DISSERTATION

Micro– and Macromechanical Models for Hybrid, Selectively Reinforced Structures

ausgeführt zum Zwecke der Erlangung des akademischen Grades

eines Doktors der technischen Wissenschaften

eingereicht an der Technischen Universität Wien,

Fakultät für Maschinenbau

von

Dipl. Ing. Christian Maximilian CHIMANI

[redacted]

Wien, im Jänner 1998 *Christian M. Chimani*

Acknowledgments

This work was carried out in the course of my employment at the Institute of Light Weight Structures and Aerospace Engineering at the Vienna University of Technology. I am deeply indebted to my thesis advisor, Prof. F.G. Rammerstorfer, for his invaluable assistance in preparing this work.
I also want to thank Prof. H.–P. Degischer for acting as co–advisor for this thesis.
Many thanks are given to Doz. H.J. Böhm for assistance and all the critical discussions with respect to my work as well as with respect to the present text.
I want to acknowledge the helpful discussions with Dr. H.E. Pettermann, especially for the introduction into his *umat*. My special thanks go to all the members of the "ILFB–gang", who have made working at the Institut für Leichtbau und Flugzeugbau an inspiring and interesting experience.
Finally I want to thank my family for their patience and support. I dedicate this thesis to my wife, Daniela.

The financial support of the BRITE EURAM Project BE'95–1183 is gratefully acknowledged.

Abstract

In modern research and development numerical simulation plays an important role for obtaining a better understanding of complex correlations in natural and technical processes and thus reducing expensive trial and error loops in experimental development procedures. Based on research in the field of micromechanics of materials in the present work numerical simulation techniques are employed and developed that make it feasible to investigate the thermo–mechanical behavior of light metal matrix composites and selectively reinforced structures.
An overview of selected micromechanical methods for the analytical and numerical description of heterogeneous materials is followed by an examination whether these methods, especially the Mori–Tanaka method, give reliable results modeling composites containing curved fibers, as found e.g. in circumferentially reinforced axisymmetric composites.

An introduction and comparison of some mechanical properties is given for fiber reinforced magnesium and aluminium based composites. This material characterization can provide information, from the mechanical point of view, for a proper selection of constituents used for the experimental development of processing routes for the manufacturing of selectively reinforced components.

At the intersection of a material interfaces and the free surface in multi material structures complex tri-axial stress states occur which are expected to be critical with respect to damage in the envisaged applications. These free edge effects are studied in terms of a bimaterial wedge problem. The stress singularities typically predicted when homogeneous material descriptions are

used are determined analytically and numerically.
Based on the analytical solution techniques rules for an optimized interface design are derived.
Introducing a micromechanical embedding technique that explicitly accounts for the micro scale heterogeneity of the composite material the previously mentioned singular solutions are reconsidered. It is found that the singular solution disappears for several important applications.

Finally a thermo–elasto–plastic analysis of a selectively, circumferentially reinforced axisymmetric structures is presented. Two modeling techniques, the incremental Mori–Tanaka approach and a hexagonal cell tiling approach, are employed for comparison. The stress distribution after cooling down from the manufacturing temperature is studied on the macro and micro level.

Zusammenfassung

Der numerischen Simulation kommt in der modernen Forschung und Entwicklung eine wichtige Rolle zu. Sie ermöglicht es, ein besseres Verständnis komplexer natürlicher und technischer Prozesse zu erlangen und hilft dadurch, teure experimentelle Entwicklungsarbeit zu verringern. Basierend auf Grundlagen aus dem Forschungsgebiet der *Mikromechanik der Werkstoffe* werden in der vorliegenden Arbeit numerische Simulationstechniken verwendet und entwickelt, die es erlauben, das thermomechanische Verhalten von Leichtmetall–Verbundwerkstoffen und selektiv verstärkten Strukturen zu untersuchen.
Nach einem Überblick über einige analytische und numerische Verfahren zur Beschreibung von heterogenen Werkstoffen wird untersucht, ob sich diese Verfahren, besonders die Mori–Tanaka Methode, zur Beschreibung von Verbunden mit nicht geradlinigen Fasern, z.B. in Umfangsrichtung verstärkten axialsymmetrische Strukturen, eignen.

Zur Unterstützung einer Werkstoffauswahl nach mechanischen Kriterien werden die wichtigsten mechanischen Eigenschaften von faserverstärkten Magnesium– und Aluminiumverbundwerkstoffen charakterisiert.
Durch die eingeschränkte Anwendung von Verstärkungsmaterial auf hoch belastete Bereiche einer Struktur kommt es zur Ausbildung von makroskopischen Materialgrenzflächen. An der freien Oberfläche führen solche Grenzflächen zu komplexen dreiachsigen Spannungszuständen, die das Versagensverhalten solcher Strukturen kritisch beeinflussen. Diese i.a. singulären Spannungen werden analytisch und numerisch untersucht. Auf der Basis von analytischen Lösungsmethoden werden Möglichkeiten für ein verbessertes Grenzflächendesign aufgezeigt.
Durch die Entwicklung einer mikromechanischen Einbettungsmetode ist es

möglich, solche Spannungskonzentrationen auf Mikroskalenebene zu untersuchen. Dadurch kann eine explizite Berücksichtigung der Mikroheterogenität realisiert werden. Für viele Anwendungen kann damit gezeigt werden, daß es, unter Berücksichtigung der Mikrostruktur, nicht zur Ausbildung von singulären Spannungsfeldern kommt.

In einer thermo–elasto–plastischen Analyse einer selektiv verstärkten axisymmetrischen Struktur werden zwei Modellierungsverfahren, eines basierend auf einer inkrementellen Formulierung der Mori–Tanaka Methode und einem Verfahren basierend auf einer hexagonalen Subzellenteilung, verglichen. Es werden die Spannungsverteilungen während und nach der Abkühlung vom Herstellungsprozeß auf Makro– und Mikroskalenebene untersucht. Mit dieser Untersuchung konnte eine sehr gute Übereinstimmung der beiden Modellierungsverfahren nachgewiesen werden.

Contents

Chapter 1

Introduction

1.1 Selectively reinforced magnesium based components, aims and scope

The fastest growing market for magnesium cast components is for automotive applications, particularly in the US, but equivalent tendencies are observed in the Asian and European markets. The reason for this are future regulations, which require fuel economy targets to be met by automobile manufacturers. Since weight reduction is even more important in aerospace engineering, there is a common tendency in the automotive as well as in aerospace engineering to increase the fuel economy by producing vehicles of lighter mass.

Accordingly there is a strong interest to substitute steel components by light weight alloys, particularly materials based on aluminum and magnesium. The aluminum industry has been by far more successful in achieving this, owing to the good chemical and mechanical properties of aluminium and to the familiarity with its use. Nevertheless, magnesium is the lightest of the structural metals with a density of only 1.74g/cm^3, i.e. magnesium has a potential of weight reductions of about 30% with respect to equivalent aluminum components. Other potential advantages of magnesium castings compared to aluminum are the better castability, a reduction of machining costs compared to aluminum, improved casting tool life and reduced transportation costs of finished castings due to their lower weight. For the future

market in magnesium cast components an annual increase of 15% is forecast [91].

1.1.1 Magnesium die casting properties

Magnesium is rarely used for engineering applications without being alloyed with other metals, typically Al, Zn, Mn, and rare earth metals, see [23]. In die casting applications most of the present products are produced by the alloy, AZ91D (9% Al, 0.5% Zn, 0.3% Mn). This alloy shows excellent die castability and good strength properties but poor ductility. Its high purity (absence of cathodic impurities, e.g. Fe) provides corrosion properties comparable to those of Al die cast alloys. For magnesium die cast applications AZ91D is always the alloy of the first choice unless it is ruled out by specific property requirements. For an improved fracture toughness alloys with reduced Al content are used to decrease the amount of embrittling intermetallics ($Mg_{17}Al_{12}$).

The mechanical properties of Mg alloys are dominated by the hexagonal lattice structure ($c/a = 1.624$), which possesses only three possible slip systems providing dislocation movement. This is also true for Zn, but there the c/a ratio is such that Zn can mechanically twin in tension, and hence new slip systems get into play. The c/a ratio of Mg allows mechanical twinning in compression only, i.e. in tension tests of polycrystalline samples twinning is not available for activating new slip systems. Thus magnesium has a comparable small ductility. A typical tensile test stress vs. strain curve shows a rather small plastic region and fracture occurs just after reaching the ultimate strength. Magnesium alloys have the lowest yield strength in the group of light metal alloys but the strength/weight ratio is about the same as that of Al and Ti, see [3, 20].

It should be noted that all mechanical properties of magnesium exhibit a pronounced temperature dependence, even at moderate temperatures. A comprehensive data collection of mechanical properties for magnesium die cast alloys is given in [5, 23]. Special consideration to the 'high' temperature properties is given in [4].

The low melting temperature of magnesium alloys, e.g. for AZ91D the melting point is approximately 420°C, indicates that time dependent (thermally activated) deformation mechanisms, i.e. creep and relaxation, also influence their mechanical behavior at rather low temperatures, see [40, 74].

As demonstrated for many metal alloys the specific strength and stiffness as well as the creep behavior of Mg can be improved considerablely by fiber reinforcements, see e.g. [31, 99].
Typical Mg based composite systems that are currently under development are carbide– and oxide ceramic particles and fibers, see e.g. [68, 71, 86, 83, 67]. A disadvantage of oxide ceramics is the high chemical affinity of Mg to oxygen leading primarily to the formation of MgO and Spinel ($MgAlO_4$) and consequently to damaged fibers and embrittlement of the matrix alloy.
The most promising reinforcement for Mg are carbon fibers. This combination leads to maximum values for the specific strength and stiffness at relatively low cost. Additionally this combination has the ability to adjust the coefficient of thermal expansion to develop dimensional stable structures, which makes this material interesting for space applications, compare e.g. [92]. Some recent studies on carbon magnesium composites are [6, 10, 36, 58, 60, 82, 109]. A comprehensive review of recent developments and tendencies of magnesium matrix composites is given in [81]

Parts of the present work are closely related to BRITE EURAM Project BE'95–1183, "Design and Processing of Selectively Reinforced Magnesium Based Components". The project's target is to provide material technologies to substitute even aluminium components for aeronautical and automotive applications by lighter castings based on magnesium, which are selectively reinforced to fulfill the service requirements: high strength and stiffness, as well as fatigue, creep and corrosion resistance at low weight. Although the optimistic expectations of recent years for the economic impact of metal matrix composites (MMC) have not been fully realized, the technical potential still exists to increase the weight-specific properties of light metals in many respects. It can be exploited by economical usage of the expensive reinforcement and by appropriate processing techniques, which require a scientific

background. Therefore, the objectives of the project are [32]:

- To develop economical production techniques for selectively reinforced light metal hybrid components consisting of a minimum amount of MMC, taking advantage of a two-step production route, where in a first step a continuous fiber reinforced MMC-insert is designed and processed at its optimum strength, which in a second step is embedded into a high strength Mg-based casting produced by modified conventional foundry techniques. A single-step technique for manufacturing selectively reinforced Mg-parts will be investigated for comparison.

- To provide criteria for the selection and the design of such hybrid components tailored to meet the service requirements. Materials research and micromechanical modeling form the basis for that development and are supplemented by specially adapted thermo-mechanical testing.

- To offer alternative process techniques together with their pros and cons for the production of small and medium/large series components demonstrated by the fabrication and evaluation of prototype components.

The main subject of this work is related to the second item. Before expensive MMC and hybrid test specimens are manufactured and tested numerical material simulation is employed to

- provide criteria for the selection of the proper materials, with respect to the thermo-mechanical behavior of the MMCs (material characterization on the basis of available material data of the constituents),

- define test specimens for experimental investigations,

- derive design rules for the shape of anisotropic reinforcing preforms,

- derive macro– and micromechanical models, which allow the numerical modeling (based on Finite Element methods) of selectively reinforced structures, including the nonlinear thermo–elasto–plastic behavior of such structures on the macro as well as on the micro level (in each constituent).

Due to the wide range of demands on the numerical simulation several methods are employed within these studies to provide optimum information making use of the individual advantages of each simulation technique. All these methods are related to the scientific field called " Micromechanics of Materials", which is discussed in chapter 2.

Apart from material characterization (where no special shape is assumed) typical simple hybrid structures also used for experimental testing are analyzed, i.e. selectively reinforced plates and a generic housing component shown in fig. 1.1.

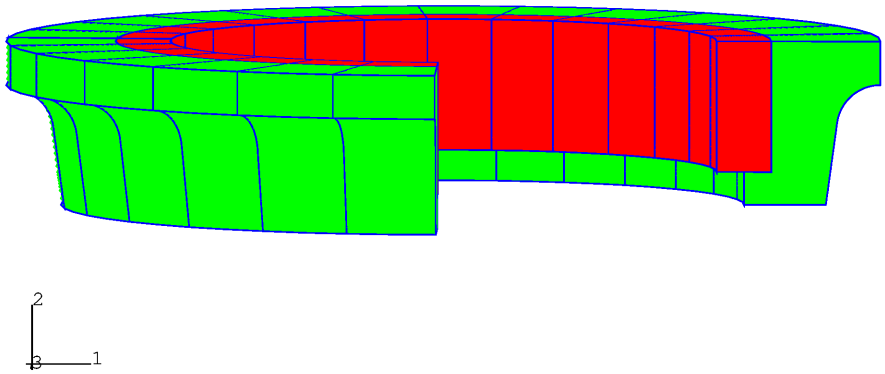

Figure 1.1: Sketch of an axisymmetric selectively reinforced generic housing component. The dark ring (insert) is a metal matrix composite surrounded by pure metal (light gray)

Within this study primarily carbon fibers are considered as reinforcing material. This is due to economic reasons, carbon fibers being the less expensive long fiber reinforcement among the possible ones, and due to their beneficial mechanical properties, see section 1.1.2. Even though different fiber types as well as different matrix alloys have also been used during the development of manufacturing techniques, the numerical studies presented in this work are restricted to the carbon fiber type T300 and to the matrix alloy AZ91D, in addition to an Altex–Al99.9 MMC for comparison. The Young's modulus E, the Poison's ratio ν and the coefficient of thermal expansion α of each constituent are given for the matrix alloys (m) AZ91D in tab. 1.1 [5], for Al99.9 in tab. 1.2 [18] and for the fiber types (i) Altex in tab. 1.3 [97] and

Table 1.1: Material data for Mg–AZ91D

T [°C]	$E^{(m)}$ [GPa]	$\nu^{(m)}$ [ ]	$\alpha^{(m)}$ [10^{-6}K^{-1}]	$\sigma_y^{(m)}$ [MPa]	$E_h^{(m)}$ [GPa]
20	45.5	0.35	25.0	160.0	1.28
50	43.9	0.35	25.2	145.0	1.28
100	40.8	0.35	25.4	140.0	1.20
150	37.4	0.35	25.7	110.0	0.90
200	27.6	0.35	26.0	73.0	0.12
250	18.7	0.35	26.4	45.0	0.11
300	18.7	0.35	26.8	10.0	0.10

for T300 carbon fibers in tab. 1.4 [104]. Additionally the yield strength σ_y and the hardening modulus E_h is given for AZ91D and Al99.9, respectively.

1.1.2 Carbon fibers and their properties

Because of their excellent performance in mechanical, electrical and thermal applications carbon fibers, particularly pitch–based carbon fibers have become one of the key materials for future development of advanced materials. Carbon fibers exhibit a wide spectrum of properties which are the consequences of micro structural variations determined by the processing route and processing parameters. There are basically three types of carbon fibers distinguished by the carbon fiber precursor: rayon, polyacrylonitrile (PAN), and petroleum pitch. Details of the production of carbon fibers are given e.g. in [64].

The mechanical properties, which are considered in the following, are determined by the graphitic submicrostructure, i.e. by atomic bonding energies, and on the microscale, by their partial crystalline–amorphous microstructure.
The basic hexagonal planar structure of graphite is sketched in fig. 1.2.
Carbon has four valence electrons, in graphite they are in the sp^2 hybrid state.

Table 1.2: Material data for Al99.9

T [°C]	$E^{(m)}$ [GPa]	$\nu^{(m)}$ [ ]	$\alpha^{(m)}$ [10^{-6}K^{-1}]	$\sigma_y^{(m)}$ [MPa]	$E_h^{(m)}$ [GPa]
20	67.2	0.35	23.0	28.2	0.638
50	66.5	0.35	23.6	27.4	0.525
100	66.3	0.35	24.5	25.9	0.367
150	63.3	0.35	25.4	23.8	0.264
200	60.0	0.35	26.3	21.1	0.199
250	54.3	0.35	27.2	17.5	0.158
300	46.8	0.35	28.1	13.6	0.125

Table 1.3: Material data for Altex fibers

T [°C]	$E^{(i)}$ [GPa]	$\nu^{(i)}$ [ ]	$\alpha^{(i)}$ [10^{-6}K^{-1}]
20	180.	0.20	6.0
300	180.	0.20	6.0

Table 1.4: Material data for carbon fibers

T [°C]	$E_A^{(i)}$ [GPa]	$E_T^{(i)}$ [GPa]	$\nu_A^{(i)}$ [ ]	$\nu_T^{(i)}$ [ ]	$G_A^{(i)}$ [GPa]	$\alpha_A^{(i)}$ [10^{-6}K^{-1}]	$\alpha_T^{(i)}$ [10^{-6}K^{-1}]
20	214.0	14.0	0.20	0.25	14.0	-0.55	5.6
300	214.0	14.0	0.20	0.25	14.0	-0.55	5.6

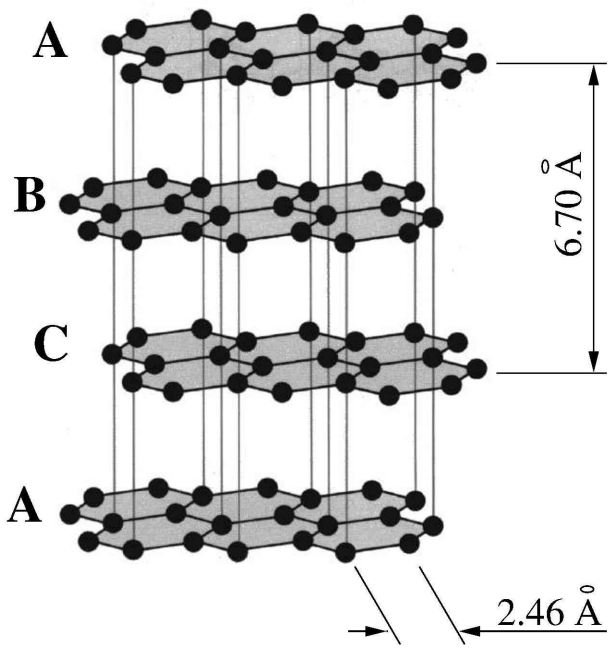

Figure 1.2: Crystal structure of graphite

Thus three electrons per atom form covalent bondings with their neighboring atoms, which causes high bonding forces in one plane (basal plane, see fig. 1.2), while the fourth electron cannot be directly related to a single atom (the neighboring electron orbitals are overlapping) and forms a bond perpendicular to the basal planes, which has much less bonding energy then the covalent bondings in the basal planes. The bonding forces are comparable to van der Waals forces. Thus the atomic spacing perpendicular to the basal planes is much higher than within the planes. The fourth valence electron is also responsible for the electric conductivity of graphite, which is excellent parallel to the basal planes but very small perpendicular to the planes. Thus the carbon microstructure leads to an extreme anisotropy of mechanical, thermal, and electrical properties.

From the microstructural point of view there are two idealized descriptions for the geometrical transverse configurations of the basal planes in circular cylindrical fibers. They are labeled as radial and onion skin configurations,

see [75]. Both types lead to a transversely isotropic mechanical behavior, i.e. their elastic behavior is described by five independent elastic constants, e.g. E_L the longitudinal Young's modulus, E_T the transversal Young's modulus, ν_A the axial Poisson ratio, G_A and G_T the axial and transversal shear moduli, see [80]. The distinction between radial and onion skin types has almost no effect on the elastic properties, only the transverse shear modulus exhibits a significant dependence, compare [26]. As stated at the beginning of the section these properties can vary over a wide range, depending on the manufacturing process. The elastic constants of the graphite hexagonal lattice (measured on a single crystal) are 1060GPa parallel to the basal planes and 36.5GPa in the perpendicular direction. Commercially available fibers reach values for the axial modulus of about 200GPa for high strength fiber to more than 500GPa for high modulus fibers. Experimentally fibers having a modulus of about 1000GPa have been developed.
Similar to the elastic properties also the thermal expansion behavior exhibits an extreme anisotropy. Perpendicular to the fiber the coefficient of thermal expansion (CTE) reaches values typical for common crystalline materials. However the axial CTE is close to zero or even negative.

One of the technical risks for the present project arises from the different thermo-mechanical material properties of the individual constituents. Especially their different thermal expansion behavior, which causes thermal eigenstresses on the micro level between reinforcement and matrix as well as on the structural level between the reinforced and the unreinforced material, must be considered. These stresses reach maximum values close to the material interfaces. The intersection points between a material interface and the free surface are known to be locations of complicated tri-axial stress states which are the consequence of the step-like, i.e. discontinuous, variation of the mechanical material parameters. Additionally at these interfaces the material strength is reduced because of the possible formation of oxide layers and intermetallics or due to imperfect metallic bonding. Thus a challenge of the present work is to find solutions which allow to overcome or handle these types of problems.

Chapter 2

Micromechanics of composite materials

2.1 Basic notions

The principal aim of theoretical studies of multiphase materials and composites is the deduction of the their overall (or effective) properties (e.g. thermo–mechanical properties such as stiffness and strength, hygrothermal properties, electro–mechanical properties, heat conduction properties, electrical and magnetic properties) from the material behavior of the components and from their microscale geometry. This corresponds to describing the behavior of the microinhomogeneous material via an equivalent continuum, a so called homogenized medium.
Descriptions of the properties of composite materials have to account for at least two (but often three or more) length scales:

- Macroscale: the length scale of the structure, component or sample
- Mesoscale: intermediate length scale (e.g. lamina level in layered composites)
- Microscale: the length scale of the reinforcement diameters or the distances of adjacent material phases (in many cases, however, the constituents may be inhomogeneous themselves, e.g. polycrystalline).

The subject of the present work is based on micromechanics of materials, i.e. the study of mechanical properties of inhomogeneous materials at the microscale as well as mechanical properties of hybrid components at the macroscale within the framework of continuum mechanics. Thus, following [17] some basic ideas on micromechanical modeling of materials are discussed in this chapter. Even though the emphasis in this work is put on the thermo–mechanical behavior of fiber reinforced composites. There is a large body of literature applying analogous or related methods to other physical properties and to a wide range of other inhomogeneous materials.

In micromechanical approaches, the stress and strain fields in an inhomogeneous material are typically split into contributions corresponding to the different length scales, which may be termed "fast" and "slow" variables. It is assumed that the length scales are sufficiently different so that variations of the stress and strain fields on the microlevel (fast variables) influence the macroscale behavior only by their average values (i.e. from the point of view of the macroscale or mesoscale the composite acts as a "material").
It is further assumed that gradients in the macroscale and mesoscale temperature, stress, and strain fields as well as compositional gradients (in terms of slow variables) are not significant at the microscale, where these fields appear to be locally constant and act as "applied" homogeneous far field temperatures, stresses, and strains.

From the point of view of a given length scale the material behavior at any lower scale may be described by that of an equivalent homogenized continuum. These assumptions are somewhat restrictive, but disregarding them could lead to erroneous results, and thus to some misinterpretation on the composite behavior. If the conditions are not met to a sufficient degree, special investigation techniques must be used, e.g. special homogenization procedures, see [22, 33]. In chapter 5 this topic is discussed for the case of a meso–macro interface (a material interface dividing two differently reinforced subregions) typically occurring in layered composites having the same matrix material in each layer, and selectively reinforced structures. An embedding modeling technique is employed, which was primarily introduced in [24] to

investigate free edge effects in hybrid materials.

For samples (or subregions of samples) that do not exhibit macroscopic stress, strain and compositional gradients, the microscale strain responses $\boldsymbol{\varepsilon}(\vec{r})$, the microscale stress response $\boldsymbol{\sigma}(\vec{r})$ and the corresponding macroscale responses, e.g. an effective mechanical strain responds $\boldsymbol{\varepsilon}_{mech}$, or an applied stress $\boldsymbol{\sigma}_a$ can be formally linked by localization relations of the type

$$\begin{aligned} \boldsymbol{\varepsilon}(\vec{r}) &= \mathbf{A}(\vec{r})\boldsymbol{\varepsilon}_{mech} \\ \boldsymbol{\sigma}(\vec{r}) &= \mathbf{B}(\vec{r})\boldsymbol{\sigma}_a \end{aligned} \tag{2.1}$$

and by homogenization relations of the type

$$\begin{aligned} \boldsymbol{\varepsilon}_{mech} &= \frac{1}{\Omega_S}\int_{\Omega_S} \boldsymbol{\varepsilon}(\vec{r})d\Omega \\ \boldsymbol{\sigma}_a &= \frac{1}{\Omega_S}\int_{\Omega_S} \boldsymbol{\sigma}(\vec{r})d\Omega \end{aligned} \tag{2.2}$$

where Ω_S stands for the volume of the sample (or of the subregion). $\mathbf{A}(\vec{r})$ and $\mathbf{B}(\vec{r})$ are called strain and stress concentration tensors (or influence functions [52]), respectively. It may be noted here that in the absence of microscopic body forces the microstresses $\boldsymbol{\sigma}(\vec{r})$ are self-equilibrated.
In the above form, eqn.(2.1) applies to elastic composites only, but it can be easily modified to cover thermo–elastic composites, see eqn.(2.3). An extension to nonlinear (i.e. thermo–elasto–plastic) composites is is discussed in section 2.2.2.
The microgeometry of real composites is at least to a certain extent random and correspondingly highly complex. Accordingly, exact expressions for $\mathbf{A}(\vec{r})$, $\mathbf{B}(\vec{r})$, $\boldsymbol{\varepsilon}(\vec{r})$, and $\boldsymbol{\sigma}(\vec{r})$ cannot realistically be provided and approximations have to be introduced.
Typically, these approximations are based on the "ergodic hypothesis", i.e. it is assumed that the heterogeneous material is statistically homogeneous. Sufficiently large subvolumes selected randomly within the sample give rise to the same effective material properties, which correspond to the sample's

overall material properties. The homogenization volume is accordingly chosen to be some reference volume element (RVE), Ω_{RVE}, which is a subvolume of Ω_S that is representative of the microgeometry of the composite. Ω_{RVE} should be sufficiently large to allow a meaningful sampling of the microfields and sufficiently small for the influence of macroscale gradients to be negligible and for an analysis of the microfields to be possible. For more thorough discussion on the size of the reference volumes see [33, 46].

2.1.1 Basic strategies in micromechanics

Homogenization methods aim to find a reference volume's response to prescribed loads (typically far-field stresses, far-field strains, or temperature changes) and deduce from it the corresponding overall properties. In micromechanics, they typically are used either for characterizing the material properties of composite materials (e.g. to generate simulated uniaxial stress vs. strain curves) or for generating macroscopic constitutive models. The latter allow the effective properties of the inhomogeneous material to be obtained for any given material state and loading history, e.g. for use as material models in Finite Element calculations (compare chapter 2.2.2).
Localization procedures are used for finding the local response of the phases when the macroscopic response of the sample or structure is known. Typical applications are evaluating the matrix stresses in an MMC in order to check for yielding, or to evaluate damage effects controlled by microscale stresses or strains such as debonding between the composite's components.
Because for realistic phase distributions the analysis of the spatial variation of the microfields in realistic reference volumes can hardly be captured computationally, many descriptions of composites are based on one of the following approximations:

- Mean Field Approaches (MFA),
- Periodic Microfield Approaches (PMA),
- Embedding Methods.

An additional difficulty that must be mentioned is of special importance for all modeling schemes, especially for metal matrix composites. For these ma-

terials, the selection of material properties for the matrix can be very difficult, because the in-situ properties of the metal matrix in the MMC can differ considerably from those of bulk samples of the same metal (as typically used for obtaining material parameters). There are various mechanisms causing such differences, e.g. refined grain size in the matrix, dominant grain orientation caused by the temperature gradient between matrix and reinforcement during manufacturing, increased and spatially varying dislocation density due to plastic deformations after cooling down from manufacturing temperature, or formation of additional phases after a chemical reaction between matrix and reinforcement, compare e.g. [11, 106]. The presence of such effects requires special care in generating models and in interpreting the results.

2.2 Mean field approaches (MFA)

In mean field approaches the microfields within each phase are approximated by their phase averages $\boldsymbol{\varepsilon}_{tot}^{(p)}$ and $\boldsymbol{\sigma}_{tot}^{(p)}$, i.e. the mean total strain and stress fields in each phase under thermomechanical loading. Such descriptions use information on the microscale topology, the inclusion shape and orientation, and (to some extent) on the statistics of the microgeometry. The localization relations then take the form

$$\begin{aligned} \boldsymbol{\varepsilon}_{tot}^{(p)} &= \bar{\mathbf{A}}^{(p)}\boldsymbol{\varepsilon} + \bar{\mathbf{a}}^{(p)}\Delta T \\ \boldsymbol{\sigma}_{tot}^{(p)} &= \bar{\mathbf{B}}^{(p)}\boldsymbol{\sigma} + \bar{\mathbf{b}}^{(p)}\Delta T \end{aligned} \tag{2.3}$$

and the homogenization relations become

$$\begin{aligned} \boldsymbol{\varepsilon}_{tot}^{(p)} &= \frac{1}{\Omega_{(p)}}\int_{\Omega_{(p)}} \boldsymbol{\varepsilon}(\vec{r})d\Omega \\ \boldsymbol{\varepsilon} &= \sum_p \xi^{(p)}\boldsymbol{\varepsilon}_{tot}^{(p)} \end{aligned} \tag{2.4}$$

$$\begin{aligned} \boldsymbol{\sigma}_{tot}^{(p)} &= \frac{1}{\Omega_{(p)}}\int_{\Omega_{(p)}} \boldsymbol{\sigma}(\vec{r})d\Omega \\ \boldsymbol{\sigma} &= \sum_p \xi^{(p)}\boldsymbol{\sigma}_{tot}^{(p)} \end{aligned} \tag{2.5}$$

where (p) stands for a given phase of the composite, $\Omega^{(p)}$ is the corresponding phase volume, and $\xi^{(p)}{=}\Omega^{(p)}/\sum_k \Omega^{(k)}$ is the volume fraction of the phase.

Note that for MFAs the phase concentration tensors $\bar{\mathbf{A}}^{(p)}$, $\bar{\mathbf{a}}^{(p)}$, $\bar{\mathbf{B}}^{(p)}$, and $\bar{\mathbf{b}}^{(p)}$ are not functions of the spatial coordinates within the reference volume (in contrast to $\mathbf{A}(\vec{r})$ and $\mathbf{B}(\vec{r})$ in eqn.(2.1)). Mean Field Approaches tend to be formulated in terms of the phase concentration tensors and they have been highly successful in describing the linear response of aligned composites.

Approaches of this type are essential for material characterization and for the structural modeling in the present work. Consequently a general overview is given. Surveys on meanfield approaches are given, e.g. in [31, 99]. For a more comprehensive treatment see [17].

Rules of Mixture

In the most general case, "rule of mixture" expressions for some (scalar) effective physical property Ψ of a two-phase composite take the form

$$\Psi = \left[\xi(\Psi^{(f)})^{\beta} + (1-\xi)(\Psi^{(m)})^{\beta}\right]^{1/\beta}, \tag{2.6}$$

where the exponent β is typically chosen to obtain a good fit to experimental data. The most popular expressions, which, in contrast to most other choices of β, have a clear physical interpretation, are β=1 (Voigt model) and β=−1 (Reuss model). Voigt expressions correspond to full strain coupling of the phases ("springs in parallel") and Reuss expressions to full stress coupling ("springs in series"), i.e. they describe the in-plane and out-of-plane behavior, respectively, of a layered material made up of two materials having the same Poisson number. The usefulness of Voigt and Reuss expressions for actual composites depends strongly on the given microtopology. Even though it neglects Poisson effects, the Voigt expression

$$E_l = \xi E_l^{(f)} + (1-\xi)E^{(m)} \tag{2.7}$$

is usually a very good approximation for the axial stiffness of continuously reinforced unidirectional composites.

Reuss-type models for the overall behavior of particle reinforced materials or for the transverse and shear properties of continuously reinforced composites,

however, typically result in excessively soft overall responses.
Even though they are not meanfield methods in the strict sense, Rules of mixture can in principle be used to generate effective "elastic tensors" (and consequently concentration tensors) that may be employed in a mean field framework. Because they do not intrinsically account for the relationships between the engineering moduli, however, such procedures are inconsistent (i.e. computing all elements of the overall elasticity tensor of a statistically transversely isotropic composite by Voigt and Reuss formulae will in general not result in a complete description of the elasticity tensor).

The VFD model

An approach which is closely related to the rules of mixture, but which gives consistent and unique overall material tensors for unidirectional continuously reinforced composites is known as the Vanishing Fiber Diameter (VFD) model originally developed by Dvorak/Bahei-el-Din [35]. The physical interpretation of the VFD model is a composite containing aligned and continuous but infinitely thin fibers (which strongly influence the axial effective behavior, but affect the transverse behavior of the composite only via the Poisson effect) in a matrix.
Due to its simplicity it has been a popular description for continuously reinforced elasto-plastic and visco-elasto-plastic UD composites since its introduction (the original VFD model was conceived as a description for MMCs), giving good results for fiber dominated properties and reasonable predictions for the hardening behavior in matrix dominated deformation modes. Since the VFD model derives the overall material tensors in a consistent manner, it has been successfully used as a material model for FE programs, e.g. [100].

Hashin's CCA and CSA models

Hashin's composite sphere assemblage [45] and composite cylinder assemblage [47] approaches (also called "direct methods") are of major interest because they give exact expressions for some engineering moduli of special, but fairly realistic, particle reinforced and aligned continuously reinforced

composites, respectively. It may be noted that even though the derivations of the CCA and CSA methods do not involve phase averaged microstresses and strains, the results can be directly interpreted in terms of mean fields.
Both CSA and CCA are based on analyzing reference volumes tightly packed with either composite spheres or composite cylinders of varying diameters (the cores of the composite spheres/cylinders consist of the reinforcement, and the matrix is placed in a concentric shell of the appropriate thickness to give the desired volume fraction). These reference volume elements are subjected to suitable homogeneous boundary conditions, from which the appropriate boundary conditions for a single cylinder or sphere are deduced. The appropriate differential equations governing elastic deformation of the composite spheres or cylinders are then solved and the overall moduli are obtained. It is not possible to derive the overall material tensors in a complete manner, so that G (for particle reinforced composites) or E_q, G_{qt} and ν_{qt} (for continuously reinforced UD composites) must be evaluated by other means, e.g. the Hashin–Shtrikman bounds [48] or three-phase self-consistent schemes [27].

2.2.1 Mean Field Methods based on Eshelby's solution

A large number of mean field descriptions for the micromechanics of composites are based on the work of Eshelby [37], who investigated the stress and strain distributions in homogeneous media containing a subregion that spontaneously changes its shape and/or size (undergoes a "transformation") so that it no longer fits into its previous space in the "parent medium".
Eshelby's results show that if an elastic homogeneous ellipsoidal inclusion (i.e. an inclusion consisting of the same material as the matrix) in an infinite matrix is subjected to a homogeneous strain $\boldsymbol{\varepsilon}_t$ (called the "stress-free strain", "unconstrained strain", "eigenstrain", or "transformation strain"), the stress and strain states in the constrained inclusion are uniform, i.e. $\boldsymbol{\sigma}^{(i)} = \boldsymbol{\sigma}^{(i)}_{tot}$ and $\boldsymbol{\varepsilon}^{(i)} = \boldsymbol{\varepsilon}^{(i)}_{tot}$. The uniform strain in the constrained inclusion (the "constrained strain"), $\boldsymbol{\varepsilon}_c$, is related to the stress-free strain $\boldsymbol{\varepsilon}_t$ by the expression

$$\boldsymbol{\varepsilon}_c = \mathbf{S}\boldsymbol{\varepsilon}_t \quad , \tag{2.8}$$

where $\mathbf{S}$ is called the Eshelby tensor. For eqn. (2.8) to hold, $\boldsymbol{\varepsilon}_t$ may be any kind of eigenstrain which is uniform over the inclusion (e.g. a thermal strain, or a strain due to some phase transformation which involves no changes in the elastic constants of the inclusion).
For spheroidal inclusions (i.e. ellipsoids of rotation) in an isotropic matrix, $\mathbf{S}$ can be evaluated analytically and depends only on the Poisson's ratio of the homogeneous material and on the aspect ratio a of the inclusion.

Mean field methods for dilute inhomogeneous matrix–inclusion composites typically aim at making use of Eshelby's expressions for the stress and strain fields in a homogeneous inclusion subjected to an eigenstrain by using the concept of an equivalent homogeneous inclusion. This strategy involves replacing the actual inhomogeneous inclusion (which has different material properties than the matrix) subjected to a given unconstrained eigenstrain with a (fictitious) "equivalent" homogeneous inclusion on which a (fictitious) "equivalent" eigenstrain is made to act.
In the case of an isotropic matrix containing inhomogeneous inclusions $\boldsymbol{\varepsilon}_t$ depends on the Poisson's ratio of the matrix and the aspect ratio of the inclusion only. Introducing an equivalent homogeneous inclusion equation (2.8) is replaced by

$$\boldsymbol{\varepsilon}_c = \mathbf{S}\boldsymbol{\varepsilon}_\tau \quad . \tag{2.9}$$

$\boldsymbol{\varepsilon}_\tau$, the equivalent eigenstrain, is chosen in such a way that the same mean stress and strain fields are obtained in the actual inhomogeneous inclusion and in the fictitious homogeneous inclusion, compare fig. 2.1. For a comprehensive discussion of the Eshelby solution see [15, 99, 31].

If a uniform external stress $\boldsymbol{\sigma}_a$ is applied to an inhomogeneous elastic matrix–inclusion system, the total stress in the inclusion, $\boldsymbol{\sigma}_{tot}^{(i)}$, will be a superposition of this applied stress and of some additional stress $\boldsymbol{\sigma}^{(i)}$ caused by the constraining effect of the surrounding matrix on the inclusions.

$$\boldsymbol{\sigma}_{tot}^{(i)} = \boldsymbol{\sigma}_a + \boldsymbol{\sigma}^{(i)} = \mathbf{E}^{(m)}(\boldsymbol{\varepsilon}_{mech}^{(m)} + \boldsymbol{\varepsilon}_c - \boldsymbol{\varepsilon}_\tau) \quad , \tag{2.10}$$

i.e. such problems can be treated by an extension of the above strategy, which takes the form of introducing an equivalent homogeneous inclusion subjected

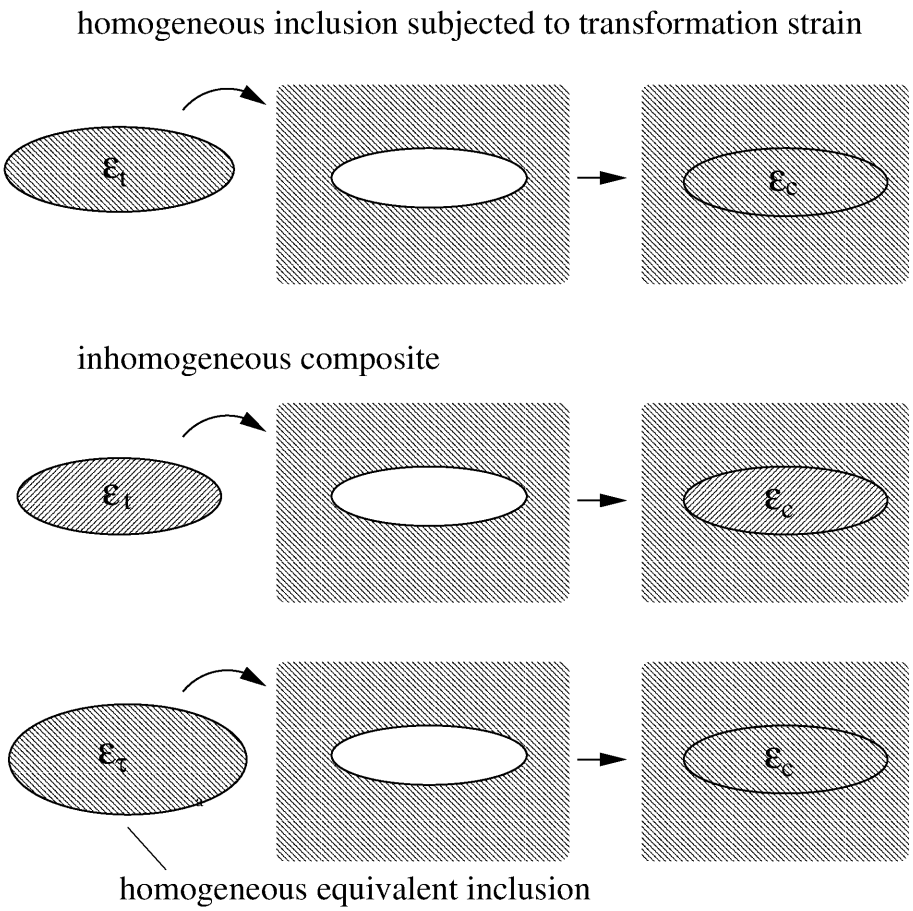

Figure 2.1: Sketch depicting Eshelby's solution procedures for a homogeneous inclusion and a typical equivalent inclusion procedure for a matrix–inclusion system loaded by a transformation strain $\boldsymbol{\varepsilon}_t$

to both the external stress $\boldsymbol{\sigma}_a$ and a suitable equivalent eigenstrain $\boldsymbol{\varepsilon}_\tau$. Again, this equivalent eigenstrain is chosen in such a way that the total average inclusion stress $\boldsymbol{\sigma}_{tot}^{(i)}$ and the constrained strain $\boldsymbol{\varepsilon}_c$ are the same in the actual (inhomogeneous) and the equivalent (homogeneous) inclusion, compare [31]. By inserting Eshelby's relation in the form of eqn.(2.9) into eqn.(2.10) and solving for the equivalent eigenstrain $\boldsymbol{\varepsilon}_\tau$ one obtains

$$\boldsymbol{\varepsilon}_\tau = [(\mathbf{E}^{(i)} - \mathbf{E}^{(m)})\mathbf{S} + \mathbf{E}^{(m)}]^{-1}[(\mathbf{E}^{(m)} - \mathbf{E}^{(i)})\boldsymbol{\varepsilon}_{mech}^{(m)} + \mathbf{E}^{(i)}\boldsymbol{\varepsilon}_t] \quad , \tag{2.11}$$

which, as expected, contains a contribution due to the applied strain $\boldsymbol{\varepsilon}_{mech}^{(m)}$

as well as a term due to the unconstrained eigenstrain $\boldsymbol{\varepsilon}_t$. Substituting eqn.(2.11) into the right hand side of eqn.(2.10) gives the following expression for the total stress in the inclusion

$$\begin{aligned}\boldsymbol{\sigma}_{tot}^{(i)} &= \mathbf{E}^{(m)}\{\mathbf{I}+(\mathbf{S}-\mathbf{I})[(\mathbf{E}^{(i)}-\mathbf{E}^{(m)})\mathbf{S}+\mathbf{E}^{(m)}]^{-1}(\mathbf{E}^{(m)}-\mathbf{E}^{(i)})\}\boldsymbol{\varepsilon}_{mech}^{(m)} \\ &\quad + \mathbf{E}^{(m)}(\mathbf{S}-\mathbf{I})[(\mathbf{E}^{(i)}-\mathbf{E}^{(m)})\mathbf{S}+\mathbf{E}^{(m)}]^{-1}\mathbf{E}^{(i)}\boldsymbol{\varepsilon}_t \quad . \end{aligned} \tag{2.12}$$

Using the relationship, which holds for a dilute composite ($\xi \to 0$), $\boldsymbol{\varepsilon}_{mech}^{(m)} = \mathbf{C}^{(m)}\boldsymbol{\sigma}_a$, eqn.(2.12) can be rewritten as

$$\begin{aligned}\boldsymbol{\sigma}_{tot}^{(i)} &= \mathbf{E}^{(m)}\{\mathbf{I}+(\mathbf{S}-\mathbf{I})[(\mathbf{E}^{(i)}-\mathbf{E}^{(m)})\mathbf{S}+\mathbf{E}^{(m)}]^{-1}(\mathbf{E}^{(m)}-\mathbf{E}^{(i)})\}\mathbf{C}^{(m)}\boldsymbol{\sigma}_a \\ &\quad + \mathbf{E}^{(m)}(\mathbf{S}-\mathbf{I})[(\mathbf{E}^{(i)}-\mathbf{E}^{(m)})\mathbf{S}+\mathbf{E}^{(m)}]^{-1}\mathbf{E}^{(i)}\boldsymbol{\varepsilon}_t \\ &= \mathbf{E}^{(m)}[\mathbf{I}+\mathbf{R}_{dil}(\mathbf{E}^{(m)}-\mathbf{E}^{(i)})]\mathbf{C}^{(m)}\boldsymbol{\sigma}_a + \mathbf{E}^{(m)}\mathbf{R}_{dil}\mathbf{E}^{(i)}\boldsymbol{\varepsilon}_t \end{aligned} \tag{2.13}$$

where the tensor $\mathbf{R}_{dil}$ is defined as

$$\mathbf{R}_{dil} = (\mathbf{S}-\mathbf{I})[(\mathbf{E}^{(i)}-\mathbf{E}^{(m)})\mathbf{S}+\mathbf{E}^{(m)}]^{-1} \quad . \tag{2.14}$$

By comparing the definition of the inclusion stress concentration tensor $\bar{\mathbf{B}}^{(i)}$, eqns.(2.3) with eqn.(2.14) and by setting the transformation strain $\boldsymbol{\varepsilon}_t$=$\mathbf{0}$ (only applied mechanical loads but no stress-free eigenstrains are considered), the following expression for the stress concentration tensor of a dilute composite is directly obtained, compare [103]

$$\bar{\mathbf{B}}_{dil}^{(i)} = \mathbf{E}^{(m)}[\mathbf{I}+\mathbf{R}_{dil}(\mathbf{E}^{(m)}-\mathbf{E}^{(i)})]\mathbf{C}^{(m)} \quad . \tag{2.15}$$

and following [9] the dilute strain concentration tensor follows as

$$\bar{\mathbf{A}}_{dil}^{(i)} = [\mathbf{I}+\mathbf{S}\mathbf{C}^{(m)}(\mathbf{E}^{(i)}-\mathbf{E}^{(m)})]^{-1} \quad . \tag{2.16}$$

It should be noted that these expressions only hold for inclusion volume fractions $\xi \ll 0.1$.

Theoretical descriptions for the overall thermoelastic behavior of composites with inclusion volume fractions of more than a few percent must explicitly account for the interaction between inclusions, i.e. for the effects of the surrounding inclusions on the stress and strain fields experienced by a given fiber or particle. One way for achieving this consists of approximating the stresses acting on an inclusion, which may be viewed as the perturbation stresses caused by the presence of other inclusions ("image stresses", "background stresses", "perturbation stresses", "mean field stresses") superimposed on the applied far field stress, by an appropriate average matrix stress. The idea of combining such a concept of an average matrix stress with Eshelby-type equivalent inclusion approaches goes back to Brown and Stobbs [21] as well as Mori and Tanaka [76]. Theories of this type are generically called Mori–Tanaka methods or "Equivalent Inclusion — Average Stress" approaches.

Mori–Tanaka methods

It was shown by Benveniste [9] that in the isothermal case the central assumption involved in Mori–Tanaka approaches can be denoted as

$$\begin{aligned} \boldsymbol{\varepsilon}_{tot}^{(i)} &= \bar{\mathbf{A}}_{dil}^{(i)}\, \boldsymbol{\varepsilon}_{tot}^{(m)} \\ \boldsymbol{\sigma}_{tot}^{(i)} &= \bar{\mathbf{B}}_{dil}^{(i)}\, \boldsymbol{\sigma}_{tot}^{(m)} \quad . \end{aligned} \tag{2.17}$$

Essentially, the methodology developed for dilute inclusions is retained and the interactions with the surrounding inclusions are accounted for by suitably modifying the stresses acting on each inclusion. Equation (2.17) may be thus viewed as a modification of eqn. (2.3) in which the applied strain or stress, $\boldsymbol{\varepsilon}_a$ and $\boldsymbol{\sigma}_a$, is replaced by the total matrix strain or stress, $\boldsymbol{\varepsilon}_{tot}^{(m)}$ and $\boldsymbol{\sigma}_{tot}^{(m)}$, respectively. Of course, suitable expressions for $\boldsymbol{\varepsilon}_{tot}^{(m)}$ and/or $\boldsymbol{\sigma}_{tot}^{(m)}$ must be introduced into the schemes in an explicit or implicit way.
Following Benveniste, eqn. (2.17) leads to strain and stress concentration tensors for non dilute composites of the form

$$\begin{aligned} \bar{\mathbf{A}}_{MT}^{(i)} &= \bar{\mathbf{A}}_{dil}^{(i)}[(1-\xi)\mathbf{I} + \xi\bar{\mathbf{A}}_{dil}^{(i)}]^{-1} \\ \bar{\mathbf{B}}_{MT}^{(i)} &= \bar{\mathbf{B}}_{dil}^{(i)}[(1-\xi)\mathbf{I} + \xi\bar{\mathbf{B}}_{dil}^{(i)}]^{-1} \quad , \end{aligned} \tag{2.18}$$

and the corresponding expressions for the matrix strain and stress concentration tensors are given by

$$\begin{aligned}
\bar{\mathbf{A}}_{MT}^{(m)} &= [(1-\xi)\mathbf{I} + \xi\bar{\mathbf{A}}_{dil}^{(i)}]^{-1} \\
\bar{\mathbf{B}}_{MT}^{(m)} &= [(1-\xi)\mathbf{I} + \xi\bar{\mathbf{B}}_{dil}^{(i)}]^{-1} \quad . \qquad (2.19)
\end{aligned}$$

Introducing the Eshelby type solution for dilute composites the Mori–Tanaka strain and stress concentration tensors take the form

$$\begin{aligned}
\bar{\mathbf{A}}_{MT}^{(m)} &= \{(1-\xi)\mathbf{I} + \xi[\mathbf{I} + \mathbf{S}\mathbf{C}^{(m)}(\mathbf{E}^{(i)} - \mathbf{E}^{(m)})]^{-1}\}^{-1} \\
\bar{\mathbf{B}}_{MT}^{(m)} &= \{(1-\xi)\mathbf{I} + \xi\mathbf{E}^{(i)}[\mathbf{I} + \mathbf{S}\mathbf{C}^{(m)}(\mathbf{E}^{(i)} - \mathbf{E}^{(m)})]^{-1}\mathbf{C}^{(m)}\}^{-1} \quad , \qquad (2.20)
\end{aligned}$$

and the expressions for the effective elasticity tensor $\mathbf{E}_{MT}$, the effective compliance tensors $\mathbf{C}_{MT}$, and the effective thermal expansion tensor $\boldsymbol{\alpha}_{MT}$ of the composite can be recovered as

$$\begin{aligned}
\mathbf{E}_{MT} &= \mathbf{E}^{(m)} + \xi[\mathbf{E}^{(i)} - \mathbf{E}^{(m)}]\bar{\mathbf{A}}_{dil}^{(i)}[(1-\xi)\mathbf{I} + \xi\bar{\mathbf{A}}_{dil}^{(i)}]^{-1} \\
\mathbf{C}_{MT} &= \mathbf{C}^{(m)} + \xi[\mathbf{C}^{(i)} - \mathbf{C}^{(m)}]\bar{\mathbf{B}}_{dil}^{(i)}[(1-\xi)\mathbf{I} + \xi\bar{\mathbf{B}}_{dil}^{(i)}]^{-1} \\
\boldsymbol{\alpha}_{MT} &= \boldsymbol{\alpha}^{(m)} + \xi[\mathbf{C}^{(i)} - \mathbf{C}^{(m)}]\bar{\mathbf{B}}_{dil}^{(i)}[(1-\xi)\mathbf{I} + \xi\bar{\mathbf{B}}_{dil}^{(i)}]^{-1} \cdot \\
&\quad [\mathbf{C}^{(i)} - \mathbf{C}^{(m)}]^{-1}[\boldsymbol{\alpha}^{(i)} - \boldsymbol{\alpha}^{(m)}] \quad . \qquad (2.21)
\end{aligned}$$

It should be noted that "standard" Mori-Tanaka theories can describe the overall thermoelastic response of composites containing aligned inclusions of a single type, which may have any aspect ratio between 0 and ∞ (i.e. aligned platelets, spherical particles, aligned short and continuous fibers). Special procedures are necessary for dealing with non-aligned or hybrid composites and materials with more than two phases, compare e.g. [85]. For further discussions of Mori–Tanaka theories for elastic inhomogeneous two-phase methods, especially of their relation to other mean field approaches and of their range of validity, see e.g. [30, 29].

Finally, it is worth noting that Mori–Tanaka type theories can be implemented into computer programs in a straightforward way. Because they are explicit algorithms, all that is required are matrix additions, multiplications

and inversions plus expressions for the Eshelby tensor. Together with their fairly good accuracy this makes them a very useful tool for assessing the stiffness and thermal expansion properties and for evaluating the thermoelastic tensors of inhomogeneous materials that show a matrix–inclusion topology with aligned inclusions or voids. Mori–Tanaka methods for thermo-elasto-plastic materials are discussed in section 2.2.2.

Self-Consistent schemes

An alternative way of extending the expressions for the elastic properties of dilute composites is based on the assumption that an inclusion is surrounded by an "effective medium" instead of the matrix (i.e. $\mathbf{E}^{(m)} \to \mathbf{E}$ and $\mathbf{C}^{(m)} \to \mathbf{C}$). The elasticity tensor of such an effective medium is given by

$$\mathbf{E} = \mathbf{E}^{(m)} + \xi(\mathbf{E}^{(i)} - \mathbf{E}^{(m)})[\mathbf{I} + \mathbf{S}\mathbf{C}(\mathbf{E}^{(i)} - \mathbf{E})]^{-1} \quad , \tag{2.22}$$

where, of course, the compliance tensor $\mathbf{C}$ is the inverse of $\mathbf{E}$. This can be interpreted as an implicit system of equations for the unknown elastic tensors $\mathbf{E}$ and $\mathbf{C}$ of the effective medium, which can be solved by self–consistent iterative schemes of the type

$$\begin{aligned} \mathbf{E}_{n+1} &= \mathbf{E}^{(m)} + \xi[\mathbf{E}^{(i)} - \mathbf{E}^{(m)}][\mathbf{I} + \mathbf{S}_n\mathbf{C}_n(\mathbf{E}^{(i)} - \mathbf{E}_n)]^{-1} \\ \mathbf{C}_{n+1} &= \left[\mathbf{E}_{n+1}\right]^{-1} \quad . \end{aligned} \tag{2.23}$$

The Eshelby tensor $\mathbf{S}_n$ in eqn.(2.23) describes the response of an inclusion in the n-th iteration for the effective medium and must be recomputed for each iteration. This approach is known as the two-phase or classical self-consistent scheme (CSCS; [53]), and its predictions are noticeably different from those of Mori–Tanaka methods. Essentially, the microstructures described by the CSCS are characterized by interpenetrating phases around ξ=0.5, with one of the materials acting as the matrix for $\xi \to 0.0$ and the other for $\xi \to 1.0$.
A more elaborate self-consistent approach, the three-phase or generalized self-consistent scheme (GSCS; [27, 28]), describes inclusions surrounded by a matrix layer (of a thickness appropriate for obtaining the required inclusion

volume fraction) embedded in an effective medium. The predictions obtained with such a procedure are generally considered as producing the best mean field type predictions for materials with matrix–inclusion microtopology, i.e. for composites in the usual sense. However, being implicit and requiring the iterative solution of nonlinear equations, this method is computationally less efficient than Mori–Tanaka approaches.

2.2.2 Incremental Mori–Tanaka method

Mean field methods can be extended into the thermo-elasto-plastic range by formulating eqn.(2.3) in terms of strain, stress, and temperature rates, $\mathrm{d}\boldsymbol{\varepsilon}^{(p)}$, $\mathrm{d}\boldsymbol{\varepsilon}^{a}$, $\mathrm{d}\boldsymbol{\sigma}^{(p)}$, $\mathrm{d}\boldsymbol{\sigma}^{a}$, and $\mathrm{d}T$, respectively, and using instantaneous concentration tensors $\bar{\mathbf{A}}_{\mathbf{t}}^{(p)}$, $\bar{\mathbf{B}}_{\mathbf{t}}^{(p)}$, $\bar{\mathbf{a}}_{\mathbf{t}}^{(p)}$, and $\bar{\mathbf{b}}_{\mathbf{t}}^{(p)}$ to give

$$\begin{aligned} \mathrm{d}\boldsymbol{\varepsilon}^{(p)} &= \bar{\mathbf{A}}_{\mathbf{t}}^{(p)}\mathrm{d}\boldsymbol{\varepsilon}^{a} + \bar{\mathbf{a}}_{\mathbf{t}}^{(p)}\mathrm{d}T \\ \boldsymbol{d\sigma}^{(p)} &= \bar{\mathbf{B}}_{\mathbf{t}}^{(p)}\boldsymbol{d\sigma}^{a} + \bar{\mathbf{b}}_{\mathbf{t}}^{(p)}\mathrm{d}T \quad . \end{aligned} \tag{2.24}$$

For the case of thermoelastic inclusions in a thermo-elasto-plastic matrix the global instantaneous tensors then take the form

$$\begin{aligned} \mathbf{E}_{\mathrm{t}}^{*} &= \mathbf{E}^{(i)} + (1-\xi)(\mathbf{E}_{\mathrm{t}}^{(m)} - \mathbf{E}^{(i)})\bar{\mathbf{A}}_{\mathbf{t}}^{(m)} \\ \boldsymbol{\alpha}_{\mathrm{t}}^{*} &= \mathbf{C}^{(i)}[\mathbf{e}^{(i)} + (1-\xi)(\bar{\mathbf{A}}_{\mathbf{t}}^{(m)})^{-1}(\mathbf{e}_{\mathrm{t}}^{(m)} - \mathbf{e}^{(i)})] \quad , \end{aligned} \tag{2.25}$$

where the specific thermal stress tensor of constituent (p) is defined as $\mathbf{e}^{(p)} = -\mathbf{E}^{(p)}\boldsymbol{\alpha}^{(p)}$.

Using the formulation of [9], Mori–Tanaka expressions for the instantaneous concentration tensors can be obtained in the form

$$\begin{aligned} \bar{\mathbf{A}}_{\mathbf{t}}^{(m)} &= \{(1-\xi)\mathbf{I} + \xi[\mathbf{I} + \mathbf{S}_{\mathrm{t}}\mathbf{C}_{\mathrm{t}}^{(m)}(\mathbf{E}^{(i)} - \mathbf{E}_{\mathrm{t}}^{(m)})]^{-1}\}^{-1} \\ \bar{\mathbf{a}}_{\mathbf{t}}^{(m)} &= (\mathbf{I} - \bar{\mathbf{A}}_{\mathbf{t}}^{(m)})(\mathbf{E}^{(i)} - \mathbf{E}_{\mathrm{t}}^{(m)})^{-1}(\mathbf{e}_{\mathrm{t}}^{(m)} - \mathbf{e}^{(i)}) \\ \bar{\mathbf{B}}_{\mathbf{t}}^{(m)} &= \{(1-\xi)\mathbf{I} + \xi[\mathbf{I} + \mathbf{E}_{\mathrm{t}}^{(m)}(\mathbf{I} - \mathbf{S}_{\mathrm{t}})(\mathbf{C}^{(i)} - \mathbf{C}_{\mathrm{t}}^{(m)})]^{-1}\}^{-1} \\ \bar{\mathbf{b}}_{\mathbf{t}}^{(m)} &= (\mathbf{I} - \bar{\mathbf{B}}_{\mathbf{t}}^{(m)})(\mathbf{C}^{(i)} - \mathbf{C}_{\mathrm{t}}^{(m)})^{-1}(\boldsymbol{\alpha}^{(m)} - \boldsymbol{\alpha}^{(i)}) \quad . \end{aligned} \tag{2.26}$$

Here $\mathbf{I}$ is the identity tensor and $\mathbf{S}_{\mathrm{t}}$ stands for the instantaneous Eshelby tensor, which depends on the instantaneous material properties of the matrix

and on the aspect ratio of the inclusions. In the elasto-plastic range it has to be evaluated numerically, e.g. by the procedure proposed by Gavazzi and Lagoudas [38].
Compared to mean field approaches based on secant plasticity, incremental Mori–Tanaka (IMT) procedures have the advantage of not being restricted to radial loading at the microlevel, which is vital for their use as material models in FE programs. They show a tendency, however, towards overpredicting the overall hardening behavior of the inhomogeneous material, compare [98]. IMT-type procedures in the literature include e.g. [62, 59].
In [85] the IMT algorithm given by eqns.(2.24)–(2.26) was implemented as a user supplied material module (UMAT) for the FE code ABAQUS [1], which requires that at each integration point and in each iteration the overall stress response and the elasto-plastic tangent operator be evaluated for some prescribed strain increment. Because in the case of the IMT model the elasto-plastic material behavior is directly defined only for the matrix and not for the overall response, a combination of a radial return mapping algorithm at the level of the elasto-plastic matrix and an Euler backward iteration scheme was selected for this task. Appropriate provisions had to be made for resolving the thermal strains in the case of thermo-elasto-plastic behavior, because in inhomogeneous materials such as MMCs the thermal expansion response depends on the load history and, as is evident from eqn.(2.25), on the instantaneous moduli of the matrix. For details of the algorithm, which is also capable of handling temperature dependent material parameters, see [85].

It should also be mentioned that in addition to the previously described micromechanical approaches there are also macromechanical approaches for simulating the elasto plastic-behavior of fiber reinforced composites using anisotropic plasticity material models, which where primarily introduced by Hill [51]. Whereas Hill type plasticity models are very useful for the description of anisotropic metals, e.g. sheet metals, they are not capable of modeling the anisotropic inelastic behavior of fiber composites with an acceptable accuracy. Comparisons with the IMT approach demonstrate that the anisotropic Hill model only produces reasonable results for the first stage of yielding,

whereas the hardening stage could not be covered correctly. There are several assumptions introduced, which are very useful for pure metals, but do not hold satisfactorily for composites:

- There is no influence of hydrostatic stress states on the plastic deformation behavior.
- The Poisson ratio is assumed to be 0.5 (constant volume) for plastic deformations.
- The hardening behavior is originally assumed to be a scalar function of the stress–strain state.
- The shape of the yield surface is far too restrictive for fiber reinforced composites.
- With respect to the thermal expansion behavior it is not possible to account for the load history dependence of the thermal expansion behavior of composite materials.

Some more sophisticated macro-plasticity models have been proposed, which can at least account for some of the previously mentioned shortcomings, see e.g. [41, 56, 61, 94, 102].
The main advantage of these continuum approaches for the use in non-linear structural analysis is that they are less expensive with respect to computer power. In comparison to micromechanically based methods, however, they are less accurate, and they do not provide any information about stress and strain field of the constituents. The main problem for the application of macro-plasticity approaches to model composite materials is that the effective composite behavior has to be determined experimentally. I.e. it is not possible to determine the effective composite properties form the properties of the individual constituents.
As it will be demonstrated in chapter 4 it should be mentioned that it is not possible to model the elasto–plastic behavior of a composite material correctly, assuming the effective coefficient of thermal expansion to be a material constant.

2.3 Periodic microfield approaches (PMA)

Periodic microfield approaches aim at describing the macroscale and microscale behavior of composites by investigating model composites with periodic phase arrangements. In comparison with mean field approaches, such strategies allow a much more detailed description of the microscale variations of the stress and strain fields, and many effects of inclusion shapes and arrangements can be investigated at considerable depth. Periodic microfield approaches are, however, subject to inherent limitations in accounting for the statistical phase arrangements typically found in actual composites, and they tend to be restricted in the mechanical loading conditions that can be modeled. Due to the detailed description of the microscale stress and strain fields, periodic microfield models are well suited to studying microscale failure mechanisms and failure-related effects in composite materials, and they are highly useful for material characterization.
Periodic microfield investigations typically analyze the behavior of an infinite periodic arrangement (in two or three dimensions) of the constituents under the influence of some far-field load (this, of course, corresponds to the assumption that macroscale gradients of the stress and strain fields are not noticeable on the microscale) or some constant temperature field. In some studies, e.g. investigations of Functionally Graded Materials (e.g. [105] or analysis of thin layers of monofilament reinforced unidirectional MMCs (see e.g. [57]), however, free boundaries and microscale stress or temperature gradients were accounted for.

The stress and strain fields in infinite periodic microgeometries can be studied analytically by employing series expansions that make use of the periodicity of the phase arrangements, e.g. [93].
For the majority of periodic microfield studies of composites, however, standard numerical engineering methods have been used to compute the microfields in the unit cells, typically at high resolution. At present, the FEM is the most popular numerical scheme for unit cell investigations of inhomogeneous materials, especially in the nonlinear range. Figure 2.2 shows a typical FE unit cell for a periodic hexagonal arrangement of fibers.

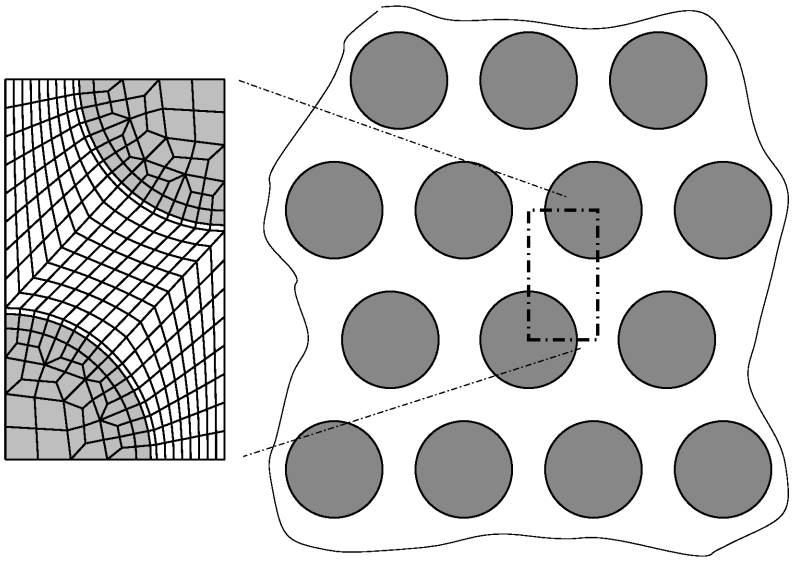

Figure 2.2: Unit cell for a periodical hexagonal fiber arrangement

The proper use of unit cell based methods requires that the unit cells together with the boundary conditions prescribed on them generate valid tilings of the problem space both for the undeformed geometry and for all deformed states pertinent to the investigation (i.e. gaps or overlaps between neighboring unit cells must be avoided). Of course, the boundary conditions for the unit cells must be selected in such a way that all deformation modes appropriate for the load cases to be investigated can be attained. Usual choices are boundary conditions of the periodic, symmetry and point symmetry types. The primary practical challenge within such a "mechanics of materials" approach involves the development of appropriate unit cells that allow a close representation of the microgeometries of actual inhomogeneous materials within available computational resources. In addition, a less obvious difficulty is encountered when the response to general loading conditions is to be modeled. Whereas periodic boundary conditions are sufficiently general for dealing with such problems, the specification of appropriate microscale loads or load distributions that do not constrain the generality of the model tends to be difficult in all but the simplest cases (e.g. setting up tractions giving rise to overall simple shear in a general orientation is challenging). Together

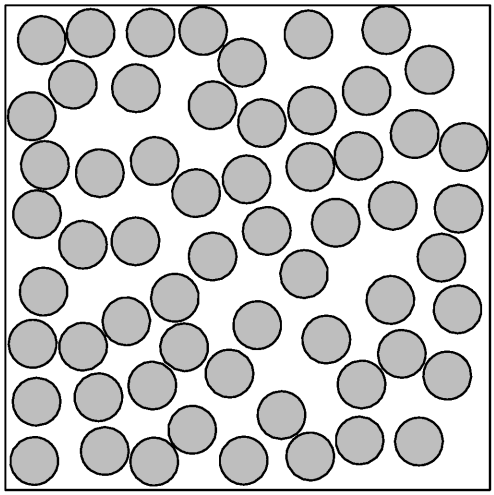

Figure 2.3: Multi fiber unit cell for a continuously fiber reinforced composite

these limitations restrict the range of applications of periodic microfield approaches. It may be noted that difficulties of this type can be resolved by using descriptions based on asymthotic homogenization, see [98].

Composites reinforced by continuous aligned fibers typically show a statistically transversely isotropic overall behavior. Their overall thermoelastic properties are very satisfactorily described by generalized self-consistent schemes and Mori–Tanaka methods, so that periodic microfield analysis are of interest mainly for their nonlinear and damage-related responses. However, in order to model realistic phase distributions such periodic cells can get quite complex. It should be noted that the VFD method [35], incremental Mori–Tanaka methods, and Aboudi's Method of Cells [2] can give reasonably good results for the overall elasto-plastic and thermo-visco-elasto-plastic behavior of unidirectional continuously reinforced composites at low computational costs, but do not resolve the microfields as well.

The thermo-mechanical behavior of composites reinforced by continuous aligned fibers under mechanical loading by axial and transverse normal stresses, hydrostatic stresses and certain transverse shear stresses as well as under thermal loading can be described by two-dimensional models employing gener-

alized plane strain conditions, three dimensional analysis being mainly of interest in the context of stress distributions near failed fibers (see e.g. [69]). It should be noted, however, that generalized plane strain conditions are not suitable for modeling the response of unidirectional composites under axial shear loading [95].
Even though periodical arrangements like the one shown in fig. 2.2 can reproduce many features of the fiber distributions in actual composites (and are thus useful for some damage related investigations), they are clearly not fully representative of "real" composites. Much improved descriptions in this respect can be obtained by multi-fiber unit cells, e.g. [79], in which the fiber positions are selected in a pseudo-random way, compare fig. 2.3.

2.4 Embedding methods

Alternatively to studying composites via periodic microgeometries, models may be used that consist of an inner "core" with a discrete phase arrangement that is embedded in an outer zone in which the microfields are resolved less accurately and which serves mainly to introduce the applied far field loads. Whereas in periodic microfield methods all features of the phase arrangement are repeated within each unit cell, embedding approaches allow to effectively "zoom in"into regions of interest, what is highly desirable for investigating e.g. the microfields near crack tips or macroscale interfaces in inhomogeneous materials. Accordingly, embedding strategies are the methods of choice for the above type of problem, where they can be used for any type of inhomogeneous material.
Because of the step like changes from homogenized material description to a discrete phase arrangement typically perturbed stress fields occur at the boundary layers of the embedded models, which decay within a region comparable to the size of the reinforcements. Thus, choosing the embedded model large enough, such perturbations are of negligible influence for the region of interest.

One type of embedding approach, see e.g. [96], uses discrete phase arrangements in both the core region and in the surrounding material, the latter

being, however, discretized much more coarsely. Such models, which may be similar to periodic microfield descriptions containing a refined mesh in some inner region, largely avoid boundary layers as discussed above, but tend to be relatively expensive in terms of computational costs.
More commonly, homogeneous (smeared out) material properties are used for the embedding region. In the simplest case, the material parameters are obtained from measurements in conjunction with a proper material law or by some micromechanical theory as discussed previously. An approaches of this type is used in chapters 5 and 6 for a detailed investigation of free edge effects in selectively reinforced structures.

The strategy of using a homogeneous embedding region has been further developed by describing the material properties of this outer zone via the homogenized material behavior of the core. Such approaches are frequently viewed as some sort of computational analogies to the three-phase self-consistent scheme, in which the response of a more complex composite core is evaluated by analytical or numerical methods [19]. Methods of this type can be used without major limitations in the elastic range, see e.g. [44]. However, difficulties typically arise in the elastic-plastic regime, where rather strong assumptions have to be introduced with respect to both the selection of the macroscale plasticity theory and the functional dependence of the overall hardening behavior to be used for the embedding region. Accordingly, such approaches have been termed "quasi self-consistent schemes".

Chapter 3

On curvature effects in modeling circumferentially reinforced composites

In general mean field methods based on the Eshelby approach, e.g. the Mori–Tanaka method, as well as unit-cell based homogenization strategies for determining micromechanically based effective material laws for unidirectionally reinforced composites assume that the axes of the reinforcements are straight on the micro level, compare chapter 2. In particular, for describing the macroscopical behavior of aligned continuous fiber composites used in circumferentially reinforced axisymmetrical structures (compare, generic part fig. 1.1) or other structures with curved reinforcements, these methods do not explicitly take into account a possible influence of the curvatures of the fibers. It might however, be expected that stiff fibers in the form of concentrically arranged rings in a soft matrix can lead to (matrix) stress states on the micro level that cannot be satisfactorily described by these methods. For example, in a uniformly heated composite cylinder with circumferentially oriented continuous fibers that have a coefficient of thermal expansion smaller than that of the matrix, the local, i.e. microscale, matrix stress state will show higher radial compressive stresses at that side of the fiber which is closer to the cylinder axis than at the opposite side of the fiber's cross section. Methods based on micromechanical models in which straight fibers

are considered are not capable of showing this local effect.

A similar problem arises if a curved thick laminate is treated by simple lamination theory. Since for this problem an analytical reference solution for a multi-layered cylinder can be derived, the curvature effect is first studied on the basis of the laminate.
In order to assess the curvature effect in UD continuous fiber reinforced composites the above multi-layer cylinder solution can also be used as a reference solution with the restriction that, in contrast to the behavior of a circumferentially UD fiber reinforced cylinder, in the multilayer cylinder solution axial strain coupling is assumed.
The individual layers are arranged in such a way that they represent fibers and matrix, respectively, in a thick-walled circular cylindrical tube reinforced by circumferential aligned fibers. The analytical solution follows and extends the derivations presented in [89].
The micro- or meso-mechanical approaches compared with the reference solution are the simple lamination theory (LAM) [54] and the Mori–Tanaka method (MTM) [76]. In the LAM and MTM approaches the local curvature effects are not included in the macroscopic material law. Additional solutions for the cylinder reinforced by circumferential aligned continuous fibers were obtained by analyses combining a hexagonal cell tiling concept (HCT) with axisymmetric FE. In this approach the fiber curvature effects are explicitly taken into account and the assumption of axial shear coupling in the multilayer model is avoided. However, the individual fibers are typically modeled with diameters larger than in reality. This phase pattern, or modeling effect is discussed in section 3.2.

3.1 Analytical solution for an axisymmetric laminate

3.1.1 General analytical solution for a thick–walled layered cylinder under thermo–mechanical loading

Assuming axisymmetric generalized plane strain conditions and cylinder coordinates, Hooke's law is given by

$$\begin{aligned}
\epsilon_{rr} &= 1/E(\sigma_{rr} - \nu(\sigma_{\varphi\varphi} + \sigma_{zz})) + \alpha\Delta T \\
\epsilon_{\varphi\varphi} &= 1/E(\sigma_{\varphi\varphi} - \nu(\sigma_{rr} + \sigma_{zz})) + \alpha\Delta T \\
\epsilon_{zz} &= 1/E(\sigma_{zz} - \nu(\sigma_{\varphi\varphi} + \sigma_{rr})) + \alpha\Delta T.
\end{aligned} \tag{3.1}$$

Using the definitions

$$\nu^* := \frac{\nu}{1-\nu}, \quad E^* := \frac{E}{1-\nu^2}, \tag{3.2}$$

where E is the Young's modulus and ν Poisson's ratio, we obtain

$$\begin{aligned}
\sigma_{\varphi\varphi} &= E^* \frac{1}{1-\nu^{*2}}\Big[\epsilon_{\varphi\varphi} + \nu^*(\epsilon_{rr} + \epsilon_{zz}) - (1+2\nu^*)\alpha\Delta T\Big] \\
\sigma_{rr} &= E^* \frac{1}{1-\nu^{*2}}\Big[\epsilon_{rr} + \nu^*(\epsilon_{\varphi\varphi} + \epsilon_{zz}) - (1+2\nu^*)\alpha\Delta T\Big] \\
\sigma_{zz} &= E^* \frac{1}{1-\nu^{*2}}\Big[\epsilon_{zz} + \nu^*(\epsilon_{\varphi\varphi} + \epsilon_{rr}) - (1+2\nu^*)\alpha\Delta T\Big].
\end{aligned} \tag{3.3}$$

The relations between strains and radial displacement u_r are given by

$$\epsilon_{rr} = \frac{\partial u_r}{\partial r}, \quad \epsilon_{\varphi\varphi} = \frac{u_r}{r}, \quad \epsilon_{zz} = C. \tag{3.4}$$

The local equilibrium condition

$$\frac{\partial \sigma_{rr}}{\partial r} + \frac{1}{r}(\sigma_{rr} - \sigma_{\varphi\varphi}) = 0 \tag{3.5}$$

leads to a differential equation for u_r

$$\frac{\partial^2 u_r}{\partial r^2} + \frac{1}{r}\frac{\partial u_r}{\partial r} - \frac{u_r}{r^2} = (1+2\nu^*)\alpha\frac{\partial \Delta T}{\partial r} \tag{3.6}$$

with the general solution

$$u_r = \frac{A}{r} + B\,r + (1+2\nu^*)\frac{\alpha}{r}\int \Delta T\, r\, dr. \tag{3.7}$$

Hence, for an axisymmetric cylinder we obtain an equation with three unknown variables A, B and C which have to be determined from the boundary conditions. Equations 3.1 and 3.3 lead to

$$\begin{aligned}\epsilon_{rr} &= -\frac{A}{r^2} + B - (1+2\nu^*)\frac{\alpha\Delta T}{r^2}(R\,t + \frac{1}{2}t^2)\\ \epsilon_{\varphi\varphi} &= \frac{A}{r^2} + B + (1+2\nu^*)\frac{\alpha\Delta T}{r^2}(R\,t + \frac{1}{2}t^2)\end{aligned} \tag{3.8}$$

$$\begin{aligned}\sigma_{rr} =& \frac{E^*}{1-\nu^{*2}}\Big[\frac{A}{r^2}(\nu^*-1) + B(1+\nu^*) + \nu^* C\\ &+ (1+2\nu^*)\alpha\Delta T(\frac{1}{r^2}(R\,t + \frac{1}{2}t^2)(\nu^*-1) - 1)\Big]\end{aligned} \tag{3.9}$$

$$\begin{aligned}\sigma_{\varphi\varphi} =& \frac{E^*}{1-\nu^{*2}}\Big[\frac{A}{r^2}(\nu^*-1) + B(1+\nu^*) + \nu^* C\\ &+ (1+2\nu^*)\alpha\Delta T(\frac{1}{r^2}(R\,t + \frac{1}{2}t^2)(1-\nu^*) - 1)\Big]\end{aligned} \tag{3.10}$$

$$\sigma_{zz} = \frac{E^*}{1-\nu^{*2}}\Big[2\nu^* B + C - (1+2\nu^*)\alpha\Delta T\Big]. \tag{3.11}$$

3.1.2 n–layered cylinder

Employing the solution for a homogeneous isotropic thick walled cylinder given in the previous section, we derive the thermo-elastic solution for an arbitrarily layered cylindrically shaped structure under thermo–mechanical loading.

Let us assume an n–layered circular cylindrical structure which is initially stress free. Each individual layer is assumed to be homogeneous and isotropic with the thickness ${}^i t$, the elasticity matrix ${}^i\mathbf{E}$, and the vector ${}^i\alpha$ for the coefficients of thermal expansion, see fig. 3.1. There are no mechanical loads on the inner and outer surfaces of the cylinder, and homogeneous thermal

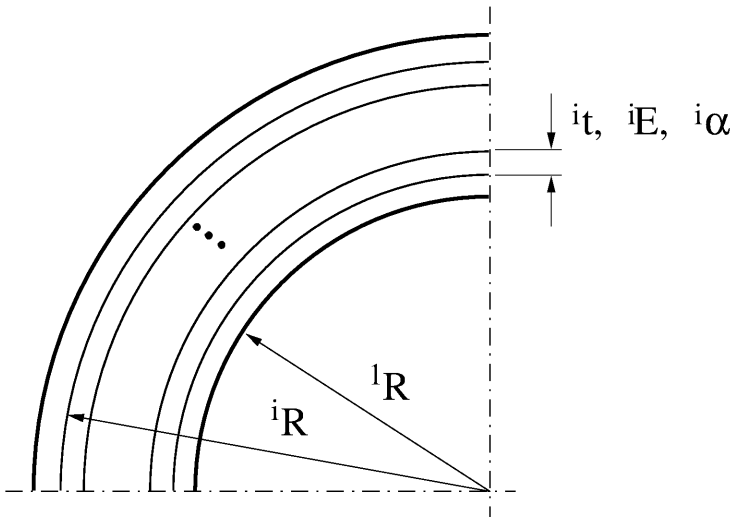

Figure 3.1: Generic model of an n–layered cylindrical structure

loading under axisymmetric generalized plane strain conditions is considered. Accordingly following boundary and continuity conditions must be met:

$$^{1}\sigma_{rr}(^{1}R) = 0, \tag{3.12}$$

$$^{n}\sigma_{rr}(^{n}R + ^{n}t) = 0. \tag{3.13}$$

Continuity of radial stresses σ_{rr} and displacements u_r at the layer boundaries leads to

$$^{i}\sigma_{rr}(^{i}R + ^{i}t) = ^{i+1}\sigma_{rr}(^{i+1}R) \qquad i = 1, n-1, \tag{3.14}$$

$$^{i}u_{r}(^{i}R + ^{i}t) = ^{i+1}u_{r}(^{i+1}R) \qquad i = 1, n-1. \tag{3.15}$$

Furthermore, because there are no external loads the following condition must hold

$$\int_{^{1}R}^{^{n}R+^{n}t} \sigma_{zz}\, r\, dr = 0. \tag{3.16}$$

Introducing eqns.(3.7) – (3.9) into the above eqns. (3.12 – 3.16) we come up with a system of $2n+1$ equations for $2n+1$ variables ${}^iA$, ${}^iB$ and C, $i=1$, $\dots$, n.

Equation (3.12) leads to

$$
\begin{aligned}
&{}^1A\,\frac{{}^1\nu^*-1}{{}^1R^2}+{}^1B(1+{}^1\nu^*)+C\,{}^1\nu^*=\\
&-(1+2\,{}^1\nu^*)\,{}^1\alpha\,\Delta T\Big[\frac{1}{{}^1R^2}({}^1R\ {}^1t+\frac{1}{2}\ {}^1t^2)({}^1\nu^*-1)-1\Big],
\end{aligned}
\tag{3.17}
$$

where ${}^i\alpha$ is the coefficient of thermal expansion in the i–th layer and ΔT is the temperature load. ${}^iA, {}^iB$ and C are constants to be determined from the boundary and continuity conditions. From eqn. (3.13) we obtain

$$
\begin{aligned}
&{}^nA\,\frac{{}^n\nu^*-1}{({}^nR+{}^nt)^2}+{}^nB(1+{}^n\nu^*)+C\,{}^n\nu^*=\\
&-(1+2\,{}^n\nu^*)\,{}^n\alpha\,\Delta T\Big[\frac{1}{({}^nR+{}^nt)^2}({}^nR\ {}^nt+\frac{1}{2}\,{}^nt^2)({}^n\nu^*-1)-1\Big]
\end{aligned}
\tag{3.18}
$$

Using the convention $j=i+1$ eqns. (3.14) give rise to the expressions

$$
\begin{aligned}
&{}^iA\,\frac{{}^iE^*}{1-{}^i\nu^{*2}}\frac{{}^i\nu^*-1}{{}^jR^2}-{}^jA\,\frac{{}^jE^*}{1-{}^j\nu^{*2}}\frac{{}^j\nu^*-1}{{}^jR^2}+{}^iB\,\frac{{}^iE^*(1+{}^i\nu^*)}{1-{}^i\nu^{*2}}-\\
&{}^jB\,\frac{{}^jE^*(1+{}^j\nu^*)}{1-{}^j\nu^{*2}}+C\Big(\frac{{}^iE^*\,{}^i\nu^*}{1-{}^i\nu^{*2}}-\frac{{}^jE^*\,{}^j\nu^*}{1-{}^j\nu^{*2}}\Big)=\\
&\frac{{}^jE^*}{1-{}^j\nu^{*2}}\,{}^j\alpha\,\Delta T(1+2\,{}^j\nu^*)\Big[({}^j\nu^*-1)({}^{i+2}R^2-{}^jR^2)\frac{1}{2\,{}^jR}-1\Big]-\\
&\frac{{}^iE^*}{1-{}^i\nu^{*2}}\,{}^i\alpha\,\Delta T(1+2\,{}^i\nu^*)\Big[({}^i\nu^*-1)({}^jR^2-{}^iR^2)\frac{1}{2\,{}^jR}-1\Big]\qquad i=1,n-1
\end{aligned}
\tag{3.19}
$$

Equation (3.15) leads to

$$
\begin{aligned}
&{}^iA\,\frac{1}{{}^jR}-{}^jA\,\frac{1}{{}^jR}+{}^iB\,{}^jR-{}^jB\,{}^jR=\\
&\frac{\Delta T}{2\,{}^jR}\Big[-(1+2\,{}^i\nu^*)\,{}^i\alpha(2\,{}^iR\,{}^it+{}^it^2)+(1+2\,{}^j\nu^*)\,{}^j\alpha(2\,{}^jR\,{}^jt+{}^jt^2)\Big]\\
&i=1,n-1
\end{aligned}
\tag{3.20}
$$

and from eqn. (3.16) one obtains

$$\sum_{i=1}^{n} {}^{i}B \frac{{}^{i}E^{*}\,{}^{i}\nu^{*}}{1-{}^{i}\nu^{*2}}({}^{j}R^{2}-{}^{i}R^{2}) + C\sum_{i=1}^{n}\frac{{}^{i}E^{*}}{1-{}^{i}\nu^{*2}}\frac{1}{2}({}^{j}R^{2}-{}^{i}R^{2}) =$$
$$\sum_{i=1}^{n} {}^{i}E^{*}\frac{1+2\,{}^{i}\nu^{*}}{2(1-{}^{i}\nu^{*2})}\,{}^{i}\alpha\,\Delta T({}^{j}R^{2}-{}^{i}R^{2}). \tag{3.21}$$

In matrix notation these $2n+1$ linear equations can be written as

$$\mathbf{K}\,\mathbf{x} = \mathbf{d} \tag{3.22}$$

where $\mathbf{K}$ is a non-symmetric sparse coefficient matrix and $\mathbf{x}$ is the vector of unknown quantities ${}^{i}A, {}^{i}B$ and C. $\mathbf{d}$ is a vector depending on the boundary conditions as well as on the material properties.
This system of equation is solved using a modified Gauss–Jordan algorithm. Thus we end up with a full description of stresses and strains within each layer as well as the global thermo-mechanical behavior of the arbitrarily layered cylinder.

3.2 Discussion of simulation results

Since it is the aim of this chapter to verify the applicability of the Mori–Tanaka method for axisymmetric inclusion–matrix composites, a multi-layered cylinder is studied in which two different layers alternate consecutively, i.e. ${}^{i+2}t = {}^{i}t$ and ${}^{i+2}\mathbf{E} = {}^{i}\mathbf{E}$. Fictitious material data which provide a considerable elastic contrast between neighboring layers were assumed: ${}^{1}E/{}^{2}E = 0.1$, ${}^{1}\nu = {}^{2}\nu = 0.3$ and the coefficients of thermal expansion fulfill ${}^{1}\alpha/{}^{2}\alpha = 10$. The layered structure is used as a model for a circumferentially continuous fiber reinforced material in a circular cylindrical body, with material 1 representing the matrix, and material 2 representing the reinforcing fibers. Correspondingly, the layer thicknesses are determined by the volume fractions of the phases and by the total number of layers. It should be mentioned that the number of layers must not be too small and, consequently, the layers must not be too thick, in order to allow neglecting the difference between the volume fractions and the fractions of meridian cross sections of the phases.

A fiber volume fraction of $\xi = 1/3$ and a total number of layers $n = 11, 27$ and 67, respectively, were chosen for the considered examples. In order to quantify the curvature effect two different cylinder geometries were treated: $R_i = 10\text{mm}$, $R_a = 11\text{mm}$, which relates to a "moderate curvature", and $R_i = 1\text{mm}$, $R_a = 11\text{mm}$ corresponding to a "strong curvature". R_i and R_a represent the inner and the outer radius, respectively, of the layered cylinder. A constant temperature load of $\Delta T = +10\text{K}$ was applied to the models.

The resulting stresses within the composite cylinder with a weak curvature are displayed in fig. 3.2 for the circumferential stress component, in fig. 3.3 for the radial component and in fig. 3.4 for the axial component, respectively. In each figure results are shown for cylinders composed of 11(bold solid line), 27(dashed line) and 67(thin solid line) individual layers. The stresses are plotted over the thickness of the cylinder in radial direction from the inner radius of the cylinder to the outer one. In fig. 3.2 we find that the circumferential stresses alternate in a stepwise manner from compression in the softer layers to tension in the stiffer ones. The magnitude of the compressive stresses is nearly constant over the whole thickness, whereas the tensile stresses within the stiffer material increase from the inner layers to the outer ones. Thus, the effective (integral) stress state changes from compression to tension with increasing radial distance while maintaining global equilibrium. Comparing the results derived for the models with different numbers of layers, we did not find any qualitative changes using a moderately small number of layers. Similar results were found for the axial stress components. It should be mentioned that due to the small curvature of the individual layers the radial stress components are small and, accordingly, their influence on the overall stress distribution is negligible, see fig. 3.3.

Next, analytical results are compared to predictions obtained from conventional lamination theory, where the composite cylinder is described using the macroscopical material law of a thin laminate, see [54]. In this material model the influence of the curvature on the material behavior is not taken into account. The results are plotted in fig. 3.5 for the case of an 11–layer cylinder.

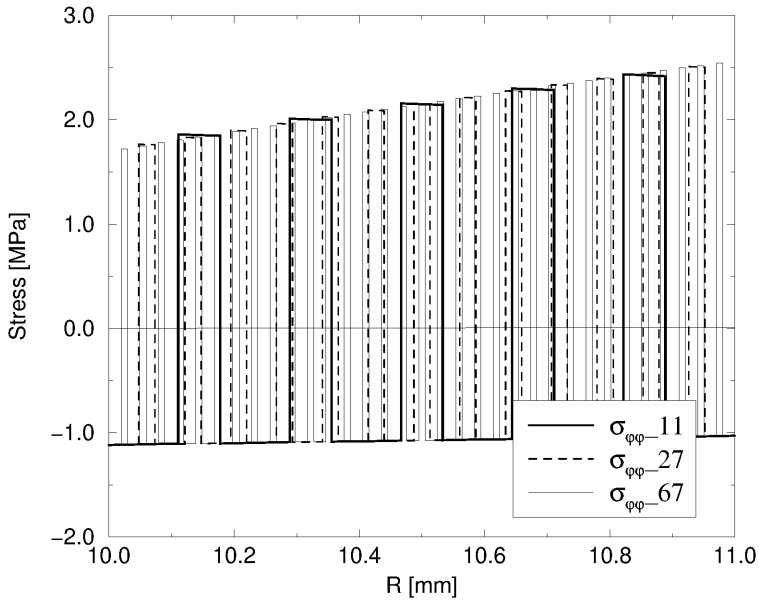

Figure 3.2: Distribution of circumferential stresses $\sigma_{\varphi\varphi}$ for cylinders composed of 11, 27 and 67 layers, respectively, as a function of their radial position

It is obvious that even for the small curvature case the resulting circumferential stresses within the stiffer layers exhibit an error of about 10%, which is due to the fact that the simple lamination shell theory cannot capture the appearance of effective, i.e. macroscopic, thermal stresses under uniform temperature loads which are caused by the anisotropy of the effective thermal expansion behavior. In contrast to a fully unconstrained body of isotropic homogeneous material, in which no thermal stresses appear under uniform temperature loads, in the case of anisotropic materials such thermal stresses must not be excluded. Effective thermal stresses of this kind are shown in fig. 3.8 denoted there by $\sigma^*_{\varphi\varphi}$_MTM.

Next we switch to the two micromechanical approaches which get employed for the description of axisymmetrical metal matrix composites reinforced by circumferentially oriented continuous fibers in chapter 6. In one approach the classical Mori–Tanaka method was used to derive the overall thermo elastic material behavior which was then employed as input for the Finite Element

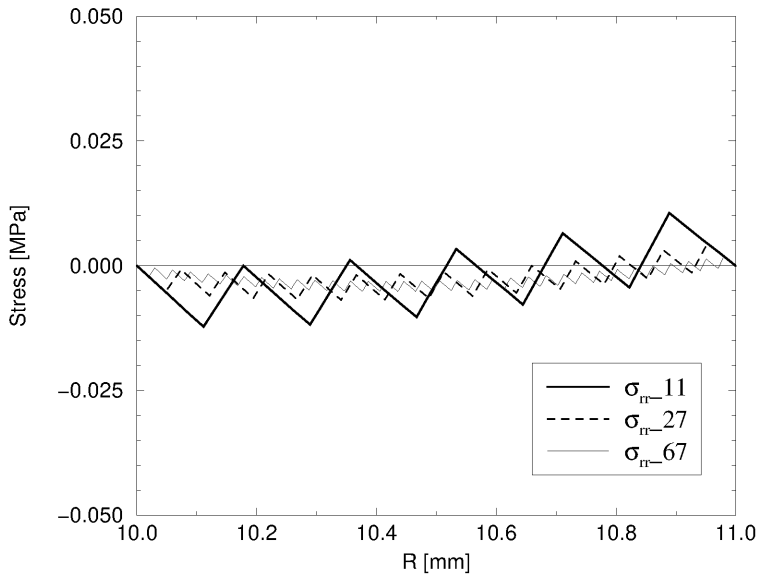

Figure 3.3: Distribution of radial stresses σ_{rr} for cylinders composed of 11, 27 and 67 layers, respectively, as a function of their radial position

code. In a complementary approach a model micro geometry was generated by a hexagonal cell tiling (HCT) concept, (i.e. the computational domain is divided into regular hexagons that are assigned to either fibers or matrix and subsequently modified to obtain the required fiber volume fraction) and discretized with 6-noded triangular elements using special preprocessing software [16]) and used as a 2D axisymmetric FE analysis. Here, due to limitations in computational power, the fibers are not modeled with their real dimensions, but with somewhat larger diameters. Two different HCT models were used, one with 63 fibers per cross-section and another one with 1036, see fig. 3.6. Symmetry boundary conditions were applied at the bottom edges of the cross section and constraint equations were employed at the top edge to obtain axisymmetric generalized plane strain conditions. Thus, similarly to the previously presented analytical approach the influence of the modeled phase pattern can be studied. This approach explicitly covers second order effects caused by the curvature of the fibers which is, of course, not possible in the MTM or any other Mean–Field approach based on Eshelby's theory for calculating the stress state within a composite reinforced by aligned el-

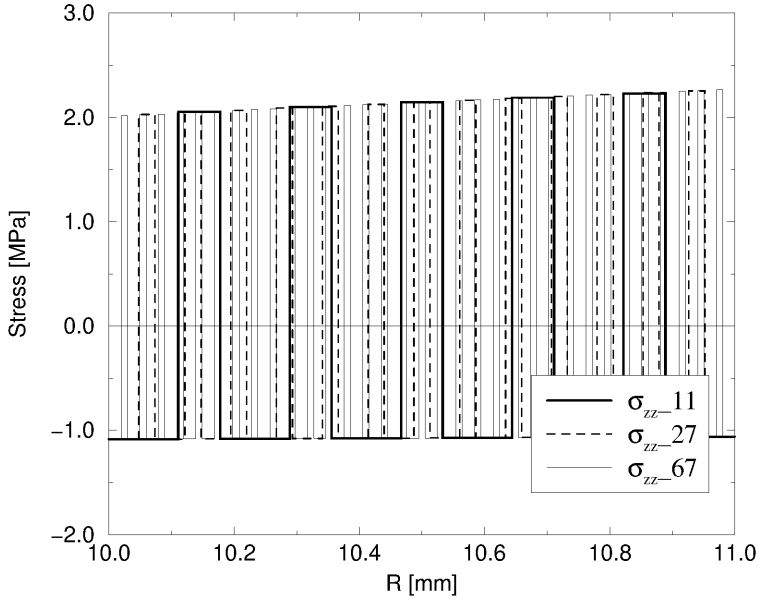

Figure 3.4: Distribution of axial stresses σ_{zz} for cylinders composed of 11, 27 and 67 layers, respectively, as a function of their radial position

lipsoidal inclusions.

In fig. 3.7 a comparison is given between the analytically determined results for a layered cylinder consisting of 67 layers and predictions for a fiber reinforced cylinder with the same constituents properties and volume fractions obtained by the MTM. Again the results are given as functions of the radius between R_i and R_a. The analytically determined circumferential stresses $\sigma_{\varphi\varphi}$_a67 (thin line jumping from compression to tension corresponding to the alternating layers) are compared with results of the MTM, represented by the circumferential stresses in the matrix phase ($\sigma_{\varphi\varphi}^{(m)}$), the reinforcing fibers ($\sigma_{\varphi\varphi}^{(i)}$) and an effective, i.e. averaged stress level ($\sigma_{\varphi\varphi}^{*}$). For the definition of the effective stresses in a composite material see chapter 2 eqn. 2.5. The overall behavior is similar for both models, the matrix material being in compression and the reinforcing material in tension, the latter increasing with increasing radius. Thus, for both models the effective stress changes from compression to tension with increasing radius, see $\sigma_{\varphi\varphi}^{*}$ for the MTM. There is, however, some difference for the circumferential stress within the reinforcing material, which appears to be mainly caused by the axial strain

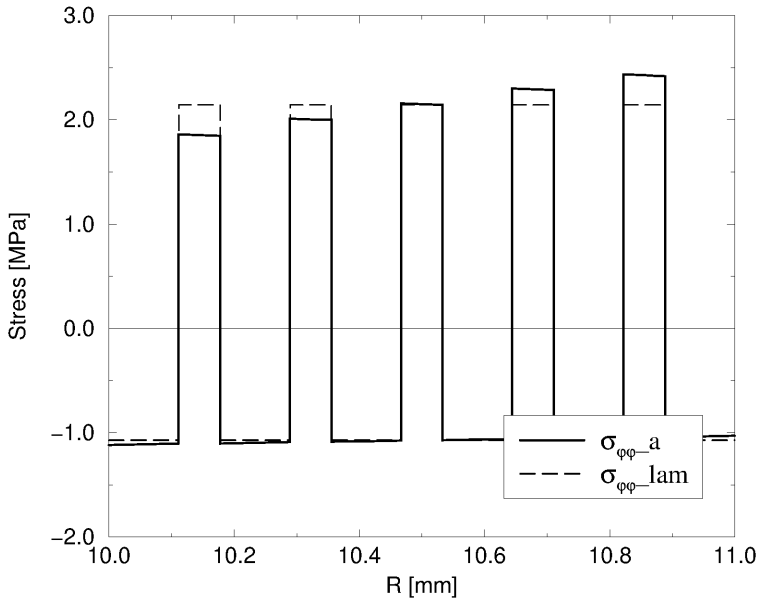

Figure 3.5: Comparison of circumferential stresses in a 11-layer laminate after a temperature change $\Delta T = 10$K, employing conventional lamination theory ($\sigma_{\varphi\varphi}$_lam) and the analytical solution technique ($\sigma_{\varphi\varphi}$_a).

coupling assumed in the multi-layer cylinder model.

In fig. 3.8 results for the fiber reinforced cylinder are compared between the two micromechanically based approaches, MTM and HCT. Since the implementation of the HCT approach does not allow a continuous variation of the dimensions of the modeled area for a given volume fraction and fiber diameter, the global geometries of both models (MTM and HCT) were chosen to be identical. For this reason the external radius has a value of $R_a = 11.15$mm instead of $R_a = 11$mm. All other conditions remain unchanged.

For the sake of comparison the MTM results for the circumferential stresses ($\sigma_{\varphi\varphi}^{(m)}$), ($\sigma_{\varphi\varphi}^{(i)}$) and ($\sigma_{\varphi\varphi}^{*}$) are plotted together with results obtain by two HCT models with 63 fibers (HCT_ A) and 1036 fibers (HCT_ B), respectively. The predictions are in very good agreement, i.e. there is no major error caused by either the curvature of the constituents (compare MTM and HCT models) or by the degree of refinement of the phase pattern, i.e. the modeled fiber

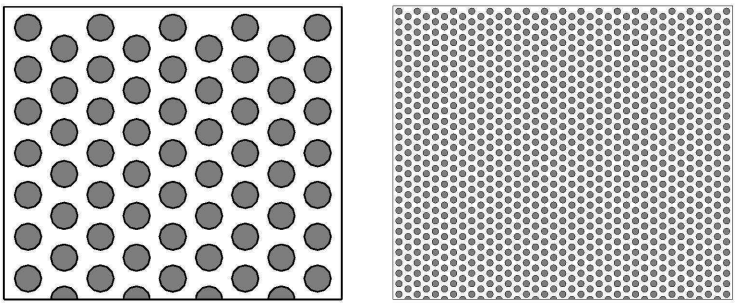

Figure 3.6: Cross sections of two axisymmetric fiber reinforced composite ring models containing 63 (model A, left) and 1036 fibers (model B, right), generated via the HCT approach

diameter (compare HCT_A vs. HCT_B).
On the basis of these results it can be stated that, as long as small fiber curvatures are concerned, both modeling approaches, MTM and HCT, are suitable modeling tools that give reliable results on the macro and on the phase level.

In the final part of this section a configuration with a more pronounced curvature is investigated. Here, the ratio of outer to inner diameter of the composite cylinder has been increased, $R_i = 1\text{mm}$ and $R_a = 11\text{mm}$.
In figs. 3.9, 3.10 and 3.11 the results for the analytical cylinder model are presented. In comparison to the previous results (figs. 3.2, 3.3, 3.4) it becomes obvious that the strong curvature has a marked influence on the circumferential stresses of the stiffer layer. The previously observed effect, that the effective stresses change from compression to tension moving from the inner to the outer diameter, is now much more pronounced. Close to the inner surface even the stiffer layers are under circumferential compression. These effects act very locally, i.e. close to the inner surface, and are accompanied and caused by non-negligible radial stresses. Thus the results of the analytical models exhibit a major dependence on the number of layers used for the model.
The same cylinder was modeled as a fiber reinforced cylinder by the MTM

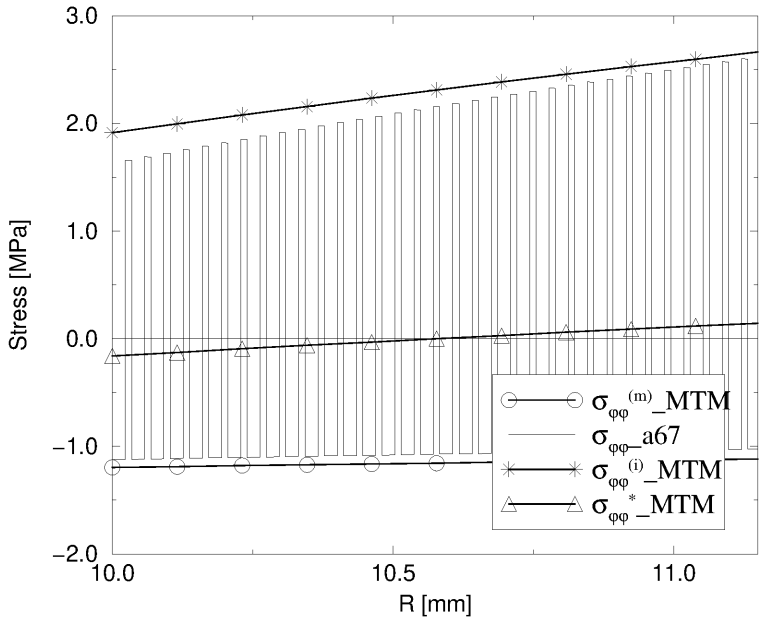

Figure 3.7: Comparison of circumferential stresses after a temperature change of $\Delta T = 10$K determined analytically for a layered cylinder and predicted for a fiber reinforced composite using the MTM

and the HCT approaches, and a similar behavior was found. Because the stress distribution close to the inner surface is mainly influenced by the overall stress state, i.e. it is not a second order effect caused by the curvature of the individual fibers, the MTM also represents this behavior in an appropriate manner. Like in the analytical solution, which is based on a finite number of layers, for the HCT approach, which uses on a finite number of fibers, the stress distribution at the innermost positions exhibits a strong dependence on the refinement of the phase pattern. Thus, in both cases by choosing an excessively coarse phase pattern the compressive circumferential stresses of inclusions are underestimated.

To conclude this chapter it can be stated that the Mori–Tanaka method is capable of describing composites reinforced by curved aligned long fibers without significant loss of accuracy due to the fiber curvature, as long as the fiber diameter is small compared to the cylinder diameter. In addition, it

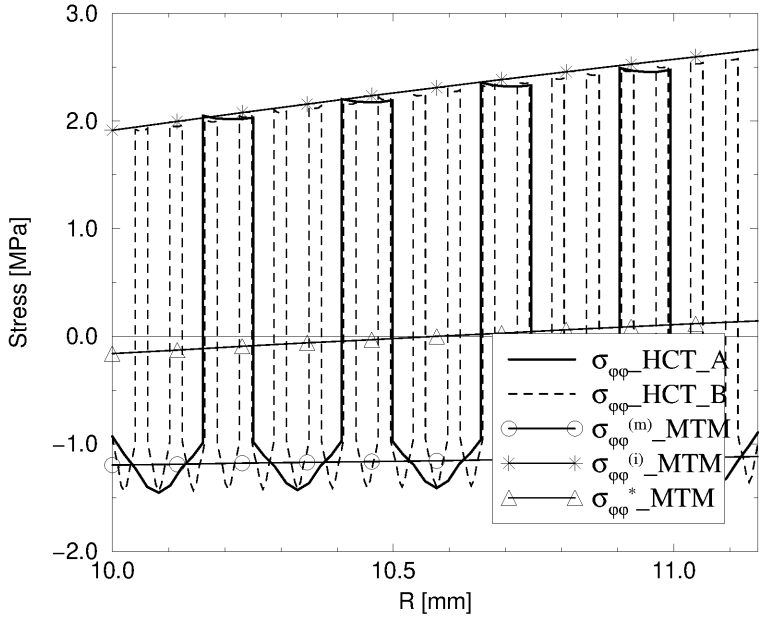

Figure 3.8: Comparison of circumferential stresses after a temperature change of $\Delta T = 10$K predicted for a fiber reinforced ring by the MTM and by two HCT models

was found that as long as the ratio of outer to inner diameters of circumferentially continuous fiber reinforced axisymmetric bodies does not become too large, approaches using simplified phase patterns of the composite, e.g. the hexagonal cell tiling approaches, represent the real composite behavior in proper manner.

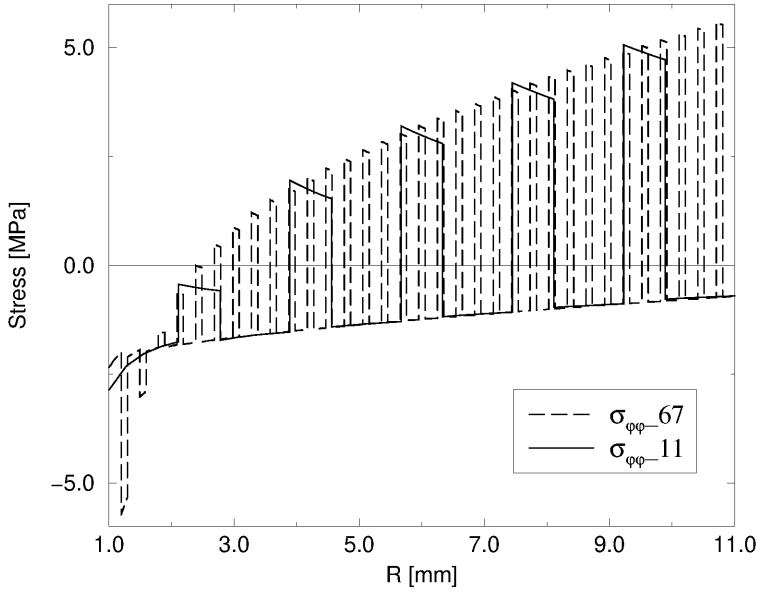

Figure 3.9: Circumferential stresses for a layered cylinder with strong curvature composed of 11 and 67 layers, respectively

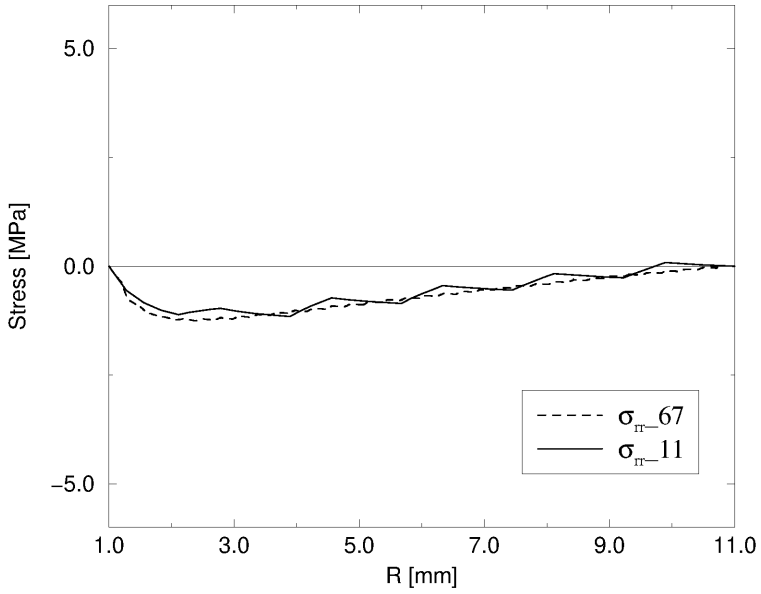

Figure 3.10: Radial stresses for a layered cylinder with strong curvature composed of 11 and 67 layers, respectively

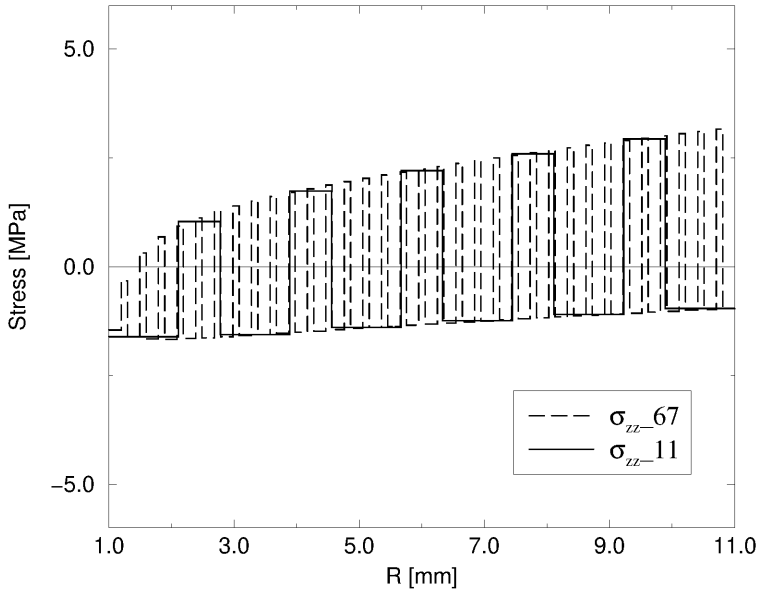

Figure 3.11: Axial stresses for a layered cylinder with strong curvature composed of 11 and 67 layers, respectively

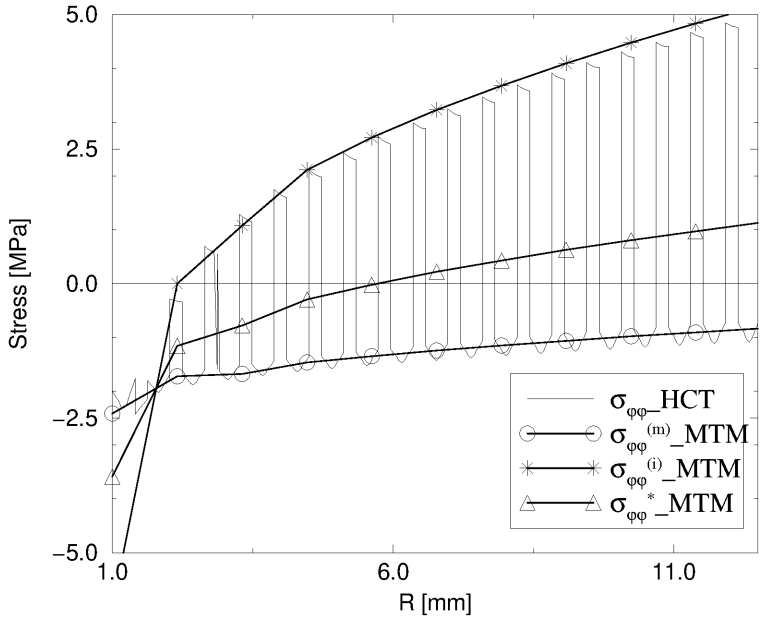

Figure 3.12: Circumferential stresses for a fiber reinforced cylinder with strong curvature – comparison of MTM and HCT results

Chapter 4

Material characterization

The objectives of this chapter are to derive effective material data for composites envisaged for the reinforcing insert. Consequently the results should support the selection of the proper constituents from the mechanical point of view. Considering the individual benefits of the available micromechanical tools a first screening on the elastic and inelastic properties is accomplished by the standard mean field methods. Whereas nonlinear material characterizations use either unit cell approaches or the incremental formulation of the Mori–Tanaka method.

4.1 First screening of the effective elastic–inelastic properties of Mg– and Al–MMCs

To obtain a quick overview on the mechanical characteristics of carbon fiber (T300) reinforced MMCs, we start with estimating the effective isothermal elastic behavior from the material parameters of the constituents. In figs. 4.1, 4.2, 4.3 and 4.4 the effective Young's and shear moduli, the effective Poisson's ratios and the effective coefficients of thermal expansion (CTE), respectively, are shown in axial and transversal directions as a function of the volume fraction of reinforcement. These results as well as the predictions for the uniaxial and shear yield strength, figs. 4.5 and 4.6, are based on the Mori–Tanaka method (MTM), comparing MMCs constituents of carbon fiber (T300) in commercially pure Al (Al99.9), in AlMg5, and in AZ91D.

The axial Young's modulus for a longfiber reinforced composite is an almost linear function of the reinforcement volume fraction, compare fig. 4.1 and for $\xi = 0.5$ the axial Young's modulus for the magnesium matrix composite is predicted as $E_a = 1.3 \cdot 10^5 \mathrm{N/mm}^2$, i.e. three times the Young's modulus of the matrix. The effective elastic response in transverse direction exhibits an unusual behavior for reinforced metals. In contrast to MMCs reinforced by ceramic reinforcements, which are in general isotropic and stiffer than the matrix, the anisotropic behavior of carbon fibers (stiff in fiber direction and compliant in transverse direction) leads to decreasing stiffness with an increasing fiber volume fraction. A similar behavior is evident for the effec-

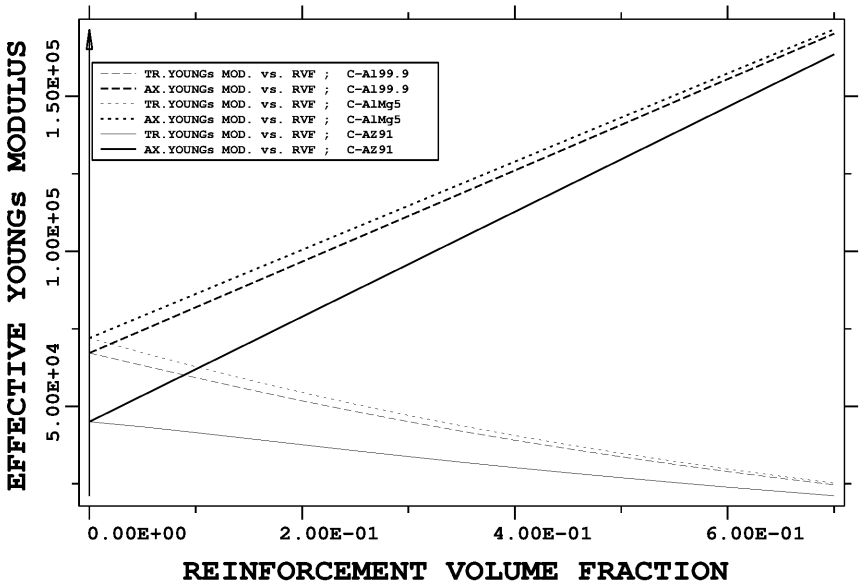

Figure 4.1: Predictions for the effective Young's moduli in axial and transversal directions for carbon fiber (T300) reinforced composites comparing the matrix materials Al99.9, AlMg5, and AZ91D

tive shear moduli given in fig. 4.2 in axial as well as in transverse directions. The effective Poisson's ratios vs. the volume fraction of reinforcements are given in fig. 4.3. Whereas the axial Poisson's ratio decreases with increasing fiber volume fractions, the transversal Poisson's ratio slightly increases

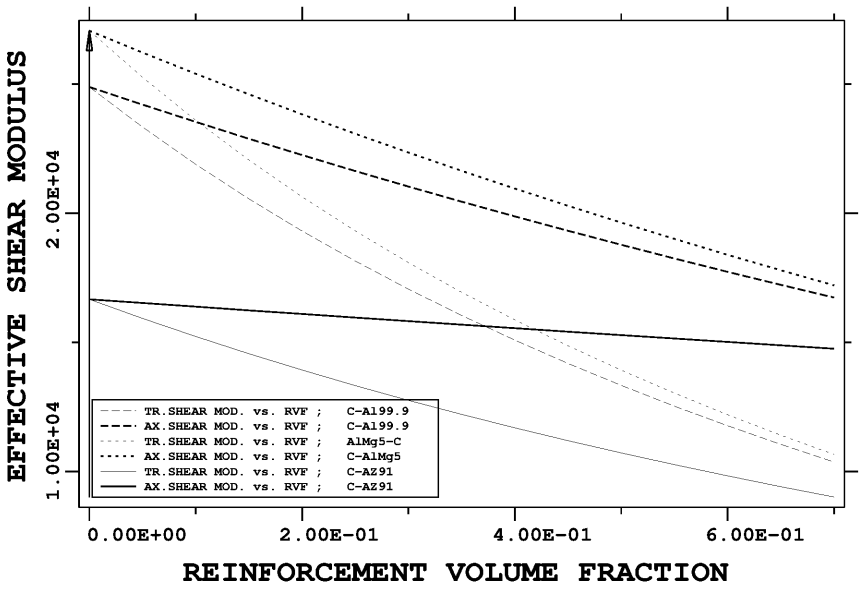

Figure 4.2: Predictions for the effective shear moduli in axial and transversal directions for carbon fiber (T300) reinforced composites comparing the matrix materials Al99.9, AlMg5, and AZ91D

for small volume fraction and then decreases for higher fractions, which is a consequence of a constraint effect in fiber direction that prevails over the transverse properties of the fibers. A similar effect is present for the transversal thermal expansion behavior, fig. 4.4, where the constraint of the thermal expansion in longitudinal direction in combination with the Poisson effect leads to a maximum of transversal effective CTEs at some small volume fraction. It is also evident that, due to the negative axial CTE of carbon fibers the effective axial CTE can be adjusted over a wide range by varying the fiber volume fraction. For a reinforcement volume fraction of 50 % the axial CTE reaches a value of $4.3 \cdot 10^{-6}\mathrm{K}^{-1}$ for an elastic C-AZ91 composite. It should be mentioned that for composite materials the CTE is no longer a simply material constant, because once yielding takes place the CTE becomes time– and load history dependent, so that only instantaneous values can be determined for an elasto-plastic composite's CTE.
In figs. 4.5 and 4.6 estimates for the effective yield limits under uniaxial and

pure shear loading, respectively, are given. An enhancement of the axial yield limit due to the fiber reinforcement is evident, whereas the transversal uniaxial as well as the shear yield limits are dominated by the matrix. It should be noted that for all calculations in this section the material is assumed to be initially stress free.

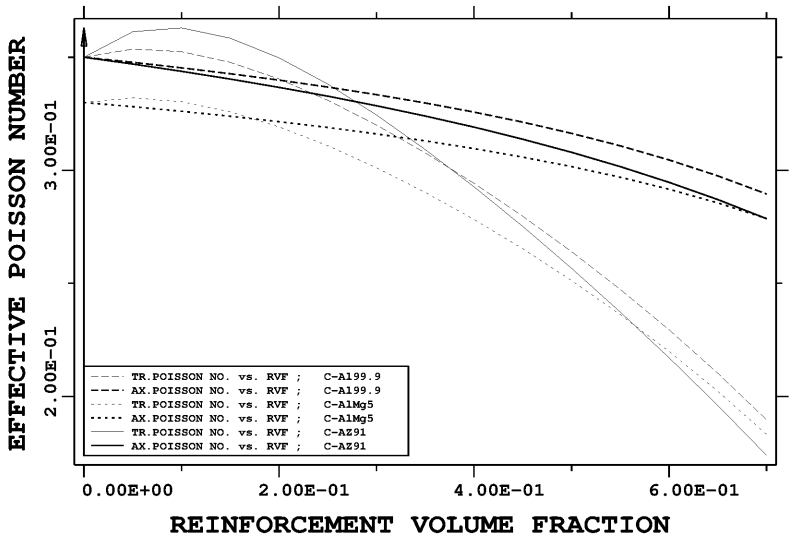

Figure 4.3: Predictions for the axial and transversal effective Poisson's ratios for carbon fiber (T300) reinforced composites comparing the matrix materials Al99.9, AlMg5, and AZ91D

In addition a first statement on the composites' response to thermal loadings can be given using the MTM. The mismatch between the CTE's of the constituents gives rise to self equilibrating microstresses, which after a sufficiently large temperature excursion depending on the mechanical loading cause the matrix to yield. Figure 4.7 presents predictions for this critical temperature change assuming initially stress free constituents and no external loading. The material combinations C–AlMg5 and C–AZ91D lead to moderate values for the critical temperature change, e.g. for $\xi = 0.5$ temperatures of 124°C and 164°C, respectively, were found. The combination C–Al99.9 leads to rather small values (25°C for $\xi = 0.5$), a fact which is the

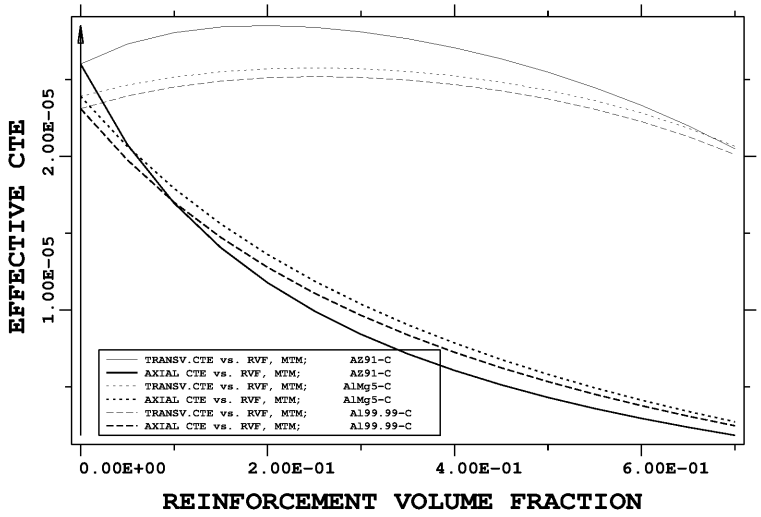

Figure 4.4: Predictions for the axial and transversal initial coefficients of thermal expansion (CTE) for carbon fiber (T300) reinforced composites at room temperature comparing the matrix materials Al99.9, AlMg5, and AZ91D

consequence of the poor resistance to plastic deformations known for pure Al. Consequently we can deduce that cyclic thermal loading (e.g. between service–rest temperatures of composite component) leads to cyclic plastic deformation of the pure Al matrix, so that the fatigue behavior has to be considered seriously. It should be mentioned that in the present predictions the material properties of the constituents were assumed to be temperature independent, which might lead to some overestimations for the critical temperature change. More accurate estimates can be obtained from unit cell type models with temperature dependent material properties, compare the following section 4.2.

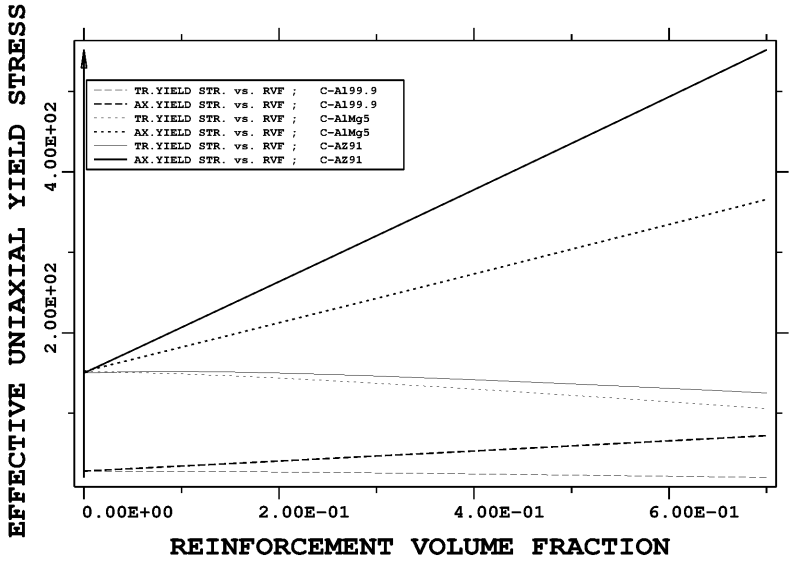

Figure 4.5: Predictions for the yield limits under uniaxial loading in axial and transversal directions, respectively, for carbon fiber (T300) reinforced composites comparing the matrix materials Al99.9, AlMg5, and AZ91D

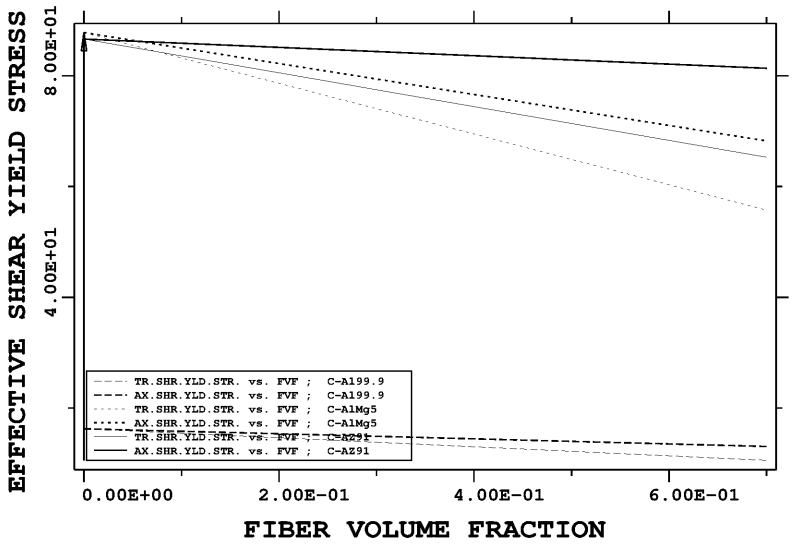

Figure 4.6: Predictions for the axial and transversal shear yield limits for carbon fiber (T300) reinforced composites comparing the matrix materials Al99.9, AlMg5, and AZ91D

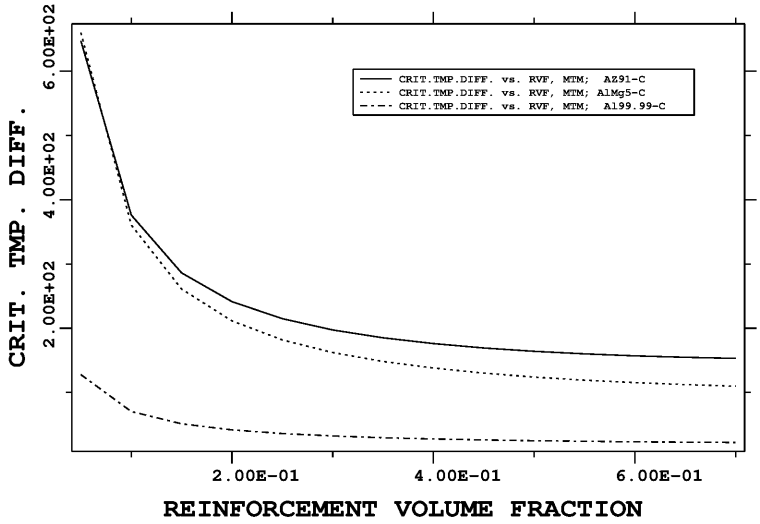

Figure 4.7: Predictions for a critical homogeneous temperature change that leads to yielding of the matrix material of initially stress free composites. A comparison is given for carbon fiber (T300) reinforced AZ91D, AlMg5, and Al99.9 composites

4.2 Elasto–plastic response

A more accurate numerical way for modeling the thermo–elasto–plastic response of fiber reinforced composites is by the use of unit cells, compare chapter 2. Nevertheless we additionally make use of the incremental Mori–Tanaka approach (IMT), in order to check its accuracy, and on the other hand because the IMT is not restricted to a limited number of loading directions, so that arbitrary loading cases can be investigated which would violate symmetry conditions used in the present unit cell models. The stress–strain responses derived by the IMT method came from single element tests, i.e. the load was applied to a cube shaped 8-node brick element employing the user supplied IMT- material subroutine (UMAT) in ABAQUS for the material description on the integration point level.

The following results are restricted to a carbon–AZ91 composite. The elasto–plastic stress–strain response of the matrix material is modeled in a simplified way as a bilinear function.

At first uniaxial tension in fiber direction and perpendicular to the fiber direction, respectively, are modeled and the strain responses are investigated for 40 %vol of aligned fibers. The results are compared to predictions from Finite Element unit cell models for a periodic hexagonal fiber arrangement, compare fig. 2.2, the same material properties for the constituents being used in both approaches. For unidirectional loading in fiber direction, see fig. 4.8, the agreement is excellent, the stress and strain distributions in the unit cells being close to the mean field assumption. Also for transverse loading, see fig. 4.9, good agreement is found. It should be noted that for hexagonal periodic unit cell models the transverse isotropy with respect to the overall behavior is broken under transverse loading in the elasto–plastic regime, compare the dashed and dotted lines in fig. 4.9. For a detailed discussion see [14]. The IMT-results tend to over predict the onset of yielding, which is a well known effect since standard mean field methods cannot account for micro fluctuations of the stress field.

Also for the transverse shear response a good agreement between unit cell and IMT method was found, as shown in fig. 4.10.

In fig. 4.11 the IMT predictions for the stress–strain response of a 30%vol car-

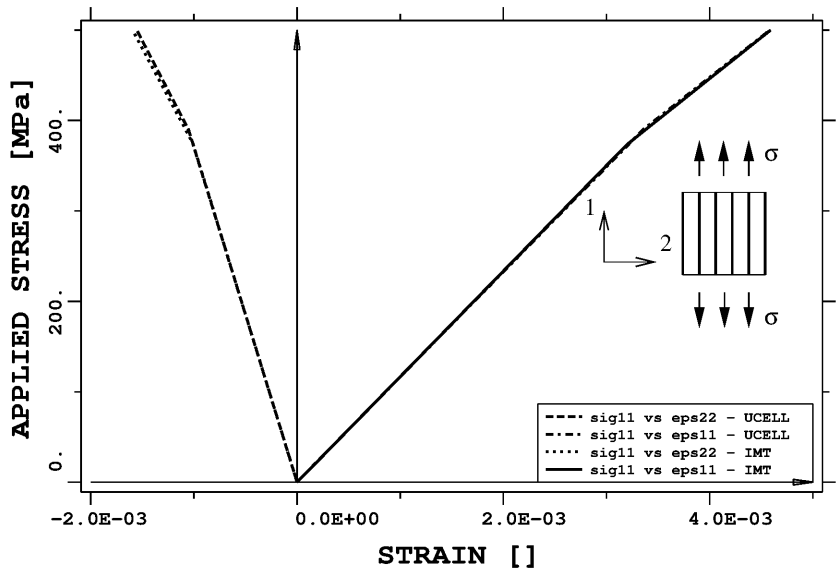

Figure 4.8: Predicted effective stress–strain diagram of a 40%vol carbon fiber–AZ91 composite subjected uniaxial loading in fiber direction at room temperature; comparison between predictions of the incremental Mori–Tanaka method (IMT) and a Finite Element unit cell approach

bon fiber – Mg(AZ91D) composite subjected to uniaxial loading employing various inclination angles with respect to the fiber and the loading direction are given. It is obvious that the stiffness is significantly reduced even for small angles of inclination. In the transverse direction the sensitivity is much less pronounced. For inclination angles greater than 30° the yield strength is found to be smaller than the yield strength of the pure matrix material, which is a consequence of the compliant transverse behavior of carbon fibers. The composite's response to pure shear loading with different inclination angles between the fiber and the loading direction is given in fig. 4.12. For an angle of inclination $\phi = 45°$ the material exhibits a stiff response, since one of the principal stress axes coincides with the fiber direction. For shear loading in and perpendicular to the fiber direction a compliant stress–strain response is predicted, because in these case the normal stresses in the fibers are almost zero.

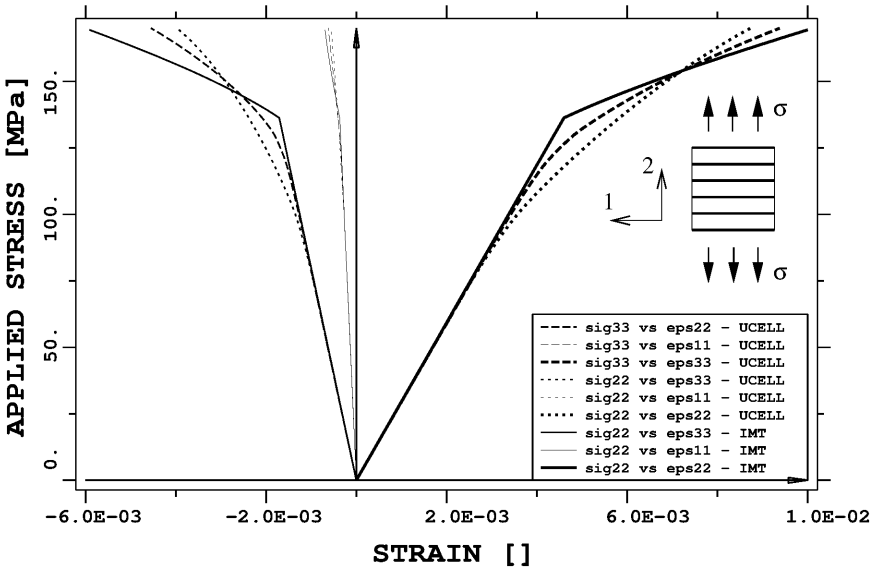

Figure 4.9: Effective stress–strain diagram of a 40%vol carbon fiber–AZ91 composite subjected to uniaxial transversal tension; comparison between predictions of the incremental Mori–Tanaka method (IMT) and a Finite Element unit cell approach

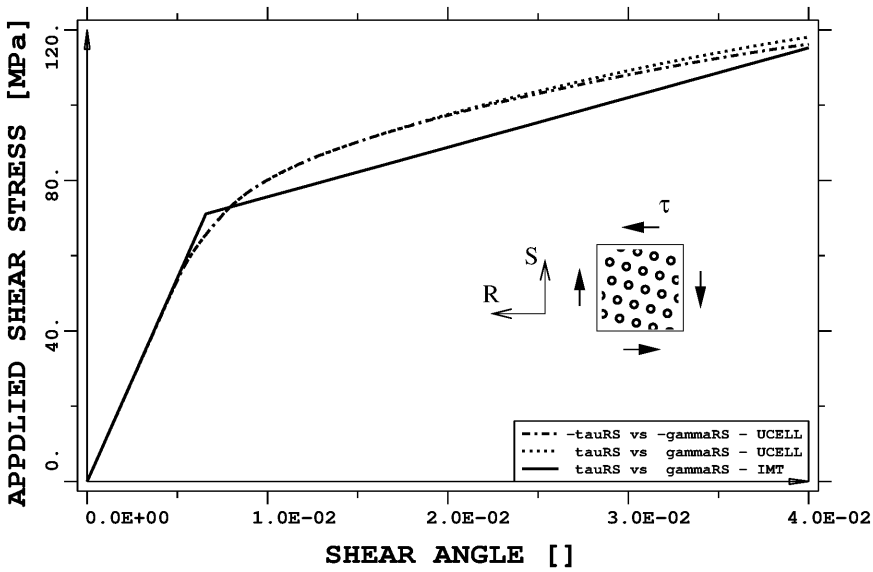

Figure 4.10: Effective stress–strain diagram of a 40%vol carbon fiber–AZ91 composite subjected to pure transversal shear loading; Comparison between predictions of the incremental Mori–Tanaka method (IMT) and a Finite Element unit cell approach

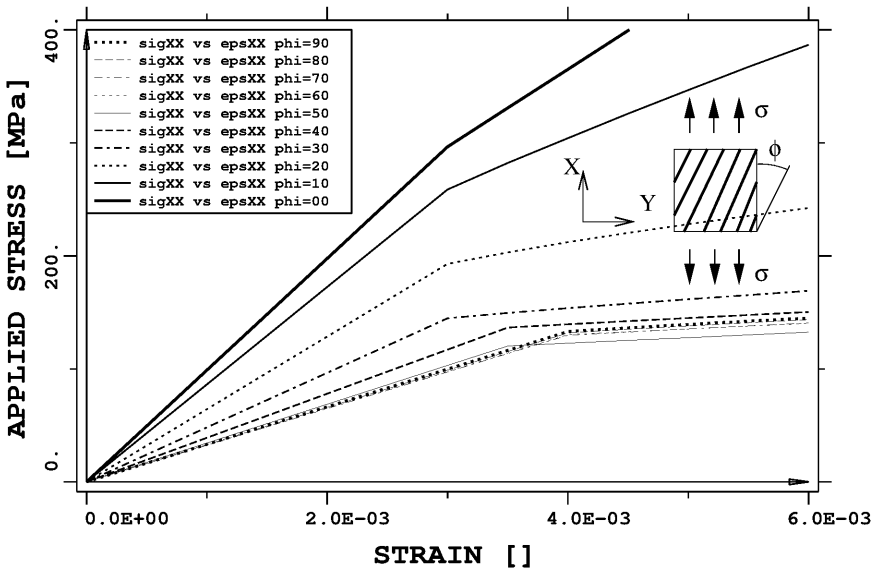

Figure 4.11: Predicted effective stress–strain response of a T300–AZ91D MMC to unidirectionally loading applied at different inclination angles with respect to the fiber directions

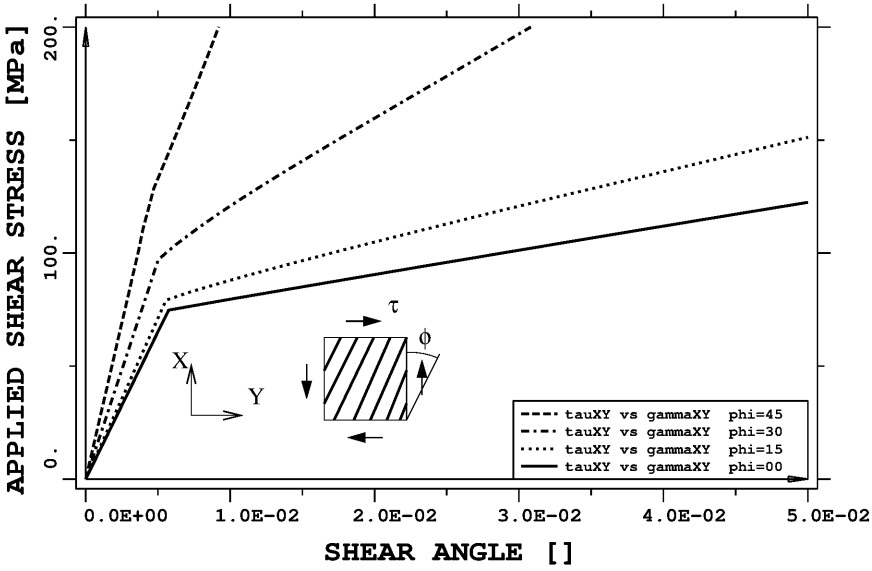

Figure 4.12: Predicted effective stress–strain response of a T300–AZ91D MMC to pure shear loading applied at different inclination angles with respect to the fiber directions

Although the MTM provides some qualitative aspects of the behavior of composites subjected to thermal loading, compare figs. 4.4 and 4.7, especially the thermal expansion behavior should be considered in closer detail. Thus a unit cell approach is employed to investigate the expansion behavior under cyclic thermal loadings. For both envisaged material combinations (Altex–Al and C–AZ91D) a unit cell with $\xi = 0.58$ is used. The thermal cycling of the Altex–Al composite starts at a temperature of 350°C, cooling down to 0°C being followed by heating to the initial temperature and a further thermal cycle. The axial (ε_{zz}) and transversal (ε_{xx}) strains exhibit hysteresis loops, indicating the accumulation of plastic deformation in each thermal cycle, compare fig. 4.13. Looking at the effective thermal expansion behavior of the Altex–Al MMC, see fig. 4.14, it is found that α_A, the axial CTE, decreases immediately after the onset of cooling while α_T, the transversal CTE, increases, followed by a nearly linear decrease for both α_A and α_T during further cooling down. At elevated temperatures (350°C at the beginning) the yield limit for the Al–matrix is very small, causing the matrix to yield right after the onset of cooling, which is the reason for the first changes of the instantaneous CTEs. After the matrix has yielded the instantaneous effective axial expansion coefficient α_A is dominated by the fiber properties, i.e. α_A is close to α_{Altex}. The constrained expansion in fiber direction causes an increase of α_T simultaneously to the decrease of α_A. The subsequent decrease of α_A and α_T is caused by the temperature dependence found for the CTE of Altex with a small influence of the hardening behavior of the Al–matrix.

If the temperature time gradient changes its sign the instantaneous effective CTEs exhibit a discontinuos change from the fiber dominated state to a regime where the matrix behaves elastically and thus has more influence on the effective thermal expansion behavior of the composite. Depending on the number of cycles the temperature change ΔT which causes the matrix material to plastify after changing the loading direction is $\Delta T \approx$ 30–40°C for heating and $\Delta T \approx 10$°C for cooling. (Compare predictions of the critical temperature change 4.7 assuming a initially stress free composite.)

Figure 4.15 and 4.16 present a similar simulation for the C–AZ91D composite. The thermal strain hysteresis is narrower compared to the Al–composite,

i.e. although ΔT was increased to 400°C the Mg matrix exhibits much less plastic deformation during thermal loading. The temperature intervals in which both constituents behave elastically are much larger, having values of $\Delta T \approx 200$°C in both "loading directions". Due to the negative axial CTE of the carbon fibers also the effective axial thermal expansion behavior exhibits rather small values especially in the fiber dominated state when the matrix has plastified. Due to the pronounced temperature dependence of the Young's modulus, the yield limit, as well as the hardening properties of the Mg–matrix the instantaneous effective CTEs exhibit an even more pronouced load history dependence then predicted for the Altex–Al composite. To demonstrate the mechanical load history dependence of a carbon–Mg composite the CTEs during a thermal loading of $\Delta T = +400$K of a initially stress free $\sigma_{zz} = 0$ MPa and prestressed $\sigma_{zz} = \pm 300$MPa composite ($\xi = 0.4$) is shown in fig. 4.17

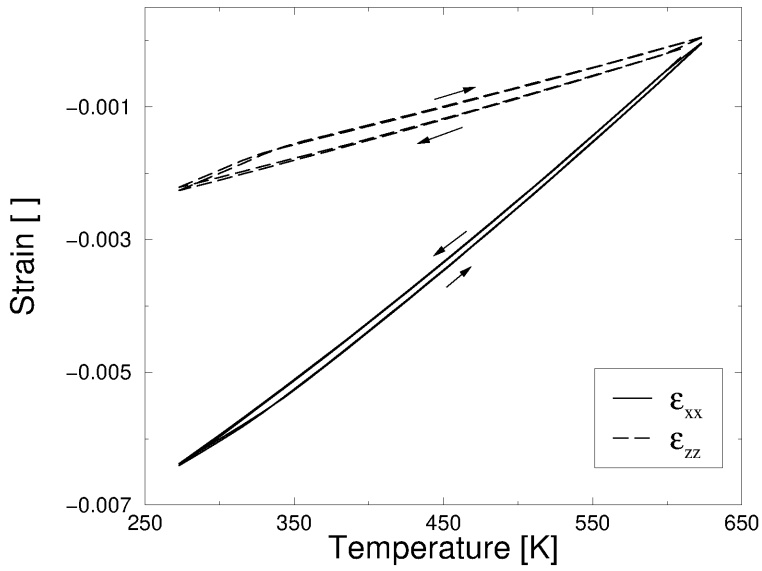

Figure 4.13: Predicted effective axial and transversal strain responses to cyclic thermal loading of an initially stress free Altex–Al99.9 composite ($\xi = 0.58$)

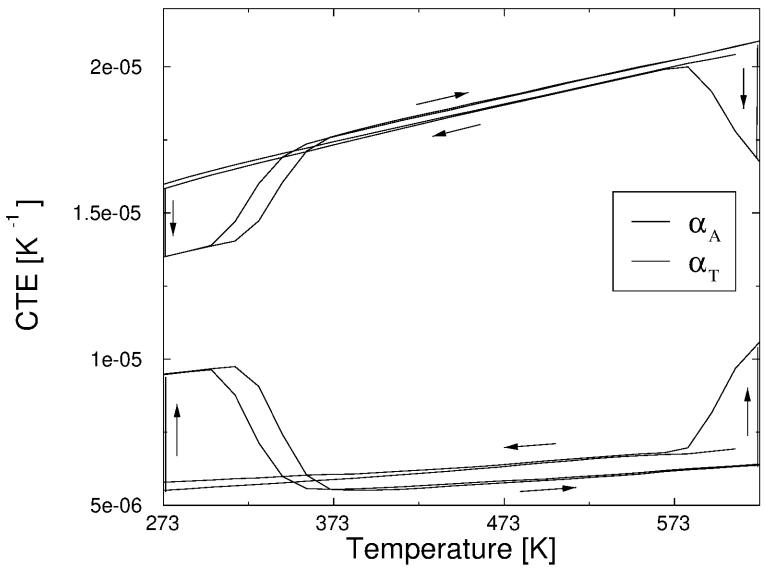

Figure 4.14: Predicted effective axial and transversal coefficients of thermal expansion responses to cyclic thermal loading of an initially stress free Altex–Al99.9 composite ($\xi = 0.58$)

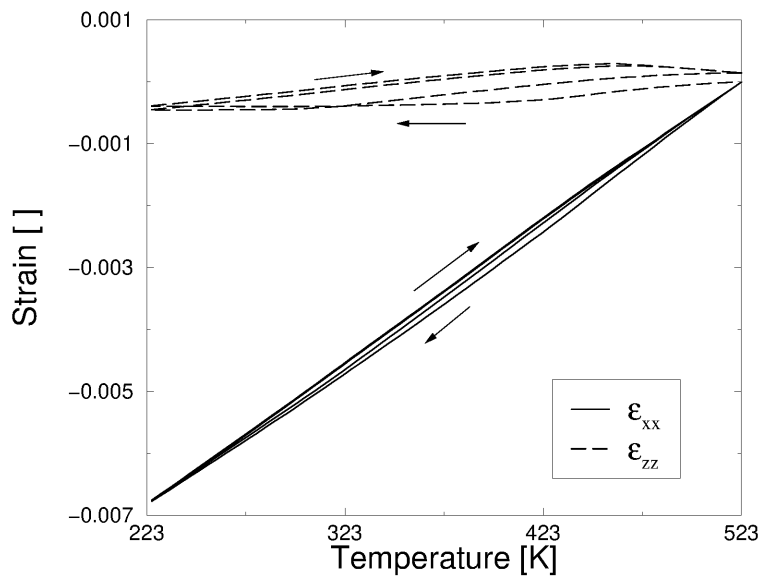

Figure 4.15: Predicted effective axial and transversal strain responses to cyclic thermal loading of an initially stress free carbon–AZ91D composite ($\xi = 0.58$)

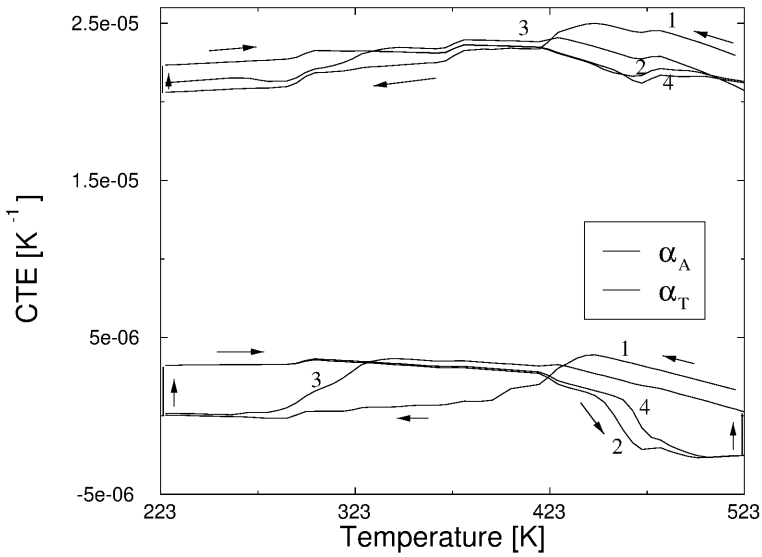

Figure 4.16: Predicted effective axial and transversal coefficient of thermal expansion responses to cyclic thermal loading of an initially stress free carbon–AZ91D composite ($\xi = 0.58$)

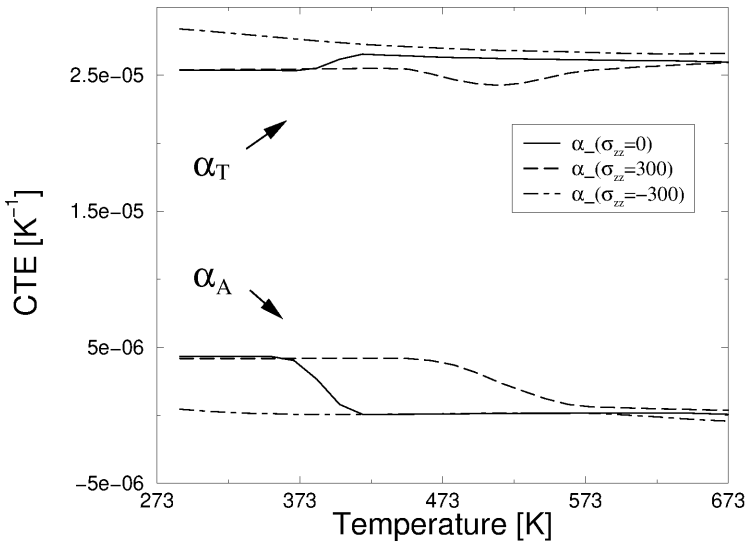

Figure 4.17: Predicted effective axial and transversal coefficient of thermal expansion responses to thermal loading of $\Delta = 400$K of initially stress free $\sigma_{zz} = 0$ MPa and prestressed $\sigma_{zz} = \pm 300$MPa carbon–AZ91D composite ($\xi = 0.4$)

Chapter 5

Free edge effects at bimaterial junctions

A consequence of producing selectively reinforced components, where the reinforcing material is restricted isolated regions, interfaces occur on the macroscale between the reinforced and the unreinforced materials. At intersections between material interfaces and free edges of multi material structures complex tri-axial stress states occur which often are critical with respect to damage. When the stress fields are studied in terms of a bimaterial junction problem using homogenized material descriptions singular stress fields are typically predicted. In the following section some simply shaped hybrid components are analyzed under thermal and mechanical loading, special consideration being given to the singular stress fields.

An analytical method was utilized to determine the singular stress fields close to the intersection points of the material interface and the free surface. It employs the Airy stress function to set up the corresponding boundary value problem, which is solved via the Mellin transform. In addition, ways for improving the interface design with respect to the free edge effect are derived for some given hybrid components.

Using a combined macro–micromechanical embedding approach it is demonstrated in the second part of this chapter, that under certain conditions the stress singularities disappear when the heterogeneous micro structure of a selectively reinforced component is accounted for explicitly.

5.1 Singular stress fields at bimaterial junctions

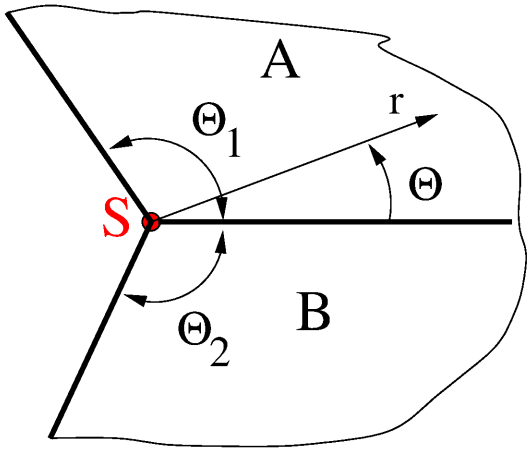

Figure 5.1: Sketch of the generic bimaterial wedge problem

Assuming two bonded wedges of dissimilar homogeneous materials, as shown in fig. 5.1, under arbitrary loading conditions, investigations based on continuum mechanics exhibit a singular behavior of the stress and strain fields at the intersection point of the material interface and the free surface. This is a consequence of the step-like, i.e. discontinuous, variation of the material parameters at the interface. An analytical solution of the so called bimaterial wedge problem was derived independently by Bogy [13], and by Hein and Erdogan [50] who solved the problem of two bonded isotropic elastic dissimilar wedges in 1971. Following their results the stress field in the vicinity of the singularity can be described by the expression

$$\sigma_{ij}(r,\theta) = K r^{-\lambda}\, F_{ij}(\theta) \tag{5.1}$$

where polar coordinates (r,θ) are used and the origin of the coordinate system is taken to lie at the intersection of the interface with the free surface. λ is the order of the singularity, which is a function of the material constants and the geometry only, whereas the function $F_{ij}(\Theta)$ and the stress intensity factor K also depend on the boundary conditions.

In the last decade considerable efforts were aimed at determining the singular stress fields for various geometries and loading conditions. The employed solution methods can be divided into analytical, numerical and combined methods. The analytical solutions are generally based on the simplifying assumptions of two bonded semi-infinite plates and isotropic material properties, e.g. [12, 13, 50, 55, 90, 107]. Analytical studies of the singularities in compounds of anisotropic materials have been presented in [66, 73].
For arbitrarily shaped components combined analytical–numerical ([65, 77]) or purely numerical methods have been employed. The majority of the numerical investigations are based on the Finite Element Method (FEM), compare e.g. [49, 42, 84, 87]. In [108] different numerical solution techniques like the Finite Difference Method, the Boundary Element Method and the Finite Element Method are discussed with respect to the accuracy of their results. It is demonstrated that the stress and strain fields are correctly described by the FEM (using fine meshes of standard continuum elements) except in the elements closest to the intersection point. Comprehensive overviews on the determination of stress singularities are given in [43, 110].

5.2 Analytical treatment of the bimaterial wedge problem

The plane problem of two linear elastic bonded dissimilar wedges, shown in fig. 5.1, under thermo–mechanical loading conditions can be treated by introducing the Airy stress function [88]. The stress and displacement fields in two-dimensional polar coordinates are obtained by solving for the Airy stress function $\phi(r, \Theta)$ which satisfies the equation

$$\nabla^4 \phi = 0 \tag{5.2}$$

$$\text{with} \quad \nabla^2 = \frac{\partial^2}{\partial r^2} + \frac{1}{r}\frac{\partial}{\partial r} + \frac{1}{r^2}\frac{\partial^2}{\partial \Theta^2}.$$

In the absence of body forces the stresses and displacements in polar coordinates are related to ϕ by

$$\sigma_{rr} = \frac{1}{r}\frac{\partial\phi}{\partial r} + \frac{1}{r^2}\frac{\partial^2\phi}{\partial\Theta^2}, \qquad \sigma_{\Theta\Theta} = \frac{\partial^2\phi}{\partial r^2},$$
$$\sigma_{r\Theta} = -\frac{1}{r}\frac{\partial^2\phi}{\partial r\partial\Theta} + \frac{1}{r^2}\frac{\partial\phi}{\partial\Theta}, \tag{5.3}$$

and

$$\frac{\partial u_r}{\partial r} = \frac{1}{2G}\left[\frac{1}{r}\frac{\partial\phi}{\partial r} + \frac{1}{r^2}\frac{\partial^2\phi}{\partial\Theta^2} - (1-m/4)\nabla^2\phi\right],$$
$$\frac{\partial u_\Theta}{\partial r} - \frac{u_\Theta}{r} + \frac{1}{r}\frac{\partial u_r}{\partial\Theta} = \frac{1}{G}\left(-\frac{1}{r}\frac{\partial^2\phi}{\partial r\partial\Theta} + \frac{1}{r^2}\frac{\partial\phi}{\partial\Theta}\right), \tag{5.4}$$

respectively, where G is the shear modulus corresponding to domains **A** or **B**, compare fig. 5.1, and m takes the values of $m = 4(1-\nu)$ for plane strain or $m = 4(1+\nu)^{-1}$ for plane stress analysis, respectively. The stress and displacement components have to satisfy the boundary conditions

$$\sigma^A_{\Theta\Theta}(r,-\Theta_1) = N^A(r), \qquad \sigma^A_{r\Theta}(r,-\Theta_1) = T^A(r),$$
$$\sigma^B_{\Theta\Theta}(r,\Theta_2) = N^B(r), \qquad \sigma^B_{r\Theta}(r,\Theta_2) = T^B(r), \tag{5.5}$$

as well as the bonding conditions at the interface (continuity of tractions and displacements)

$$\sigma^A_{\Theta\Theta}(r,0) = \sigma^B_{\Theta\Theta}(r,0), \qquad \sigma^A_{r\Theta}(r,0) = \sigma^B_{r\Theta}(r,0),$$
$$u^A_r(r,0) = u^B_r(r,0), \qquad u^A_\Theta(r,0) = u^B_\Theta(r,0). \tag{5.6}$$

Here $N^A(r), T^A(r), N^B(r)$, and $T^B(r)$ stand for the normal and tangential components of the tractions at the surfaces of materials **A** and **B**, respectively. A powerful method for solving the above singular boundary value problems is the Mellin transform, [39, 101, 107].

The Mellin transform of a function $\phi(r,\Theta)$ has the following definition [63]:

$$\hat{\phi}(s,\Theta) = \int_0^\infty \phi(r,\Theta)r^{(s-1)}dr, \tag{5.7}$$

where s is the complex transform parameter, and the inverse Mellin transform is given by

$$\phi(r,\Theta) = \frac{1}{2\pi i}\int_{y-i\infty}^{y+i\infty} \hat{\phi}(s,\Theta)r^{-s}ds, \tag{5.8}$$

where y determines the path of the integration in the complex line integral. Of course, y must be chosen in such a way that the integral exists.
The application of the Mellin transform to eqn. (5.2) leads to an ordinary differential equation for $\hat{\phi}(s,\Theta)$ of the form

$$(D^2+s^2)[D^2+(s+2)^2]\hat{\phi}(s,\Theta)=0, \qquad (5.9)$$
$$\text{with} \quad D=\frac{\partial}{\partial\Theta},$$

which holds for both wedges **A** and **B**. A general solution for this equation in the transformed notation takes the form

$$\begin{aligned}\hat{\phi}(s,\Theta)= \quad & a(s)\sin(s\Theta)+b(s)\cos(s\Theta)+\\ & c(s)\sin(s\Theta+2\Theta)+d(s)\cos(s\Theta+2\Theta)\end{aligned} \qquad (5.10)$$

within materials **A** and **B**, respectively. Here $a(s)^A$, ... $d(s)^A$ for $\hat{\phi}(s,\Theta)^A$ and $a(s)^B$, ... $d(s)^B$ for $\hat{\phi}(s,\Theta)^B$ have to be determined through the transformation of eqn. (5.3) and from the transformed boundary and bonding conditions, eqns. (5.5) and (5.6). Now we end up with a system of eight equations and eight unknown coefficients $a(s)^A$, ... $d(s)^A$ and $a(s)^B$, ... $d(s)^B$, that depend on the transform parameter s.

$$\begin{aligned}
&-\sin(\Theta_1 s)a^A+\cos(\Theta_1 s)b^A-\sin(\Theta_1 s+2s)c^A+\cos(\Theta_1 s+2s)d^A=\\
&\hat{N}^A(s)/s(s+1) \qquad ,\\
&s\cos(\Theta_1 s)a^A+s\sin(\Theta_1 s)b^A+(s+2)\cos(\Theta_1+2s)c^A+\\
&(s+2)\sin(\Theta_1+2s)d^A=\hat{T}^A(s)/s+1 \qquad ,\\
&\sin(\Theta_2 s)a^B+\cos(\Theta_2 s)b^B+\sin(\Theta_2 s+2s)c^B+\cos(\Theta_2 s+2s)d^B=\\
&\hat{N}^B(s)/s(s+1) \qquad ,\\
&s\cos(\Theta_2 s)a^B-s\sin(\Theta_2 s)b^B+(s+2)\cos(\Theta_2+2s)c^B-\\
&(s+2)\sin(\Theta_2+2s)d^B=\hat{T}^B(s)/s+1 \qquad ,\\
&b^A+d^A-b^B-d^B=0 \qquad ,\\
&sa^A+(s+2)c^A-sa^B-(s+2)c^B=0 \qquad ,\\
&G^B sb^A+G^B(s+m^A)d^A-G^A sb^B-G^A(s+m^B)d^B=0 \quad ,\\
&G^B sa^A+G^B(s+2-m^A)c^A-G^A sa^B-G^A(s+2-m^B)c^B=0 \quad .
\end{aligned} \qquad (5.11)$$

In matrix notation this system can be written as

$$\mathbf{K}\,\mathbf{x} = \mathbf{d}. \tag{5.12}$$

When the Mellin transform is applied to eqn. (5.3), back transforming of the solution $\hat{\sigma}_{ij}$ via eqn. (5.8) gives expressions of the type

$$\sigma_{ij} = \frac{1}{2\pi i}\int_{y-i\infty}^{y+i\infty} \hat{\sigma}_{ij}(s,\Theta) r^{-(s+2)} ds \tag{5.13}$$

for the stress components. Comparison with eqn. (5.1) shows that the order of the singularity λ must be related to the transform parameter s by $\lambda = s + 2$. Furthermore, it can be shown that the solution of eqn. (5.8) is analytic in the open strip $-2 \leq \mathrm{Re}(s) \leq -1$ except for poles that may occur at the zeros of the determinant of the matrix $\mathbf{K}$. Thus λ, the order of the singularity can be determined from the eigenvalues of the matrix $\mathbf{K}$ defined in eqn. (5.12).

The solutions for $s > -1$ are unphysical, since the displacements at $r = 0$ would be infinite. From eqn. (5.7) it is obvious that one has to distinguish between two types of zeros, first, zeros lying within the interval $-2 < \mathrm{Re}(s_1) \leq -1$ and, second, zeros $s_2 = -2$. The latter ones correspond to $\lambda = 0$, and thus to a constant stress term σ_0, see [110]. For the first case we come up with singular stress fields of the type

$$\begin{aligned} &\sigma_{ij}(r,\Theta) = K r^{-\lambda} F_{ij}(\Theta) \\ &\text{if} \quad \lambda \in \mathbb{R}, \quad \text{or} \end{aligned} \tag{5.14}$$

$$\begin{aligned} \sigma_{ij}(r,\Theta) = &\quad K r^{-\zeta}\Big(\cos\left(\eta \log r F^c_{ij}(\Theta)\right) + \sin\left(\eta \log r F^s_{ij}(\Theta)\right)\Big) \\ \text{if} \quad \lambda = &\quad \zeta + i\eta \in \mathbb{C}. \end{aligned} \tag{5.15}$$

The global solution for the stress and displacement fields can be found by applying the inverse Mellin transform to the corresponding equation in the transformed notation. This can be done either numerically or analytically by using the residual principle [63].

From eqn. (5.10) it is obvious that the eigenvalues of the corresponding

boundary value problem are determined by the solution of a transcendental equation. In general this leads to an infinite number of eigenvalues. Thus for arbitrarily shaped finite geometries the stress field can be expressed as

$$\sigma_{ij}(r,\Theta)=\sum_{k=1}^{N}\frac{K_k}{(r/L)^{\lambda_k}}F_{ijk}(\Theta)+\sigma_{ij0}(\Theta). \tag{5.16}$$

Here L is a characteristic length of the structure, which will be discussed in the following section, and σ_{ij0} is the constant stress term, see [110]. However, for special cases like the plane problem of two isotropic elastic wedges with wedge angles $\Theta_1 = -\Theta_2 = \pi/2$ only one singular term exists [50]. For arbitrary wedge angles additional terms might occur, compare fig. 5.4 which will be discussed later on. Another well known special case of the bimaterial wedge problem that can be solved employing the above method is obtained by choosing $\Theta_1 = -\Theta_2 = \pi$, leading to the solutions for a crack in the line of bonding between two dissimilar isotropic half planes where the order of singularity is found to be $\lambda = 0.5 + i\eta$. For the even more specialized case of both wedges having the same material properties we come up with the solution of a semi–infinite crack in a homogeneous infinite medium, where $\lambda = 0.5$, compare [50]. For the present study the primary interest was to investigate the region affected by the singular stress field, and thus to determine the order of the singularity λ depending on the material parameters and on the geometrical influence of the angles (Θ_1, Θ_2).

5.2.1 Proper interface design in hybrid structures with respect to stress singularities

Looking at the cross section of the generic hybrid part (discussed in chapter 1, see fig. 1.1) we find two intersection points of the material interface with the free surface. Thus, assuming two dissimilar homogeneous materials, arbitrary loading conditions leads to singular stress fields at the intersection points **X** and **Y** marked in fig. 5.2 (possible singularities in the vicinity of the lower right corner of the insert are not discussed here).

For these particular cases, $\Theta_1 = -\Theta_2 = \pi/2$, at intersection point **X** and $\Theta_1 = \pi, \Theta_2 = -\pi/2$ at intersection point **Y**, respectively, we study the singular behavior analytically. For simplicity a plane strain state is assumed for

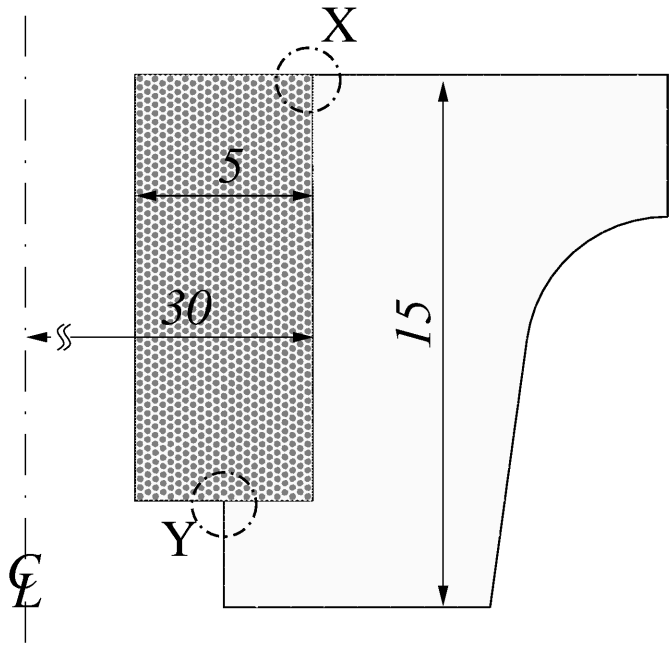

Figure 5.2: Cross section of a selectively reinforced ring. Regions where singular stress fields may occur are marked as **X** and **Y**

this study instead of an axisymmetric one. In fig. 5.3 the order of singularity λ versus the elastic contrast for the wedge angles $\Theta_1 = -\Theta_2 = \pi/2$, i.e. the configuration at intersection point **X**, is given. Such configurations appear in numerous applications, e.g. at free edges of laminates, or barrier coatings. In the logarithmic plot the order of singularity is found to be a symmetric function with respect to $G^A/G^B = 1$ if material **A** and material **B** have the same Poisson's ratio. With increasing elastic contrast the curves reach plateaus of approximately $\lambda = 0.3$. For $\nu_1 = \nu_2 = 0.3$ the maximum order of singularity reaches a value $\lambda_{max} = 0.289$. A variation of the Poisson's ratios leads to some shift for the order of singularity, but the global behavior is not affected. As mentioned before λ is a function of the elastic mismatch and the wedge angles only, so that this solution holds for arbitrary loading conditions.

For the second intersection point **Y** ($\Theta_1 = \pi$ and $\Theta_2 = -\pi/2$) the order of singularity is found to be close to 0.5 over a wide range of elastic contrasts, i.e. λ is close to values reached in front of a crack tip, compare fig. 5.4. For stiffness ratios smaller than 0.1, λ becomes complex and the value of the

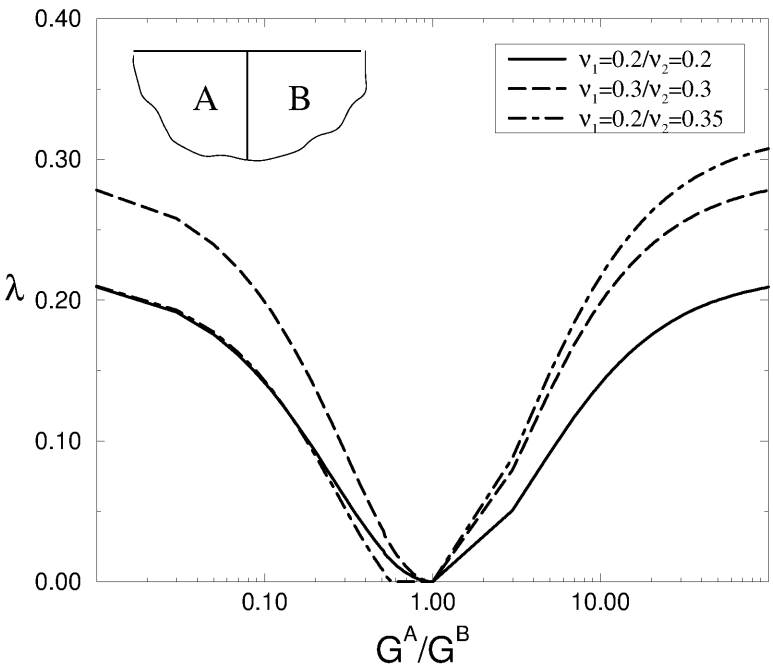

Figure 5.3: The order of singularity for λ for the wedge angles $\Theta_1 = -\Theta_2 = \pi/2$ versus elastic contrast G^A/G^B

real part is about 0.5. Close to $G^A/G^B = 0.1$ a bifurcation occurs, and for higher elastic contrasts two eigenvalues are found, so that the stress field has to be described using two singular terms, compare eqn. (5.16). Analogous solutions were given in [50].

For comparison a combination with an inclined interface $\Theta_1 = 2\pi/3$ and $\Theta_2 = \pi/3$ is shown in fig. 5.5. For $G^A/G^B \leq 0.1$ the singularity increases quite rapidly and becomes complex in a short interval around $G^A/G^B \approx 0.05$. The interval $0.1 \leq G^A/G^B \leq 1$ exhibits very small or zero values of λ. In comparison with fig. 5.3 this indicates the possibility of reducing the free edge effect by inclining the interface with respect to the free surface. Consequently, we are looking for an improved interface design with respect to the free edge effect at intersection points $\mathbf{X}$ and $\mathbf{Y}$, respectively.

We first discuss intersection point $\mathbf{X}$, for which the order of the singularity is plotted in fig. 5.6 as a function of the angle Θ_1 defined in fig. 5.1. The angle

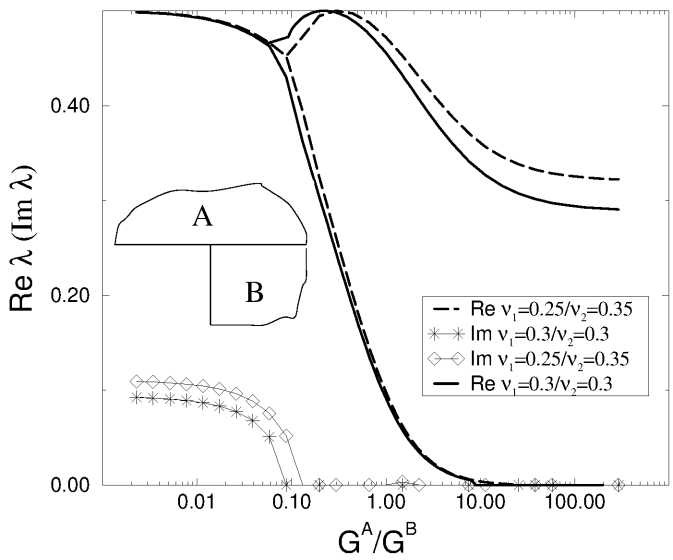

Figure 5.4: The order of singularity λ for a bimaterial wedge with $\Theta_1 = \pi$, $\Theta_2 = -\pi/2$, versus the elastic contrast G^A/G^B

of inclination of the interface is varied while keeping $\Theta_1 - \Theta_2 = \pi$. Three different elastic contrasts are considered to account for the mechanical properties of the constituences of a selectively reinforced component composed of a fiber reinforced MMC and monolithic (unreinforced) metal. $G^A/G^B = 3$ corresponding to the material combination T300–AZ91–AZ91 (i.e. carbon fiber reinforced magnesium combined with monolithic magnesium), $G^A/G^B = 1.8$ to Altex–Al–Al, and $G^A/G^B = 2.8$ to Altex–Al–AZ91, respectively. The effective elastic contrasts between reinforced and unreinforced material were obtained via the Mori–Tanaka method, see section 2.2. Since the analytical approach is restricted to isotropic material parameters only the elastic contrast in fiber direction is acounted for. Numerical investigations that explicitly account for the anisotropic material behavior demonstrate that the singularity is mainly influenced by the elastic mismatch in fiber direction, see chapter 5.3, so that this simplification seems to be justified for the current considerations.

The qualitative behavior of the order of singularity is predicted to be similar for all material combinations. The curves show two maxima for λ, one at

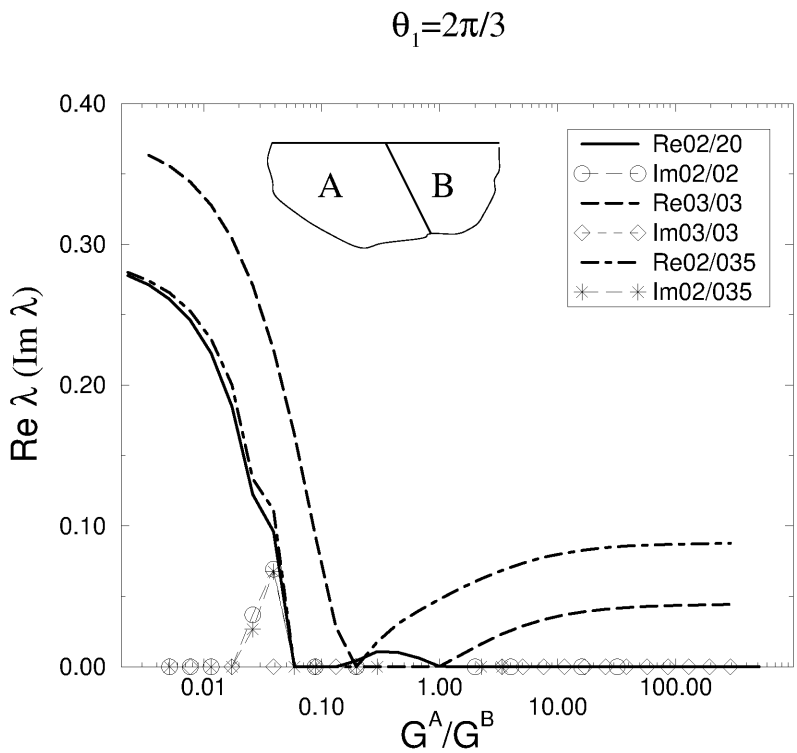

Figure 5.5: Order of singularity λ for $\Theta_1 = 2\pi/3$, $\Theta_2 = -\pi/3$

$\Theta_1 \approx 0.1\pi$ and another at $\Theta_1 \approx 0.55\pi$. For $\Theta_1 \approx \pi/3$ and for $\Theta_1 \geq 0.7\pi$ one obtains $\lambda = 0$, i.e. no singular stress field is found. This demonstrates the possibility of reducing or avoiding the singular free edge effect by a proper interface design.

For the hybrid structure sketched in fig. 5.2 this means that an inclination of the interface of more than 40° from the axial direction should avoid stress singularities in the vicinity of point **X**. For material combinations producing a weak interface between the inner ring and the outer casting such an inclined interface has the additional advantage of acting as geometrical anchor for the MMC insert.

In fig. 5.7 the order of the singularity λ is plotted as a function of the wedge angle Θ_2, with Θ_1 kept at a constant value of $\Theta_1 = \pi$. Only the first eigenvalue is displayed which is the more important one for the singular stress field

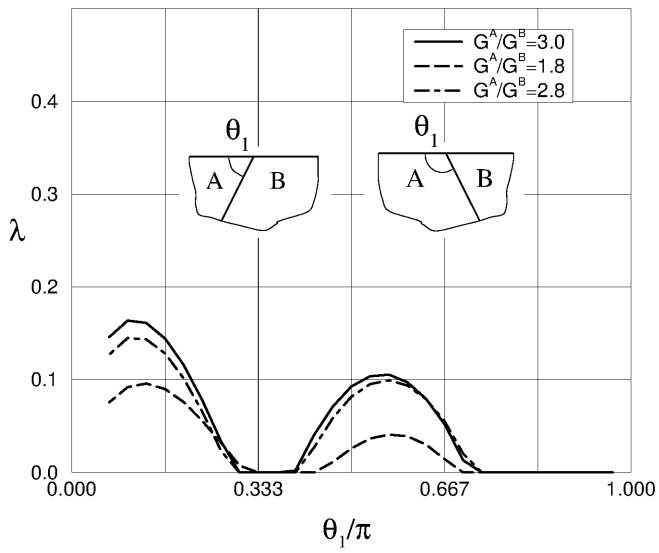

Figure 5.6: Variation of the order of singularity λ for different inclination angles Θ_1 at intersection point $\mathbf{X}$, keeping $\Theta_1 - \Theta_2 = \pi$

close to the intersection point. Again, we find that by decreasing the angle Θ_2 the order of the singularity can be reduced. Thus, a smooth transition, which could be realized by a radius instead of the sharp corner, would avoid most of the free edge effect in this intersection region. It is also interesting to note that the order of singularity λ is higher for smaller elastic contrasts, an analogous behavior being evident in fig. 5.4. For elastic contrasts larger than unity the slope of the first eigenvalue is negative, i.e. the order of singularity decreases with increasing elastic contrast.

5.2.2 Concluding remarks on the analytical approach

An analytical treatment of the bimaterial wedge problem was utilized for improving the geometrical interface design with respect to free edge effects. Assuming an effective homogeneous material for both components meeting at the interface, singular stress and strain fields were predicted at the intersection points of the material interface and the free surface. It was demonstrated

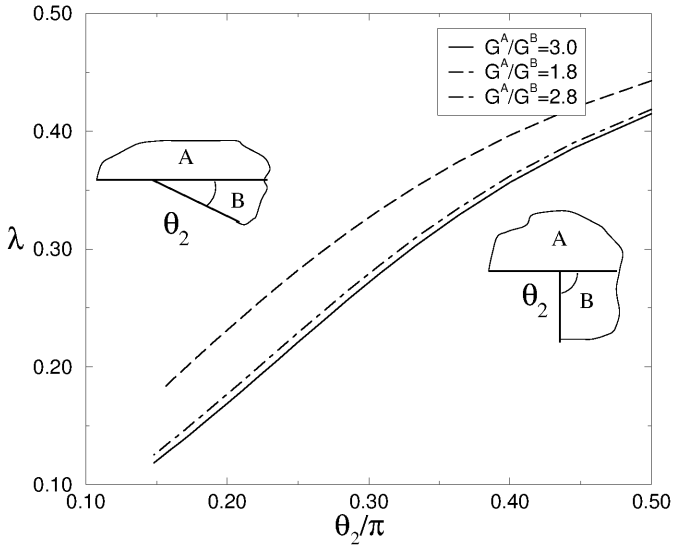

Figure 5.7: Variation of the order of singularity λ for different inclination angles Θ_2 ($\Theta_1 = \pi$, and Θ_2 varies from 0 to $-\pi/2$) at intersection point $\mathbf{Y}$

that the singularity can be reduced or even avoided by a proper design of the interface, thus mitigating free edge effects.

5.3 Numerical treatment of the bimaterial wedge problem

Although the Finite Element method (FEM), using standard regular continuum elements, cannot explicitly account for singularities, it is the most common tool for the investigation of free edge effects in arbitrarily shaped hybrid structures of finite size. A comprehensive treatment of the question whether or not an FEM solutions behaves in a consistent and reliable way in the immediate vicinity of singularities is given in [108]. Solving as a reference problem the free edge stress distribution of a mechanically loaded symmetric laminate it was found that the FEM solutions are accurate everywhere except very close to the singularity. The region of inaccurancy was found to be restricted to the two elements closest to the singular point. Similar results were found in the present study, the region where the results differ significantly from the analytic predictions being restricted to the distance of two integration points from the singular point. This region can be reduced by progressive mesh refinement to obtain any required degree of accurancy. Another possibility for considing singular stress–strain fields within the FEM is to introduce singular elements around the singularity, a method which is well known for applications in fracture mechanics. The most popular element in this respect is the quarter-point 8-noded degenerated quadrilateral element, introduced in [7]. The most severe limitation of this element is its ability to model only square-root singularities, i.e. $\lambda = 0.5$. However several methods have been published introducing Finite Elements which are capable of handling variable singularities λ, e.g. [34, 70, 84]. These methods are preferably used for applications where the order of singularity is known or can be derived analytically. For applications with unknown λ iterative procedures may have to be used, e.g.[8].

It should be noted that at a later stage of the present work it will be shown that for various hybrid components the singular stress fields predicted by structural analysis employing homogenized material descriptions for the multiphase part are not valid. They are a consequence of assumptions for the use of homogenization relations given in eqn. (2.2). Nevertheless the free

edge effect has to be treated comprehensively since it is important to obtain information on the size of the region that is influenced by the free edge effect in order to check whether homogenization via mean field approaches is acceptable or not. Thus the main topic of this chapter is determining the region where the stress and strain fields are mainly influenced by the singular stress field.

From eqn. (5.16) it is obvious that the stress field close to the intersection point is determined by a factor of the type $\left(\frac{L}{r}\right)^{\lambda}$, i.e. its range depends on the characteristic macroscopic length of the sample L, e.g. the length of the interface, and on λ.

Additionally, we have to notice that the introduction of L leads to a definition of the stress intensity factor K which is independent on the overall size of the component (a definition which obviously differs from the conventions used in fracture mechanics). Consequently, studying two bimaterial wedges made of equal materials, subjected to equal loading conditions and having a scaled geometry leads to geometrical similar results. The length scale dependence is introduced via the overall geometry (L) in contrast to the conventional definition in fracture mechanics, where a length scale is introduced via the finite crack length. Comprehensive studies of the geometrical influence on the singular stress field for components of finite size are given in [110].

5.3.1 Numerical investigation of the free edge effect in selectively reinforced components employing homogenized material descriptions

Numerical and experimental investigations of selectively reinforced axisymmetric components have indicated that the interfaces between the reinforced and the unreinforced material are the most critical regions with respect to failure. There are several reasons for this. On the one hand, at the interface the material strength is reduced because of the formation of oxide layers and intermetallic phases. On the other hand, as a consequence of the mismatch in the material properties thermal loading gives rise to eigenstresses of first and second order, i.e. stresses on the macro scale due the hybrid structure and stresses on the micro scale within the reinforced material. These stresses

reach maximum values close to the material interface. In addition, the intersection points between a material interface and the free surface are locations of complicated tri-axial stress states which are the consequence of the step-like, i.e. discontinuous, variation of the mechanical material parameters.

In the present section the stress field under several loading conditions is studied considering hybrid structures similar to the test specimens used for the experimental part of the project, compare chapter 1. In particular the free edge effect at the intersections between the macro interface (i.e. between the reinforced and unreinforced parts of a component) and the free surface is analysed to determine the order of singularity predicted by the use of homogenized material descriptions.

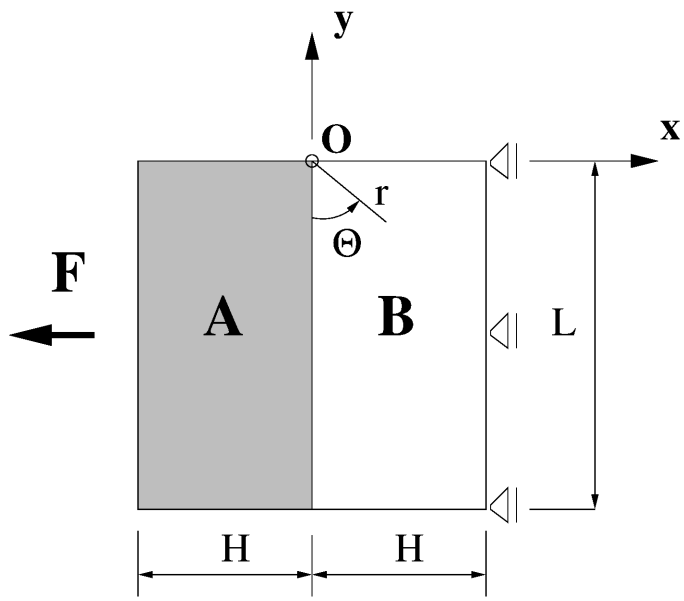

Figure 5.8: Selectively reinforced component, material **A**: matrix inclusion type composite, material **B**: monolithic matrix material

Primarily a selectively reinforced component having a square cross section as shown in fig. 5.8 is considered. The left half of the model {bf A is taken to be a continuously reinforced composite with a fiber volume fraction of 50%. The aligned fibers are assumed to be arranged in the out-of-plane

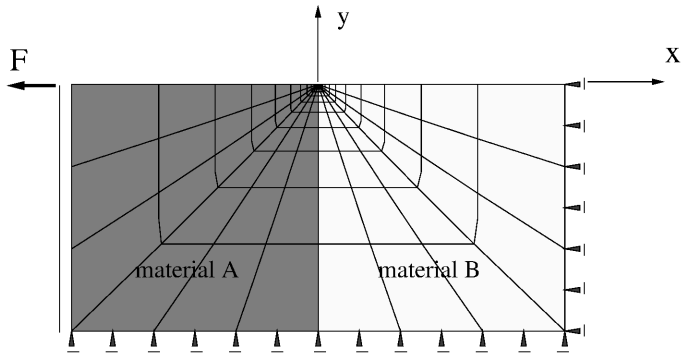

Figure 5.9: Macroscale FE-model of the hybrid structure

direction in a matrix having the same material properties as the homogeneous right half **B**. Hypothetical material parameters were chosen for matrix (m) and fibers (i) in order to reach a high elastic contrast: $E^{(m)} = 10.0\text{GPa}$, $\nu^{(m)} = 0.33$, $E^{(i)} = 167.5\text{GPa}$ and $\nu^{(i)} = 0.15$. For these material data, the elastic contrasts between the matrix and the effective (homogenized) material behavior of the composite as obtained by a Mori–Tanaka analysis [10] are $E^A_{x,y}/E^B_{x,y} = 2.5$ and $E^A_z/E^B_z = 8.9$. The model is loaded by a distributed force applied at the left side of the specimen causing an effective tensile stress of $\sigma_{xx} = 1\text{MPa}$. From the analytical solution of the boundary value problem it is known that the λ_k eqn.(5.16) correspond to the eigenvalues of a transcendental equation, i.e. in general there is an infinite number of terms. However, assuming isotropic materials for the given structure it can be shown that there exists only one valid eigenvalue and for mechanical loading the regular stress term $\sigma_{ij0}(\Theta)$ is equal 0, compare fig. 5.3. Thus eqn. (5.16) is reduced to

$$\sigma_{ij}(r,\Theta) = \frac{K}{(r/L)^{\lambda}} F_{ij}(\Theta). \tag{5.17}$$

From eqn. (5.17) it is obvious that λ can be estimated from the slope of the logarithmic plot $\log(\sigma_{ij}(r,\Theta))$ versus $\log(r/L)$.

The macroscale Finite Element model shown in fig. 5.9 uses homogenized material descriptions for the eight-noded isoparametric plane strain elements. A mesh progressively refined in the vicinity of the intersection between interface and free edge was used. Because of symmetry conditions only one

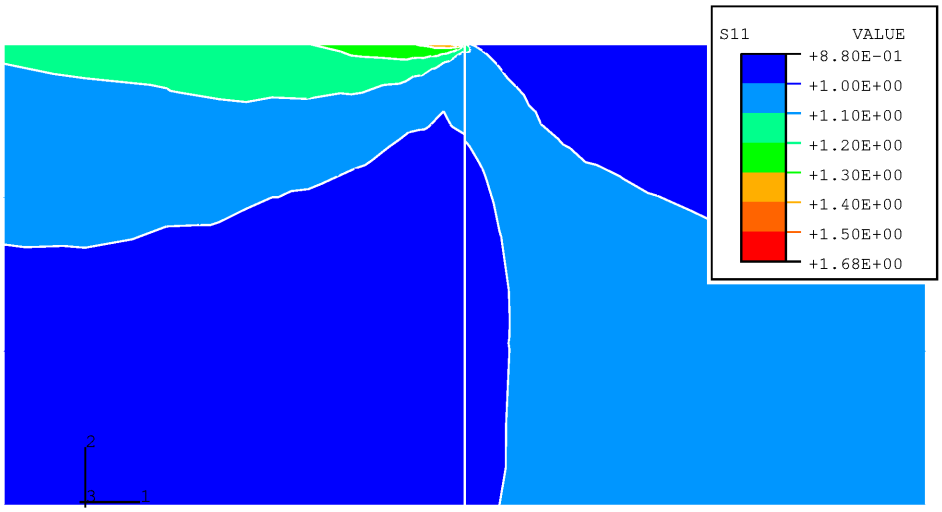

Figure 5.10: Predicted stress distribution σ_{xx} due to mechanical loading using homogenized material descriptions

half of the problem shown in fig. 5.8 was modeled ($-L/2 \leq y \leq 0$), where $L/2 = H = 20$mm. The x-displacements on the right boundary are locked and the left side is constrained to remain vertical.

The resulting stress distributions are given in fig. 5.10 for the stress component σ_{xx} and in fig. 5.11 for the shear stresses σ_{xy}, respectively. Both fringe plots exhibit homogeneous stress distributions except for a stress concentration close to the intersection point of the macro interface and the free surface.

The predicted stresses σ_{xx}, σ_{yy}, σ_{zz} and σ_{xy} along the interface ($x = 0$) are plotted in fig. 5.12, and along the the free edge ($y = 0$) in fig. 5.13. The normal stresses do not vary over a wide range of the interface, but close to the free surface they become unbounded. The shear stress σ_{xy} varies over the entire length of the interface to fulfill the equilibrium condition $\frac{\partial \sigma_{xx}}{\partial x} + \frac{\partial \sigma_{yx}}{\partial y} = 0$. Close to the intersection point σ_{xy} also becomes singular. Of course, if one stress component becomes singular all other stress components are singular, too.

In order to determine the order of the singularity λ the absolute values of each stress component are plotted along the interface (r/L) using a double logarithmic diagram in fig. 5.16. From the slopes of the logarithmic stress

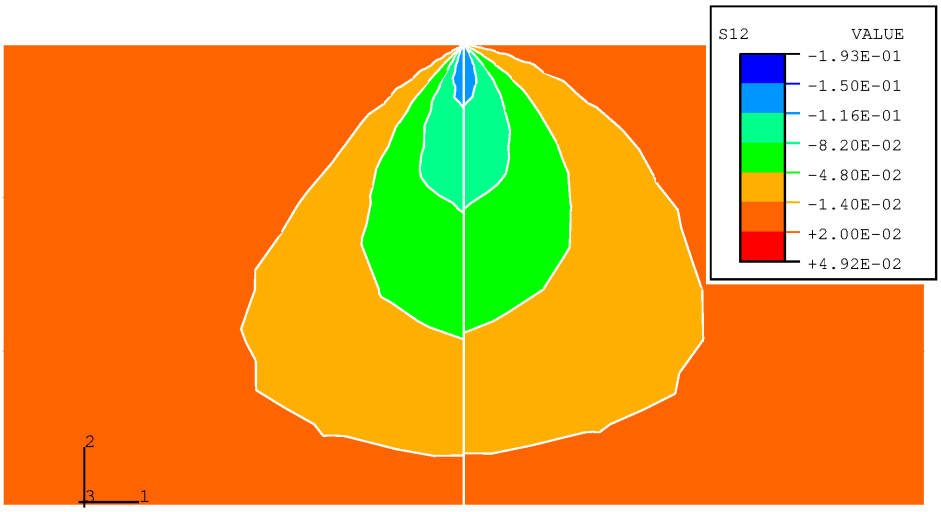

Figure 5.11: Predicted shear stress distribution σ_{xy} due to mechanical loading using homogenized material descriptions

components the numerical result for the order of the singularity is found to be $\lambda = 0.06$.

Thus, although the elastic contrast was increased by choosing hypothetical material parameters, the singularity is quite weak and the region influenced by the singular stress term is small. For a radial distance of 0.2mm from the singular point the singular stress term causes a stress increase of less than 30% .

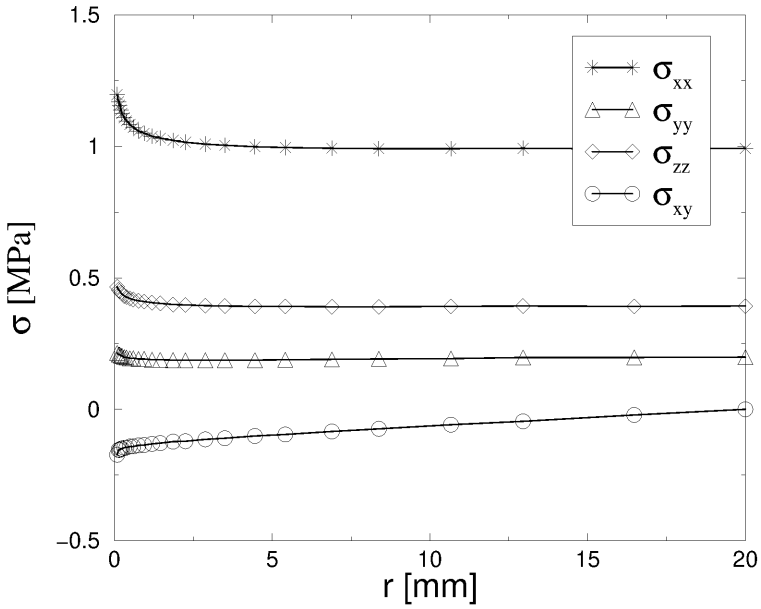

Figure 5.12: Stresses along the interface $x = 0$, for the radial distance $0 \leq r \leq L/2$

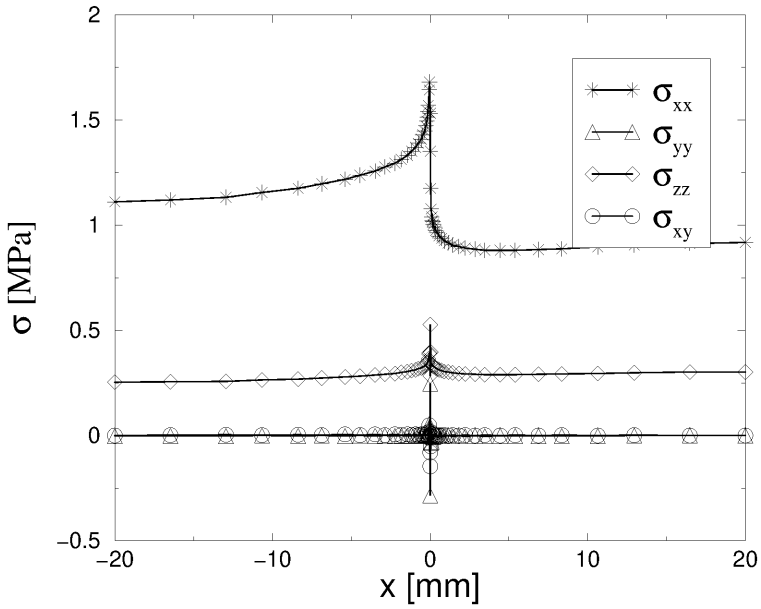

Figure 5.13: Stresses along the free edge $y = 0$

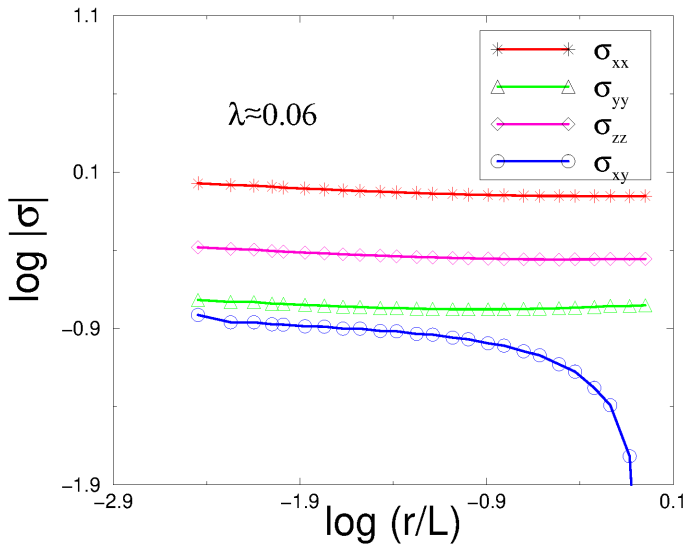

Figure 5.14: Stress components along the macro interface versus the distance from the singular point.

Using the same specimen geometry as before, we do a similar analysis applying a homogeneous thermal loading of $\Delta T = 10°\mathrm{C}$. Material **A** is considered to be a particle reinforced Al_2O_3–Al99.9 composite (having isotropic effective material properties). The reinforcement volume fraction is 0.5. Material **B** is considered to be monolithic Al99.9. Applying thermal loading the stresses close to the singular point are given by

$$\sigma_{ij}(r,\Theta) = \frac{K}{(r/L)^{\lambda}} F_{ij}(\Theta) + \sigma_{ij0}(\Theta). \tag{5.18}$$

The constant stress term $\sigma_{ij0}(\Theta)$ can be determined from the solution given e.g. in [78]. σ_{yy0} and σ_{xy0} are found to be zero, and σ_{xx0} is given by

$$\sigma_{xx0} = \Delta\alpha \Big[\frac{1}{E_A^*} - \frac{1}{E_B^*}\Big]^{-1} \Delta T, \tag{5.19}$$

using $E^* = E/(\nu(1+\nu))$ and $\Delta\alpha = \alpha_A(1+\nu_A) - \alpha_B(1+\nu_B)$.
After rearranging equation 5.18 and taking the logarithm of both sides the equation takes the form

$$\log\Big(\sigma_{ij}(r,\Theta) - \sigma_{ij0}(\Theta)\Big) = \log\Big(KF_{ij}(\Theta)\Big) - \lambda \log\Big(r/L\Big) \tag{5.20}$$

The stresses σ_{xx}, σ_{yy}, σ_{zz} and σ_{xy} predicted along the interface ($x = 0$) by the Finite Element method are plotted in fig. 5.15 Accordingly to eqn. (5.20) the order of singularity λ can be determined from the slope of the logarithmic plot $\log(\sigma_{ij}(r,\Theta) - \sigma_{ij0}(\Theta))$ versus $\log(r/L)$, shown in fig. 5.16. For the current problem the numerical result for the order of the singularity is $\lambda = 0.025$ which is in good agreement with the analytical solution of the boundary value problem.

Applying the same procedure to a long fiber reinforced hybrid structure (material **A** being a fiber reinforced MMC and material **B** pure metal) the singularity was predicted for an Altex fiber–Al–Al structure by $\lambda \approx 0.024$, the combination carbon fiber T300–AZ91D–AZ91D leads to $\lambda \approx 0.02$, and finally the combination Altex fiber–Al–AZ91D gives $\lambda \approx 0.065$. It should be mentioned that these values are only estimates for the singularities because the fiber reinforced MMC is not isotropic, so that eqn. (5.18) gives reasonable results only very close to the singular point. For an exact analytical solution

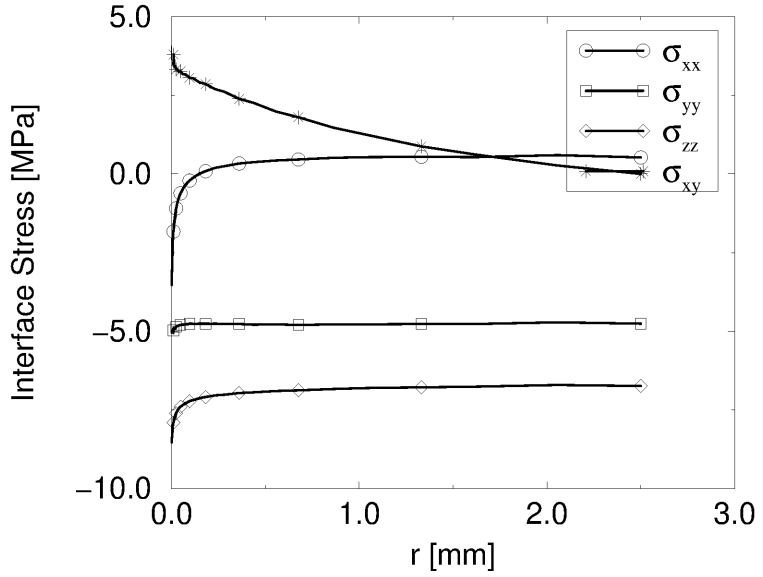

Figure 5.15: Stress components along the macro interface versus the distance from the singular point of an $Al_2O_3 - Al - Al$ hybrid component subjected to thermal loading.

of the boundary value problem including anisotropic materials see [72].
A similar investigation of free edge effects in selectively reinforced ring shaped structures is discussed in [25].

An important result that holds for all of the structural problems discussed here is that the order of singularity is very small. Thus the region affected by the singular stress term is very limited, i.e. its characteristic length is comparable to or smaller than the characteristic length of the constituents at the micro scale of the composite. Thus we come up with high effective stress–strain gradients at the microscale. Consequently a major assumption employed for the use of homogenized material description, i.e. that gradients in the macroscale stress and strain fields as well as compositional gradients (slow variables) are not significant at the microscale, see section 2.1, is violated. For this small region close to the intersection point special micromechanical approaches have to be employed, which are capable of accounting

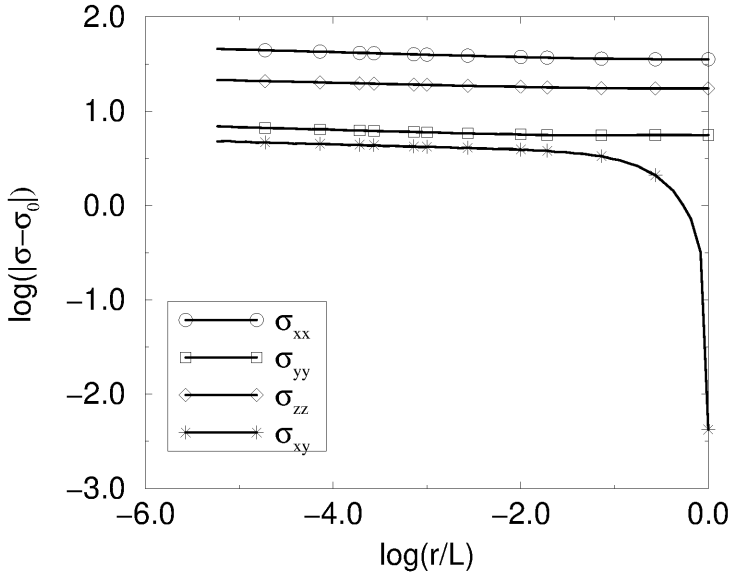

Figure 5.16: Stress components along the macro interface versus the distance from the singular point of an $Al_2O_3 - Al - Al$ hybrid component subjected to thermal loading.

for local compositional variations. For a discussion of some related problems in the field of free edge singularities in laminates see e.g. [111].
In the following section we use a combined macro–micromechanical embedding approach, which was introduced in [24], to study the free edge effect on the micro structural basis.

5.3.2 Combined macro–micromechanical investigation of free edge effects

In the previous section we found that arbitrary loading conditions lead to singular stress fields close to an intersection point of an interface between homogeneous materials and the free surface. Thus stress based failure criteria cannot be used to predict failure at the interface. Additionally it was argued that the use of homogenized material descriptions is not applicable for micro heterogeneous materials close to the intersection point.
In the present section it will be shown by using a micromechanical approach that under certain conditions these theoretically derived stress singularities disappear when the inhomogeneous microstructure of the composite is accounted for explicitly. Hence, a stress based assessment of the free edge stress fields is justified.

This modeling approach is discussed using the results of the previously considered example of a mechanically loaded hybrid component shown in fig. 5.8. For a detailed investigation of the free edge effect at a length scale comparable to the reinforcement size, an embedding method is used, which introduces a micromechanical submodel that is centered at the singular point of the global model ($x = 0$, $y = 0$) and has dimensions of 0.4mm by 0.2mm (i.e. it is somewhat larger than the zone of influence of the singularity in the homogenized model as defined in fig. 5.17). The composite material on the left side, **A**, is explicitly modeled via a periodic hexagonal array of fibers of 10μm diameter and a volume fraction of 50%, whereas region **B** consists of homogeneous isotropic matrix material. The material properties of the matrix and the fibers correspond to the data used to derive the homogenized properties for the macro model. The microgeometry is generated by a hexagonal cell tiling approach (HCT) [16], compare section 3.2. Displacements obtained from the macroscopic model are prescribed at the left, right, and bottom boundaries. A periodic fiber arrangement was chosen, on the one hand, because it has the required transversely isotropic overall material symmetry and, on the other hand, because it tends to minimize microscale stress concentrations that might mask the free surface effects to be studied.

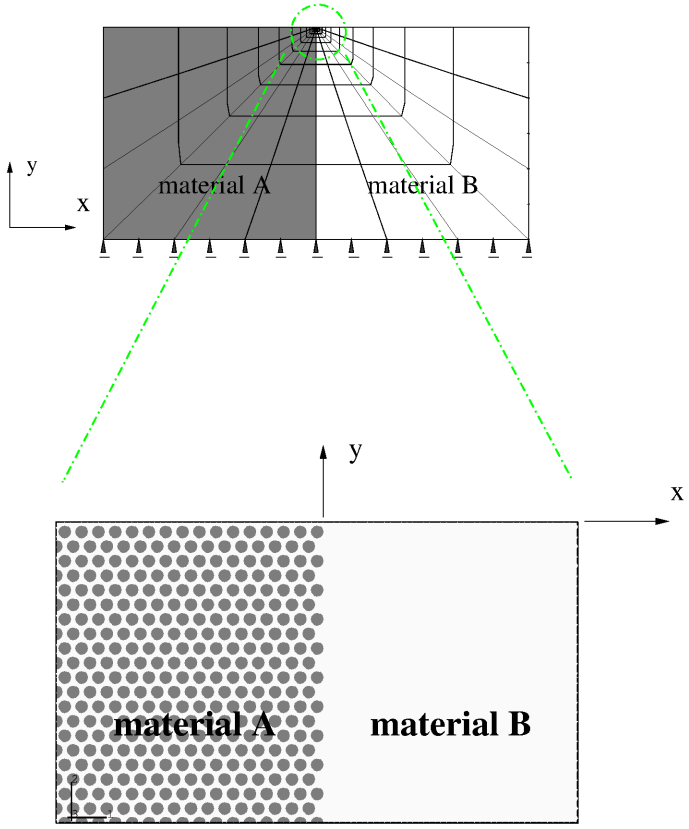

Figure 5.17: Micromechanically based submodel for local investigations close to the intersection point between the macro material interface and the free edge

It should be noted that, due to the change from a homogenized material description to position dependent constituent material properties, the present submodel technique gives rise to perturbations in the local stress fields along the left and lower boundaries, which, however, decay within a few fiber diameters and are of no relevance to the region of interest.

The results obtained with the submodel display no marked stress concentrations at the intersection between the interface and the free surface, as can be seen in fig. 5.18 which shows the stress component σ_{xx} in the matrix (top) and in the fibers (bottom). The most highly stressed regions in both constituents are found in region **A** in the neighborhood of the intersection between inter-

face and free surface. The peak values of the predicted microscale stresses in both fibers and matrix, however, do not exceed the applied stress by more than a factor of 3.1.

The low stress intensities predicted by the micro model clearly show that in the vicinity of the bimaterial junction the conditions for using homogenized material properties, which lead to the prediction of a stress singularity, were not met. Even though the results were obtained for the case of a selectively reinforced sample, i.e. for an inhomogeneous material **A** containing inclusions in a matrix corresponding to material **B**, it might be expected that an analogous behavior will prevail if both materials are matrix–inclusion composites with a common matrix, e.g. at the interfaces of a fiber reinforced laminate, where each lamina is composed of the same matrix with individual fiber directions.
The (hypothetical) example of two joined matrix–inclusion composites, having different matrix materials, however, suggests that free edge singularities can be present in bimaterial samples with a pronounced microstructure. More sophisticated microscale models (or nonlocal homogenization theories, see e.g. [33]) will be required for studying the stress states at such interfaces.

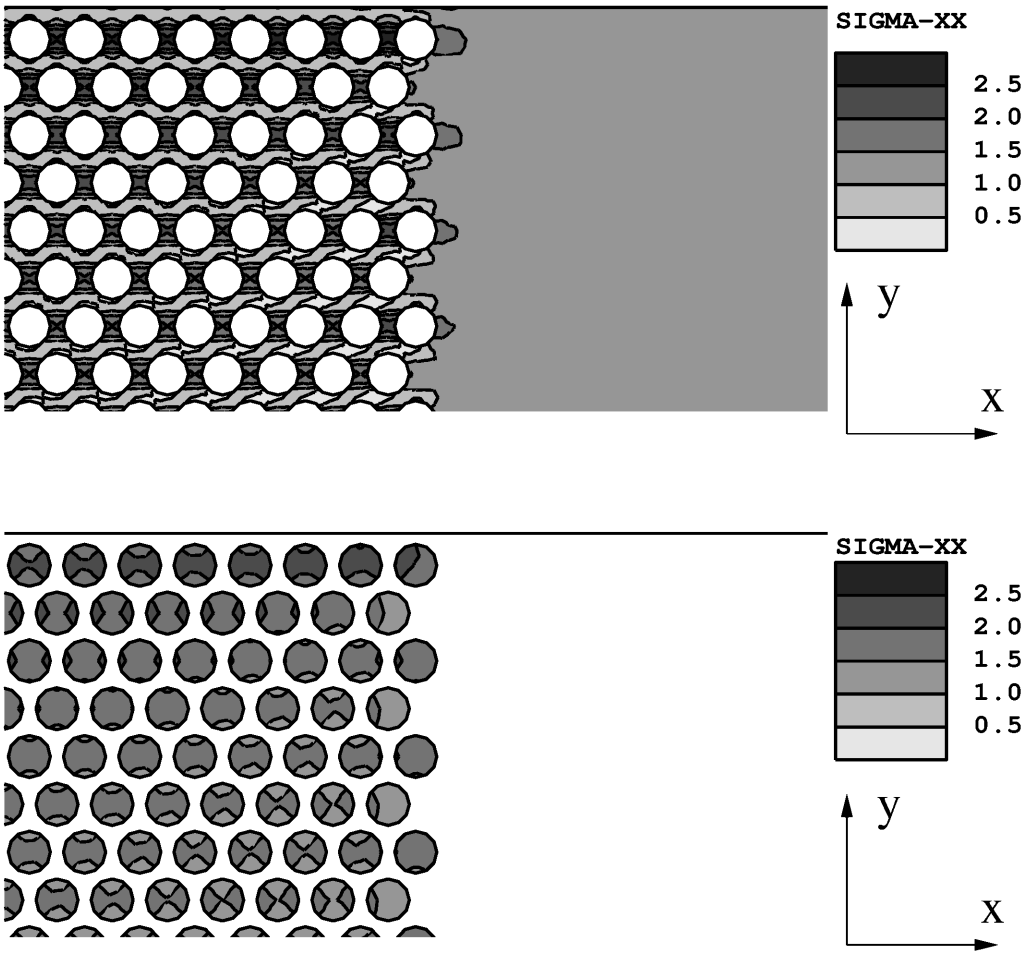

Figure 5.18: Predicted distributions of σ_{xx} in matrix (top) and fibers (bottom) within a detail of the submodel due to an applied effective macro stress of $\sigma_{xx}^{eff} = 1\text{MPa}$

Chapter 6

Structural Analysis of Hybrid Components

This chapter is dedicated to the micromechanical modeling of selectively reinforced components featuring the incremental Mori–Tanaka (IMT) approach. In addition a "quasi-real" structure model (the micro heterogeneity is modeled explicitly but in a bigger size scale compared to the real reinforcement distribution) is employed. To the knowledge of the author this is the first thermo–elasto–plastic investigation of a heterogeneous hybrid structure using micromechanically based material descriptions that explicitly accounts for the micro heterogeneity of the material. The hybrid component which was introduced in chapter 1, fig. 1.1 is intended as a generic part for developing manufacturing techniques for the production of selectively reinforced gear box housings. It consists of a circumferentially longfiber reinforced metal matrix composite surrounded by a monolithic (unreinforced) Mg–alloy. Due to the big differences in the coefficients of thermal expansion (CTE) of each constituent, on the macro level between MMC and monolithic material, as well as on the micro level between reinforcement and matrix of the MMC, it is expected that thermal loadings are most critical from the mechanical point of view. Hence, in the following investigation we look at the stress distribution after thermal loadings under thermo–elastic conditions as well as for thermo–elasto–plastic cases. Special consideration is given to the macro material interface between the MMC and the monolithic region.

6.1 Thermo–elastic analysis

The Finite Element mesh used for the axisymmetrical macro model of the component is shown in fig. 6.1. The dark area, i.e. the MMC ring insert, is modeled employing the IMT approach as material description at the integration point level of the elements, while the white area (pure matrix alloy) is described via standard material laws. The dimensions of the insert are 50mm for the inner diameter and 60mm for the outer one, its height being 12mm. The matrix material of the insert is the magnesium alloy AZ91D, which also makes up the monolithic part. The fibers are T300 carbon fibers with a volume fraction of $\xi = 0.5$ that are arranged in circumferential direction. Predicted stress distributions in each constituent after a temperature change of $\Delta T = -10$K are given in fig. 6.2 for the circumferential stresses σ_{zz} in the monolithic part and the matrix of the MMC (right figure) and in the fibers, respectively (left figure). The small axial coefficient of thermal expansion of the carbon fibers in comparison with the surrounding matrix causes circumferential compressive stresses in the fibers and tension in the matrix material after cooling down. The maximum fiber stresses are found in the lower right corner of the insert reaching values of more than 40MPa, while the maximum matrix stresses are located at the upper left corner with maximum stresses of about 15MPa. Additionally, some stress concentrations occur where the macro interface intersects the free surface. However, the coarse FE–mesh does not allow a detailed investigation of the free edge effect. In the previous chapter these intersection points were treated in detail. It was found that the singular stress field, predicted using homogenized material descriptions, is restricted to a very small region around the intersection point. Subsequently it is demonstrated that the singular solution of the stress field close to the intersection point of the free surface and the material interface is not always valid, since in the case of micro structured materials the gradients of the stress fields and the micro structural gradients are much too large to allow the use of a homogenized material description on the basis of mean field approaches see previous chapter. This effect is even more pronounced if the

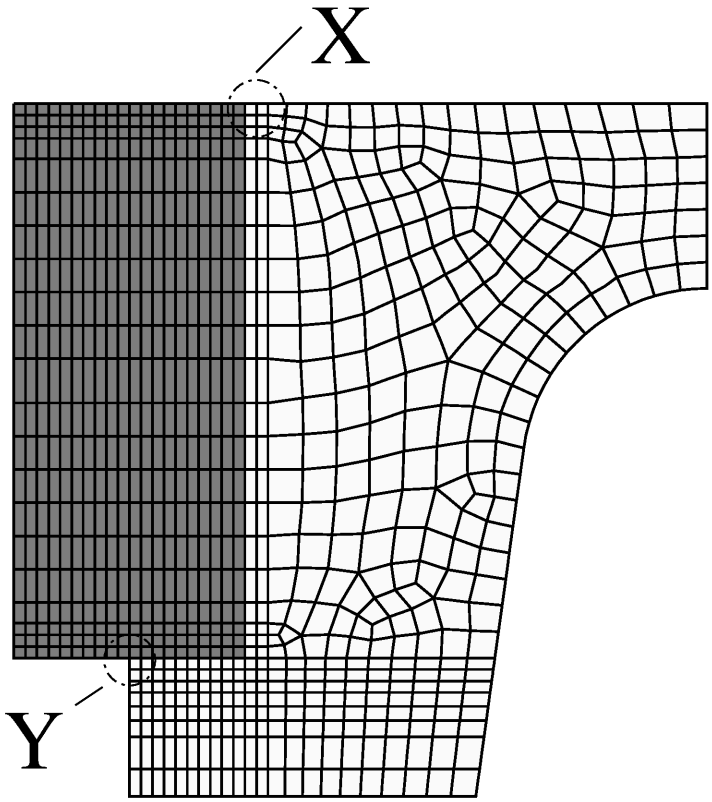

Figure 6.1: Axisymmetric FE–model for the selectively reinforced generic part

material transition is smeared out at the micro scale and a distinct interface no longer exists, as is the case for the material combinations covered here. In fig. 6.3 and 6.4 metallographic sections of a transition zone from carbon fiber reinforced magnesium to pure magnesium alloy are shown. These SEM pictures represent cross-sectional views perpendicular to the fiber direction. The "dotted" dark zone on the left side corresponds to the carbon/magnesium composite, whereas at the right pure magnesium alloy is visible. The very light areas are intermetallic $Mg_{17}Al_{12}$ precipitates. Although at the structural level a sharp interface would be expected, it is obvious that there is no distinct interface at the micro scale.

Accordingly the combined macro–micromechanical embedding technique introduced in chapter 5 is used for an assessment of the stresses close to

the intersection region. An axisymmetric micro scale submodel is centered around the intersection point **X**. It has the dimensions of 0.2mm in height, 0.4mm in width, the outer diameter of the insert being 60mm, see fig. 6.5. These dimensions are chosen to be sufficiently large to cover the region affected by the singular stress field derived from the macro model.

Within the submodel the heterogeneous microstructure of the MMC is modeled explicitly. The diameter of the fibers is chosen as 10μm, which is comparable to their actual size, see fig. 6.4, and for simplicity a periodic hexagonal arrangement of fibers is again used within the insert. The model micro geometry is generated via the HCT approach, compare chapter 5. The boundary conditions for the submodel are derived from the global analysis, i.e. displacements obtained from the macroscopic model are prescribed at its left, right, and bottom boundaries, and the same thermal loads as in the macro model are applied.

As in chapter 5 the results obtained with the submodel display no marked stress concentrations at the intersection between the macro interface and the free surface, as can be seen in fig. 6.6, a fringe plot of the radial stress component, σ_{xx}, and in fig. 6.7, which displays the axial stress component, σ_{zz}. Both stress components increase as the free surface is approached from the interior of the hybrid ring, but they actually decrease near the surface close to the macro interface. These predictions can be seen as evidence that in the immediate vicinity of the interface the micro stresses within the constituents of the MMC are relieved due to the presence of the monolithic material in the homogeneous region. In addition, these stress distributions strongly indicate that in the vicinity of the junction between MMC and homogeneous metal the conditions for using homogenized material properties, which lead to the prediction of a stress singularity, are not met.

The above predictions are, to some extent, verified by a series of experiments, in which special test specimens consisting of a cylindrical MMC insert embedded in an axisymmetric monolithic casting were produced for a structural push out test in order to characterize the strength of the macro interface. Investigations of the fracture surfaces after push out showed composite material on both sides of the fracture surface, which indicates that damage has been initiated within the MMC a few fiber diameters away from the interface.

In fig. 6.8 a metallographic view of a fractured generic part is shown, which failed after cooling down from manufacturing temperature. The upper part consists of reinforced material, while the lower, lighter colored part belongs to the monolithic constituent. The dark regions consists of the metallographic embedding material. It is evident that the crack was propagating close to the macro interface but again a view fiber diameters within the MMC.

The theoretical prediction that the maximum stresses occur at a distance of a few fiber diameters away from the interface is also in good agreement with results given in [22]. In that contribution the effective elastic properties within and around a cluster of inclusions embedded in an infinite matrix are studied using the nonlocal version of the multiparticle effective field method (MEFM). It was found there that the effective elastic tensor varies continuously from the cluster to the matrix within a boundary layer having a width of a few inclusion diameters. This is a further theoretical proof that no singularity occurs in configurations of the type discussed here.

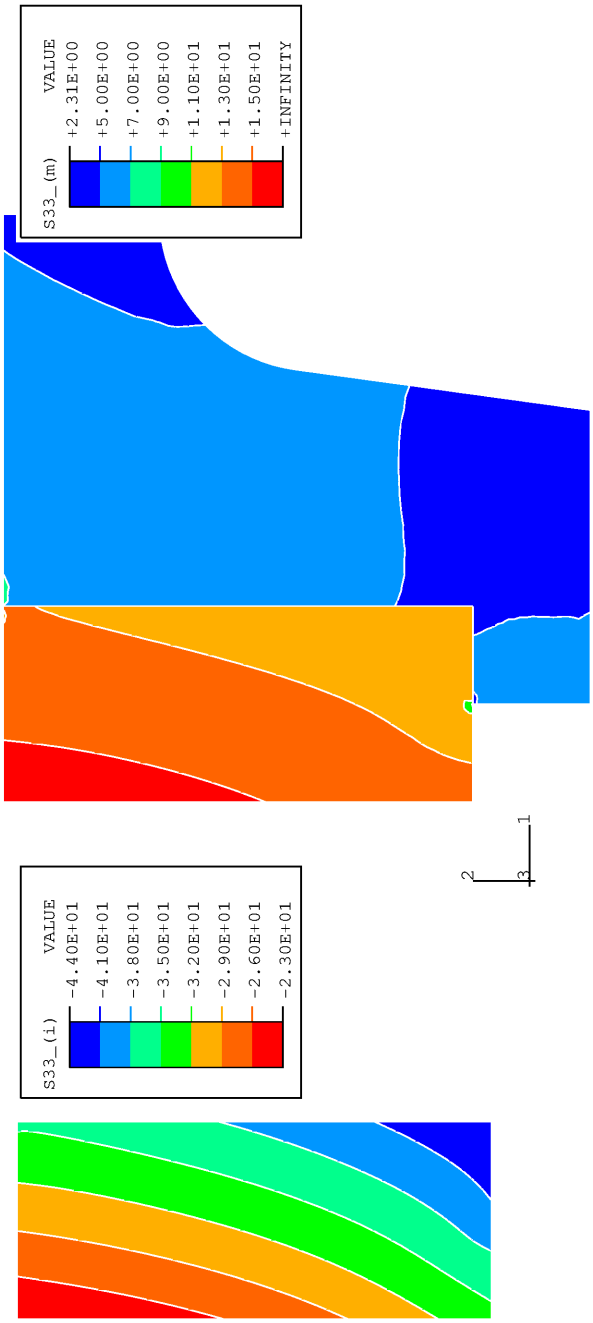

Figure 6.2: Predicted circumferential stresses σ_{zz} in the reinforcing fibers (left figure) and the matrix (right figure).

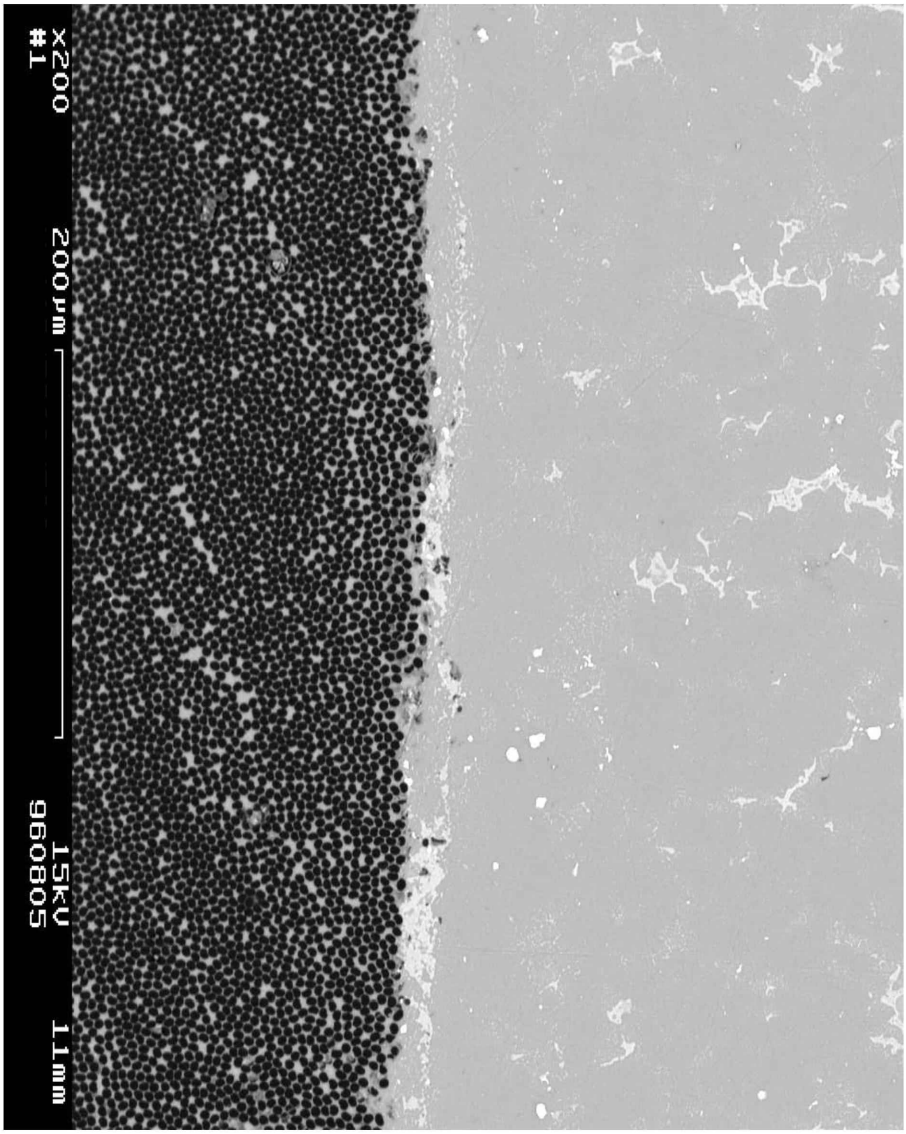

Figure 6.3: Cross-section of the macro interface perpendicular to the fiber direction obtained by SEM (supplied by Swiss Federal Laboratories for Material Testing and Research, Thun, Switzerland)

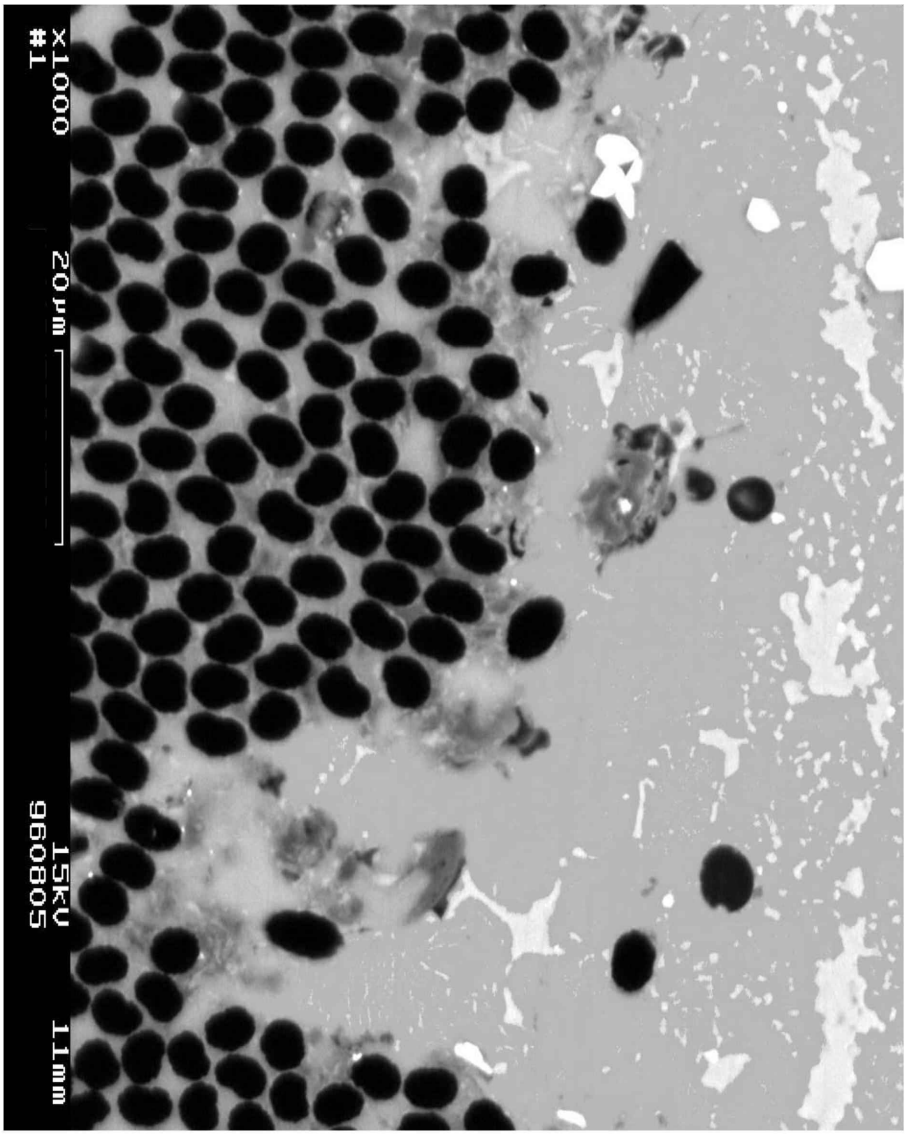

Figure 6.4: Detail of the cross-section of the macro interface perpendicular to the fiber direction obtained by SEM (supplied by Swiss Federal Laboratories for Material Testing and Research, Thun, Switzerland)

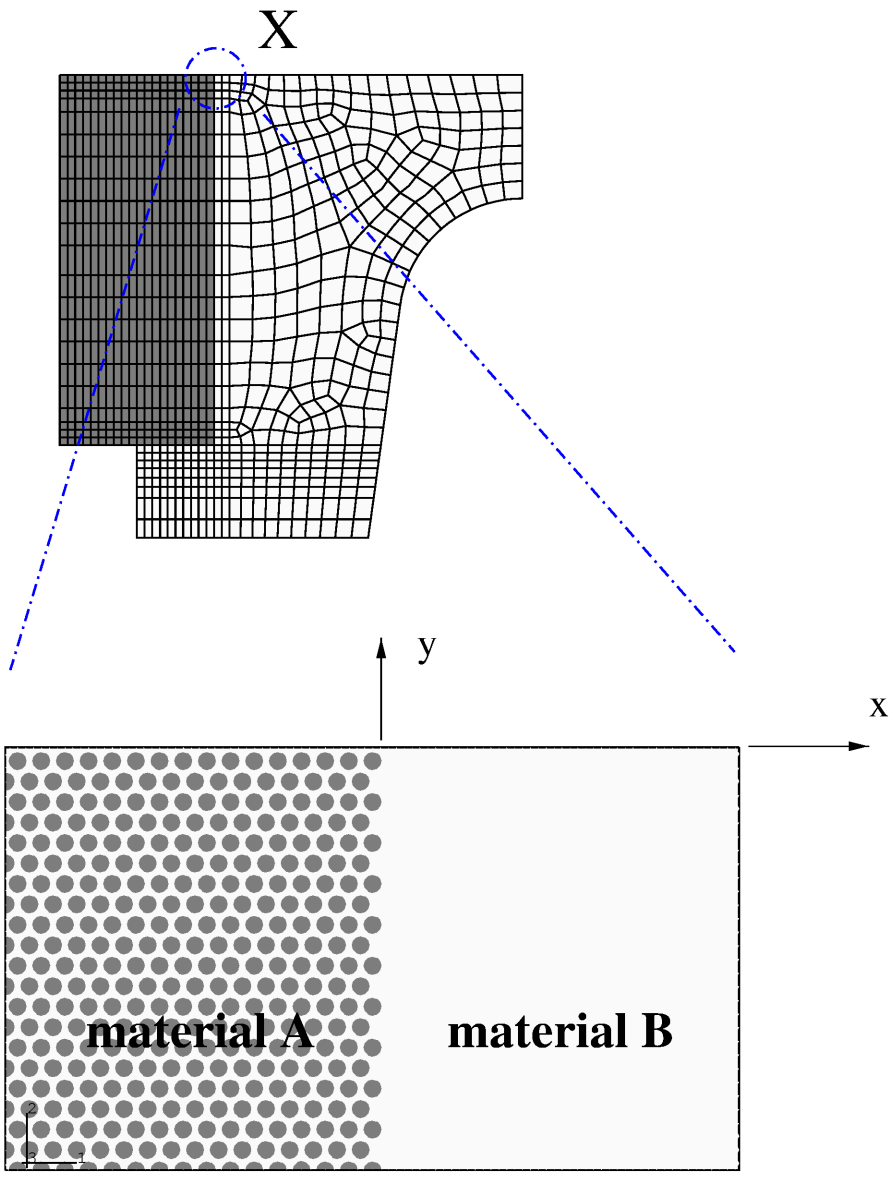

Figure 6.5: Micromechanically based submodel for local investigations of the region around intersection point **X**

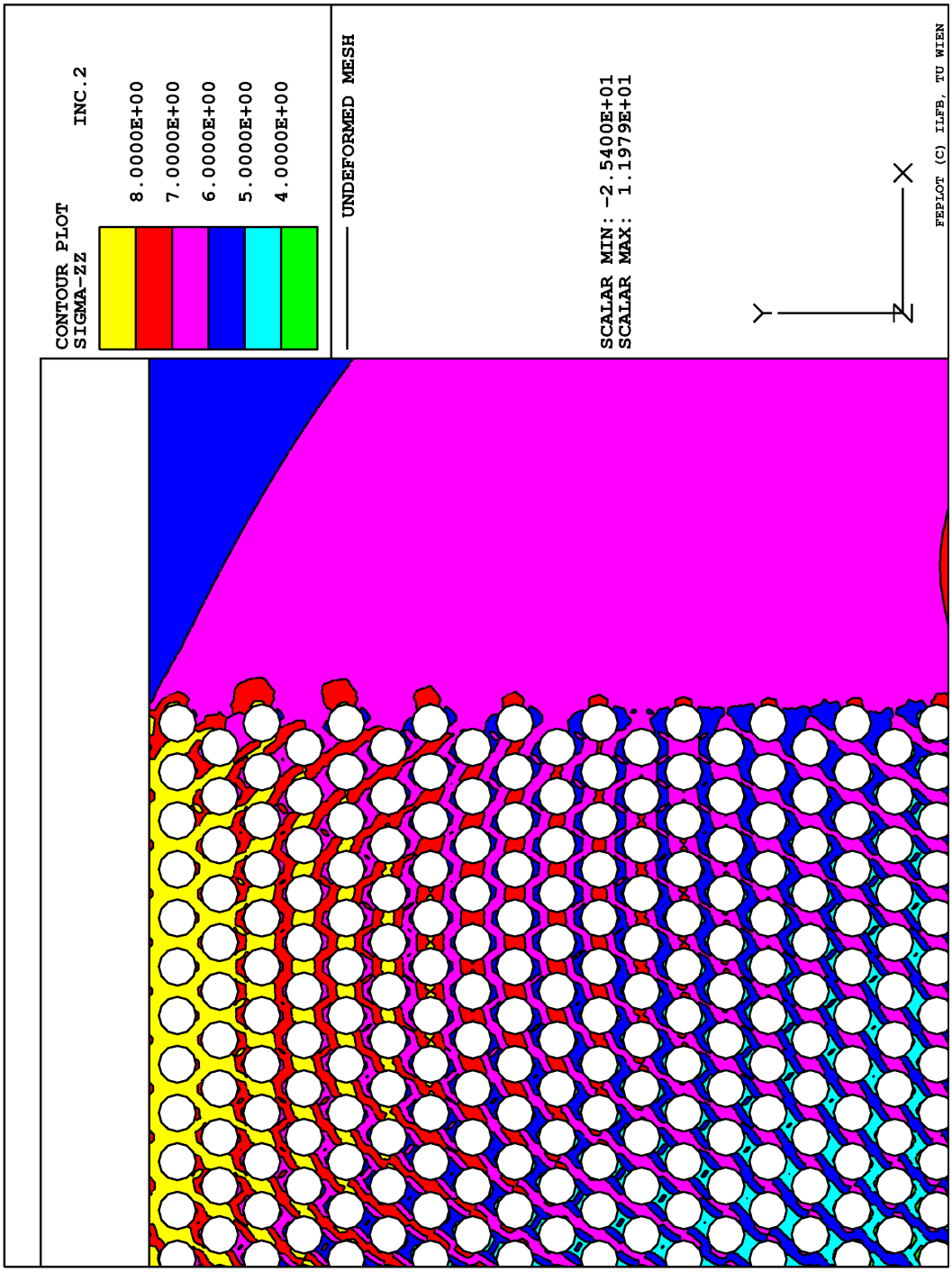

Figure 6.6: Detail fringe plot of the predicted distribution of the radial stresses σ_{xx} in the vicinity of the intersection between the macro interface and the free surface.

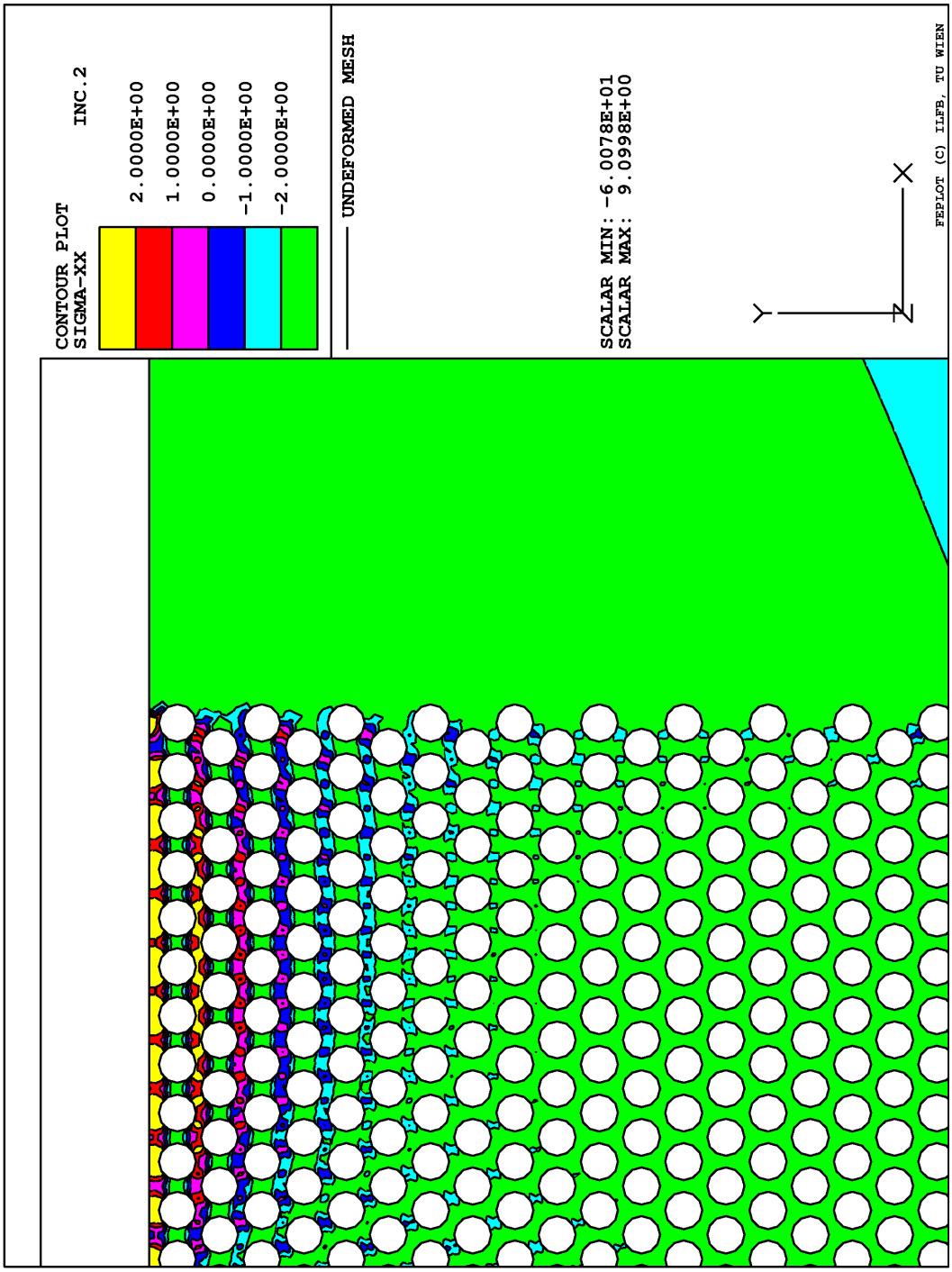

Figure 6.7: Detail fringe plot of the predicted distribution of the axial stresses σ_{zz} in the vicinity of the intersection between the macro interface and the free surface.

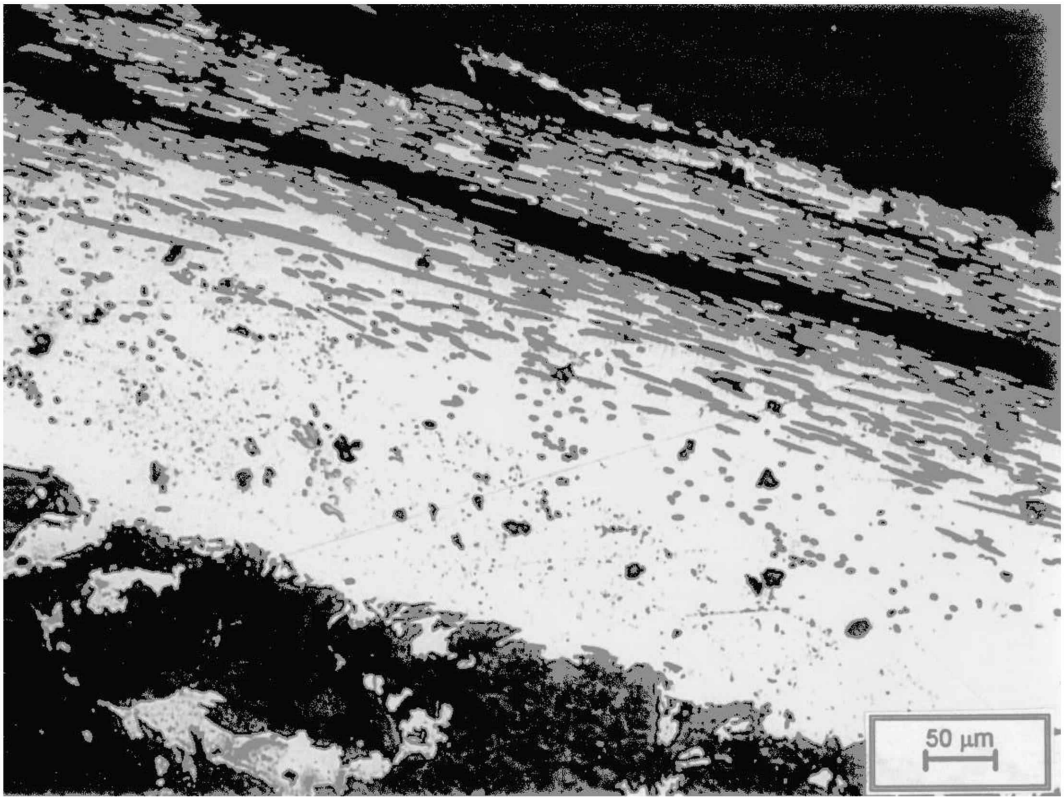

Figure 6.8: Metallographic view of a fractured macro interface where the crack occurs within the MMC (top) close to the monolithic material (lower light region). The black region belongs to metallographic embedding material (supplied by Inst. of Mat. Technology, TU-Vienna)

6.2 Thermo–elasto–plastic analysis

For comparison we introduce a second set of analyses of the generic part, where both the homogenized model employing the IMT–approach and a "real" structure model are used to simulate the stress accumulation due to cooling down from manufacturing temperatures. With respect to computational requirements it is unnecessarily difficult and as demonstrated in chapter 3 rather pointless to model the fibers in their real dimensions, so that MMC insert was modeled by periodic hexagonal arrangement of 1105 fibers. The heterogeneous phase pattern was derived using the HCT approach. The advantage of this modeling technique is that standard elasto–plastic material laws could be used and, additionally, the stress fluctuations at the microlevel are accounted for, whereas the IMT approach accounts for the micro stresses in terms of their mean values only , which, on the other hand, makes it feasible to cover a wide range of structural problems involving composite materials.
Both modeling techniques imply simplifications with respect to fiber curvature effects. The Mori–Tanaka method uses the assumption of straight ellipsoidal inclusions to derive the stress–strain concentration tensors used for the localization relations, compare chapter 2. The HCT approach covers the curvature effect, however introducing a different relation between fiber diameter and curvature radius. A validation of the two modeling approaches with respect to the previously mentioned shortcomings is given in chapter 3. The two models used for the following investigations are shown in fig. 6.9

For comparison of the results obtained from each model two small regions, annotated by the letters E and F, both lying within the MMC ring, are considered in detail. The calculations start at a temperature of 473K, which is about 0.7 of the homologous temperature of AZ91D, and it is assumed that the structure is stress free at this temperature. For temperatures above this value it is assumed that all stresses are deactivated by thermal activated relaxation processes.
In fig. 6.10 predictions of the variation of the circumferential stresses with temperature obtained via the HCT-model are shown for both the matrix (m)

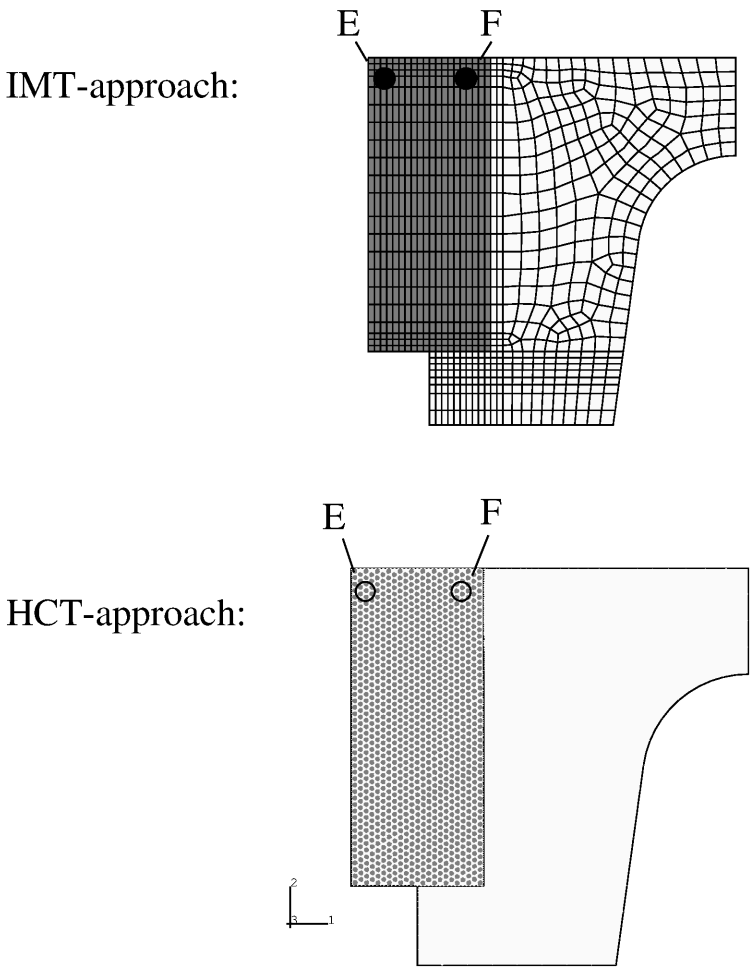

Figure 6.9: FEM models for the investigation of the generic part, employing the IMT and the HCT approach, respectively.

and the fibers (i). The mean values of the stress distribution for region E and F, and for the whole insert, respectively, are shown. Additionally, the standard deviations are indicated using "error bars".
Similarly to the elastic case the maximum fiber stresses (with respect to the cross sectional view of the generic part) are found in the lower right corner of the insert. Consequently the mean value over the whole insert exhibits much higher stresses than the values found for regions E and F. It is also found that the stress distribution inside the fibers is by far more homogeneous than the stress distributions found for the matrix, which is a well known behavior

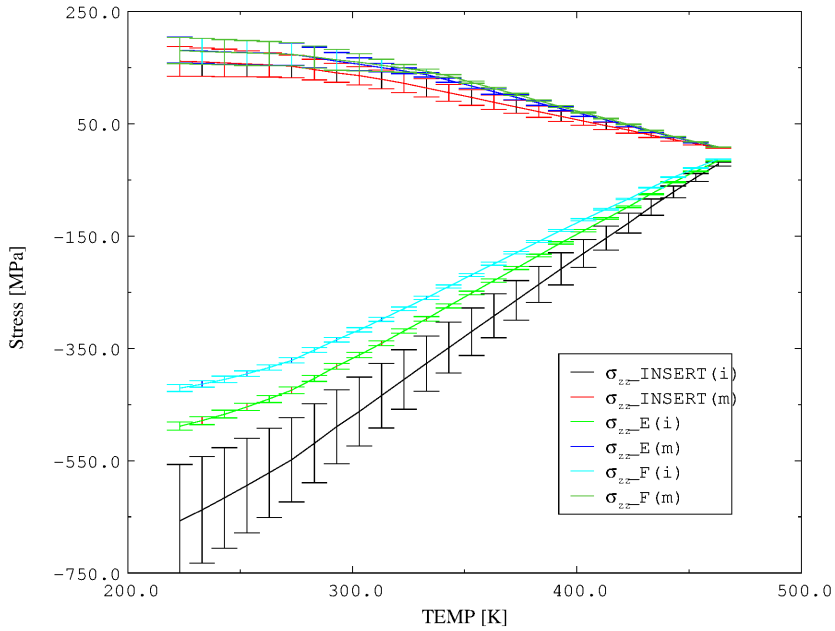

Figure 6.10: Circumferential (σ_{zz}) stresses predicted via the HCT–model. The given stresses are averages over the entire insert and over the regions E and F, respectively. The standard deviations are indicated by "error bars"

of inclusion–matrix type composites.

In fig. 6.11 results for the region E obtained via the IMT approach are presented together with the circumferential stresses obtained via HCT approach. The agreement between the two modeling techniques is excellent. However, for the radial and axial stress components σ_{xx}, σ_{yy} some discrepancies caused by the strong micro stress fluctuations in the HCT model occur, compare fig. 6.12. In figs. 6.13 and 6.14 a comparison is given for the model predictions of the accumulated equivalent plastic stain after a cool down of $\Delta T = -250$K. The matrix starts to plastify at the inner top corner of the insert and, additionally, at the intersection point of the macro interface and the top surface. The agreement found between both modeling approaches is excellent. For the plastic deformations predicted within the insert the HCT–model leads to higher values, caused by the micro stress fluctuations.

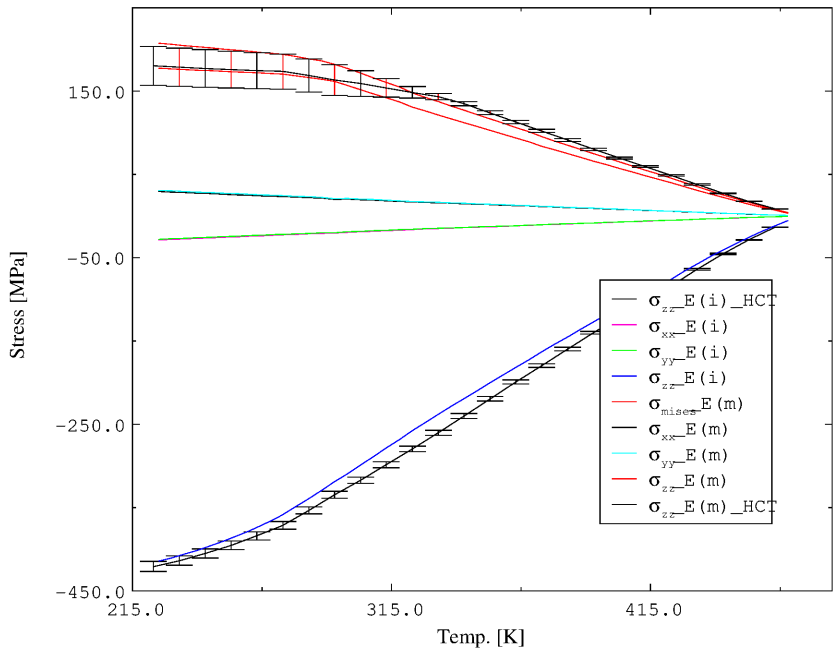

Figure 6.11: Comparison of IMT and HCT predictions for the circumferential phase stress components $\sigma_{zz}^{(i)}$ and $\sigma_{zz}^{(m)}$ in region E during cooling down

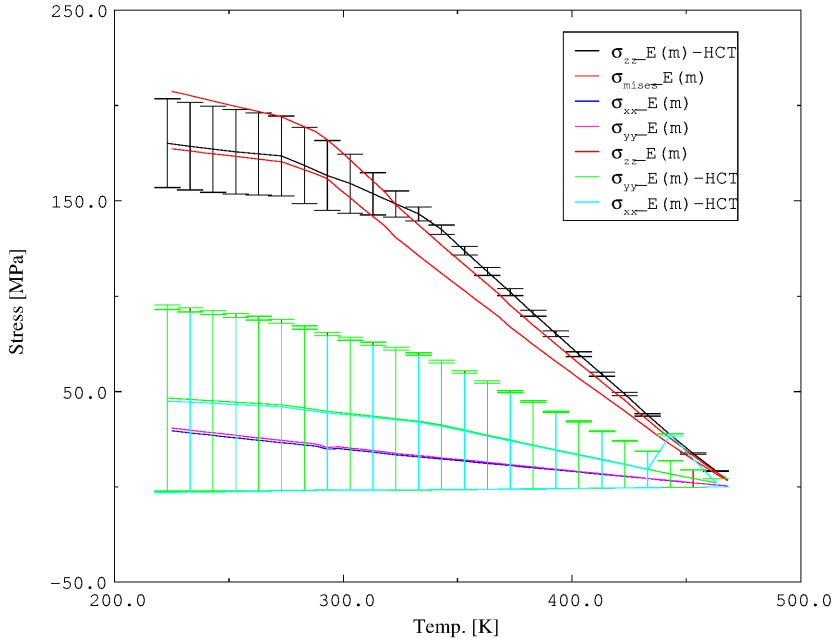

Figure 6.12: Comparison of IMT and HCT predictions for the phase stress components $\sigma_{zz}^{(m)}$, $\sigma_{xx}^{(m)}$ and $\sigma_{yy}^{(m)}$ in region E during cooling down

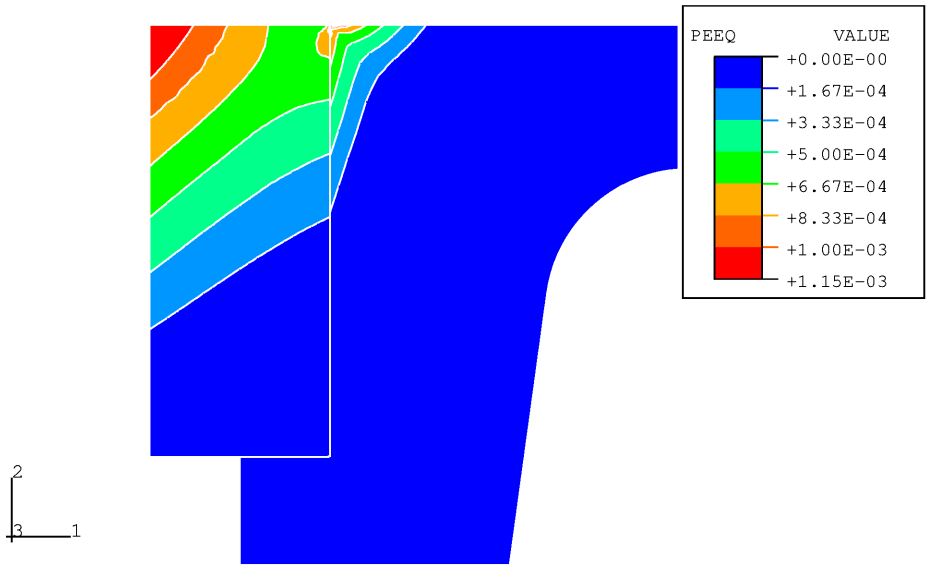

Figure 6.13: Equivalent plastic strain predicted for the matrix material using the IMT–model

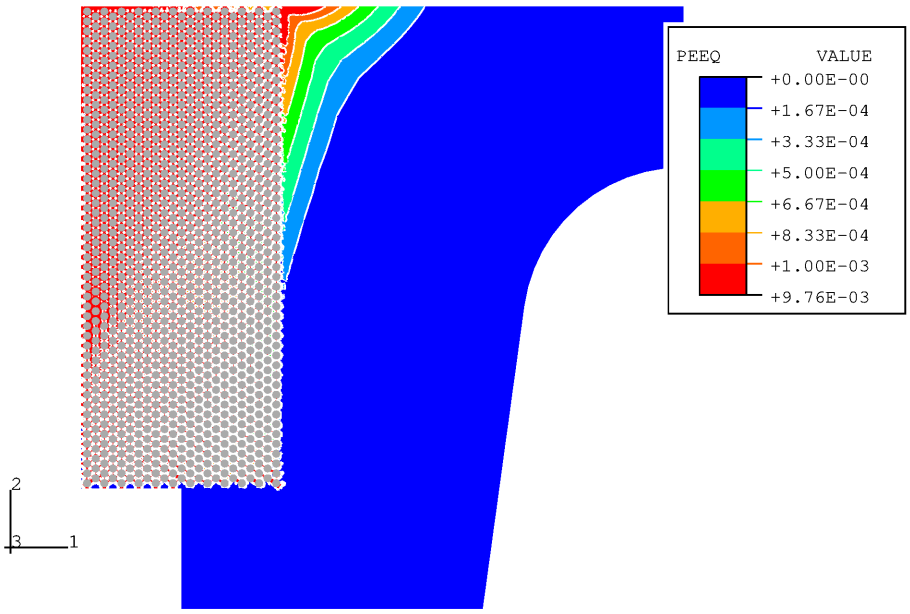

Figure 6.14: Equivalent plastic strain predicted for the matrix material using the HCT–model

Chapter 7

Conclusions

In the present work a number of topics relevant to the thermo–mechanical behavior of selectively reinforced magnesium based components have been studied via Finite Element based micromechanical methods. After a short review of selected micromechanical methods for the description of fiber reinforced composites the advantages of the Mori–Tanaka method (MTM), especially the incremental version of the Mori–Tanaka method which can be used as a material law at integration point level of standard finite elements, are pointed out.
By deriving the analytical solution for an arbitrarily layered cylinder it was demonstrated that the MTM, even though it is based on the assumption straight aligned spheroidal inclusions, is capable of modeling composite materials containing curved fibers without a significant loss of accuracy, which is essential for modeling circumferentially fiber reinforced axisymmetric structures.
Some material characterization based o n the MTM was presented. The thermo–mechanical responds of fiber reinforced Mg and Al composites under cyclic thermal loading was studied using a unit cell approach. It was demonstrated that the coefficient of thermal expansion for the composite must not be treated as a material constant. The simulation results clearly indicate a temperature–load history dependence.

As expected using a homogenized material description for the composite re-

gions in structural investigations of selectively reinforced structures subjected to arbitrary loading conditions leads to stress concentrations, i.e. singular stress fields, at the intersection of the material interface between reinforced and unreinforced material and the free edge. Using an analytical solution method for the singular stress problem it was found that the singularity can be reduced or even avoided by a proper interface design.
Introducing a micromechanically based embedding technique that explicitly accounts for the micro heterogeneity of the composite material it was found, that for the cases covered here the singular stress field disappears at the microscale, since there is no longer a distinct interface between the composite having the same matrix material as used for the unreinforced zone. Maximum stresses were found within the composite material a few fiber diameters away from the interface.

In the final part a themo–elasto–plastic analysis of a axisymmetric selectively reinforced component was carried out via the incremental Mori–Tanaka approach. Due to the simple shape of the reinforced part a comparison calculation using a hexagonal cell tiling approach was possible. The stress distribution after cooling down from the manufacturing temperature was studied on the macro– and, with respect to phase mean values, on the microlevel. The agreement found between the two models was excellent, i.e. the incremental Mori–Tanaka approach was found to be very well suited for the mechanical investigation of complex fiber reinforced structures.

Bibliography

[1] ABAQUS. Version 5.6. Hibbitt, Karlson & Sorensen, Inc., Pawtucket, RI, 1996.

[2] J. Aboudi. Analysis of composites by the method of cells. *Appl. Mech. Rev.*, 42:193–221, 1989.

[3] M. F. Ashby. *Materials selection in mechanical design.* Pergamon Press, Oxford, 1993.

[4] T. K. Aune and T. J. Ruden. High temperature properties of magnesium die castings alloys. *SAE Tech. Paper Series*, 920070, 1992.

[5] T. K. Aune and H. Westengen. Magnesium die casting properties. *Automotive Engineering*, pages 87–92, August 1995.

[6] C. Badini, M. Ferraris, and F. Marchetti. Interface reaction in AZ61/ AZ91/ P100 Mg/graphite composite: an Auger spectroscopy investigation. *Materials Letters*, 21:55–61, 1994.

[7] R. S. Barsoum. On the use of isoparametric finite elements in linear fracture mechanics. *Int. J. Num. Methods Eng.*, 10:25–37, 1976.

[8] R. S. Barsoum and C. E. Freese. An iterative approach for the evaluation of delamination stresses in laminated composites. *Int.J.Numer.Meth.Engng.*, 20:1415–1431, 1984.

[9] Y. Benveniste. A new approach to the application of Mori–Tanaka's theory in composite materials. *Mech.Mater.*, 6(2):147–157, 1987.

[10] A. K. Bhattacharya and S. I. Hong. Modelling of compressive stiffness of a multilayered graphite-reinforced magnesium-matrix composite. *Scr.metall.mater.*, 28:1131–1136, 1993.

[11] R. Bode and E. Hornbogen. Interfaces in magnesium matrix composites. In *Magnesium Alloys and Their Applications*, pages 461–468, Oberursel, Germany, 1992. DGM Informationsgesellschaft.

[12] D. B. Bogy. Edge-bonded dissimilar orthogonal elastic wedges under normal and shear loading. *J. Appl. Mech.*, 35:460–466, 1968.

[13] D. B. Bogy. On the plane elastostatic problem of a loaded crack terminating at a material interface. *J. Appl. Mech.*, 38,:911–918, 1971.

[14] H. J. Böhm. Computer based micromechanical investigation of the thermomechanical behavior of metal matrix composites. *VDI-Berichte*, Reihe 18(101), 1991. VDI-Verlag, Düsseldorf, Germany.

[15] H. J. Böhm. Notes on some mean field approaches for thermoelastic two-phase composite. *CDLμMW-Report*, 108, 1994.

[16] H. J. Böhm. HEXGRAIN V. A–2. Institute for Light Weight Structures and Aerospace Engineering, Vienna University of Technology, Austria, 1997.

[17] H. J. Böhm. *Lecture Notes, Composite Engineering*, chapter Micromechanics of Materials. Institute for Light Weight Structures and Aerospace Engineering, Vienna University of Technology, 1997.

[18] H. J. Böhm, H. P. Degischer, W. Lacom, and J. Qu. Experimental and theoretical study of the thermal expansion behavior of ceramic fiber reinforced aluminium. *Compos.Engng.*, 5(1):37–49, 1995.

[19] M. Bornert, E. Hervé, C. Stolz, and A. Zaoui. Self consistent approaches and strain heterogeneities in two-phase elastoplastic materials. *Appl.Mech.Rev.*, 47(1):S66–S76, 1994.

[20] Charlie R. Brooks. *Heat treatment, structure and properties of non-ferrous alloys.* American Society for Metals, Metals Park, OH 44073, 1982.

[21] L. M. Brown and W. M. Stobbs. The work-hardening of copper–silica. I. A model based on internal stresses, with no plastic relaxation. *Phil.Mag.*, 23:1185–1199, 1971.

[22] V. Buryachenko and F. G. Rammerstorfer. Micromechanics and non-local effects in graded random structure matrix composites. In *IUTAM Symposium on Transformation Problems in Composite and Active Materials*, Cairo, Egypt, March 1997.

[23] R. S. Busk. *Magnesium products design.* Marcel Dekker, New York, 1986.

[24] C. M. Chimani, H. J. Böhm, and F. G. Rammerstorfer. On the stress singularity at free edges of bimaterial junctions — a micromechanical study. *Scr. Mat.*, 36(8):943–947, 1997.

[25] C.M. Chimani, H. J. Böhm, and F. G. Rammerstorfer. A micromechanical investigation of thermally introduced stress singularities in heterogeneous hybrid structures. *Submitted to: Proceedings of the International Conference of Residual Stresses 5*, 1997.

[26] R. M. Christensen. Properties of carbon fiber. *J. Mech. Phys. Sol.*, 42(4):681–695, 1994.

[27] R. M. Christensen and Lo K. H. Solutions for effective shear properties in three phase sphere and cylinder models. *J.Mech.Phys.Sol.*, 27:315–330, 1979.

[28] R. M. Christensen and K. H. Lo. Erratum to Christensen and Lo, 1979. *J.Mech.Phys.Sol.*, 34:639, 1986.

[29] R. M. Christensen, H. Schantz, and J. Shapiro. On the range of validity of the Mori–Tanaka method. *J.Mech.Phys.Sol.*, 40(1):69–73, 1992.

[30] R.M. Christensen. A critical evaluation for a class of micromechanics models. *J.Mech.Phys.Sol.*, 38(3):379–404, 1990.

[31] B. Clyne and P. J. Withers. *An Introduction to Metal Matrix Composites.* Cambridge University Press, Cambridge, 1993.

[32] H.P. Degischer et.al. Project programme, "design and processing of selectively reinforced magnesium–based components". Technical report, EU–BE95–1183, 1996.

[33] W. J. Drugan and J. R. Willis. A micromechanics-based nonlocal constitutive equation and estimates of representative volume element size for elastic composites. *J. Mech. Phys. Sol.*, 44(4):497–524, 1996.

[34] B. K. Dutta. A six-noded element for analysing power-type singularities under thermal loads. *Int. J. Num. Methods Eng.*, 36:2287–2303, 1993.

[35] G. J. Dvorak and Y. A. Bahei-el Din. Plasticity analysis of fibrous composites. *J. Appl. Mech.*, 49:327–335, 1982.

[36] J. S. Epstein, S. Rawal, and M Misra. Microplasticity phenomena in graphite magnesium metal matix composites. *Optics and Laser in Engineering*, 12:1–17, 1990.

[37] J.D. Eshelby. The determination of the elastic field of an ellipsoidal inclusion and related problems. *Proc.Roy.Soc.London*, A241:376–396, 1957.

[38] A. C. Gavazzi and D. C. Lagoudas. On the numerical evaluation of Eshelby's tensor and its application to elastoplastic fibrous composites. *Comput.Mech.*, 7:12–19, 1990.

[39] D. E. R. Godfrey. Generalized plane stress in an elastic wedge under isolated loads. *Q. J. of Mech. Appl. Math.*, 8(2):226–236, 1955.

[40] D.L. Goodenberger and R.I. Stephens. Fatigue of AZ91E-T6 cast magnesium alloy. *J. Eng. Mat. Tech.*, 115(4):391–7, 1993.

[41] O. H. Griffin. *Three-dimensional inelastic finite element analysis of laminated composites.* PhD thesis, Virginia Polytechnic Institute and State University, Blacksburg, VA, 1980.

[42] L. Gu and T. Belytschko. A numerical study of stress singularities in a two-material wedge. *J. Sol. Struct.*, 31(6):865–889, 1994.

[43] Q. Gu and J. N. Reddy. Non-linear analysis of free edge effects in composite laminates subjected to axial loads. *Int. J. Non-Linear Mech.*, 27(1):27–41, 1992.

[44] F.W. Williams, C. Haoran, Y. Quangsan A self-consistent finite element approach to the inclusion problem. *Comput.Mater.Sci.*, 2(2):301–307, 1994.

[45] Z. Hashin. The elastic moduli of heterogeneous materials. *J.Appl.Mech.*, 29:143–150, 1962.

[46] Z. Hashin. Analysis of composite materials — a survey. *J.Appl.Mech.*, 50:481–505, 1983.

[47] Z. Hashin and B.W. Rosen. The elastic moduli of fiber-reinforced materials. *J.Appl.Mech.*, 31:223–232, 1964.

[48] Z. Hashin and S. Shtrikman. A variational approach to the theory of the elastic behavior of multyphase materials. *J.Mech.Phys.Sol.*, 11:127–140, 1963.

[49] M. Y. He, A. G. Evans, and J. W. Hutchinson. Interface cracking phenomena in constrained metal layers. *Acta Mater.*, 44(7):2963–2971, 1996.

[50] V. L. Hein and F. Erdogan. Stress singularities in a two-material wedge. *J. Fract. Mech.*, 7:317–330, 1971.

[51] R. Hill. *The Mathematical Theory of Placticity.* Oxford University Press, London, 1950.

[52] R. Hill. Elastic properties of reinforced solids: Some theoretical principles. *J.Mech.Phys.Sol.*, 11(8):357–372, 1963.

[53] R. Hill. Theory of mechanical properties of fibre-strengthened materials: III. Self-consistent model. *J.Mech.Phys.Sol.*, 13:178–188, 1965.

[54] J. Hult and F. G. Rammerstorfer. *Engineering Mechanics of Fibre Reinforced Polymers and Composite Structures.*, volume 282 of *CISM Lecture Notes.* Springer–Verlag, Vienna, Austria, 1994.

[55] S. Ioka, S. Kubo, K. Ohji, and J. Kishimoto. Thermal residual stresses in bonded dissimilar materials and their singularities. *JMSE Int. J. Series A*, 39(2):197–203, 1996.

[56] S. Jansson and F.A. Leckie. Transversal tensile and inplane shear strength of weakly bonded fiber reinforced MMC's subjected to cyclic thermal loading. *Mech. Mat.*, 18:205–212, 1994.

[57] G.S. Jeong. *Residual stress development due to cool down in viscoplastic metal matrix composites.* PhD thesis, Texas A&M University, College Station, TX, 1993.

[58] Y. Kagawa and E. Nakata. Some mechanical properties of carbon fiber-reinforced magnesium-matrix composites fabricated by squeeze casting. *J. Mat. Sci. Let.*, 11:176–178, 1992.

[59] M. Karayaka and H. Sehitoglu. Thermomechanical deformation modeling of Al2xxx-T4/SiC_p composites. *Acta metall.mater.*, 41(1):175–189, 1993.

[60] A. Kleine, J. Hemptenmacher, H. J. Dudek, K. U. Kainer, and G. Krüger. Interface formation in corbon fibre reinforced magnesium alloys (AZ91). *J. Mat. Sci. Let.*, 14:358–360, 1995.

[61] M. Kojić, N. Grujović, R. Slavković, and M. Zivković. A general orthotropic von Mises plasticity model with mixed hardening: Model definition and implicit stress integration procedure. *J.Appl.Mech.*, 63(2):376–382, 1996.

[62] D. C. Lagoudas, A. C. Gavazzi, and H. Nigam. Elastoplastic behavior of metal matrix composites based on incremental plasticity and the Mori–Tanaka averaging scheme. *Comput.Mech.*, 8:193–203, 1991.

[63] W. Ledermann and Vajda. *Handbook of Applicable Mathematics*, volume IV : Analysis. John Wiley & Sons, Chichester 1982.

[64] S. M. Lee. *International Encyclopedia of Composites*, volume 3. VCH Publishers, New York, NY, 1990.

[65] Y.-D. Lee and F. Erdogan. Residual/thermal stresses in FGM and laminated thermal barrier coatings. *Int. J. Fracture*, 69(2):45–165, 1995.

[66] C. C. Li and E. S. Folias. Edge effect of carbon fiber meeting a surface. *J. Mech. Mat.*, 12(3-4):267–278, 1991.

[67] N. Llorca. Fatigue behaviour of short alumina fibre reinforced AZ91 magnesium alloy metal matrix composite. *Mat. Sci. Eng.*, A135:247–52, 1991.

[68] A. Luo. Processing, microstructure, and mechanical behavior of cast magnesium metal matrix composites. *Metallurgical and Materials Transactions A*, 26A:2445–2455, 1995.

[69] J. M. Mahishi. An integrated micromechanical and macromechanical approach to fracture behavior of fiber-reinforced composites. *Eng. Frac. Mech.*, 25:197–228, 1986.

[70] S. K. Maiti. A finite element for variable order singularities baseed on the displacement formulation. *Int. J. Num. Methods Eng.*, 33:1955–1974, 1992.

[71] A. Martin and J. Llorca. Mechanical behaviour and failure mechanisms of binary Mg-6% Zn alloy reinforced with SiC particulates. *Mat. Sci. Eng.*, A201:77–87, 1995.

[72] S. E. Mikhailov. Plane problem for two bonded anisotropic wedges. *Izv. AN SSSR. Mekhanika Tverdogo Tela*, 14(5):103–110, 1979.

[73] S. E. Mikhailov. Stress singularity in a compound arbitrarily anisotropic body and applications to composites. *Izv. AN SSSR. Mekhanika Tverdogo Tela (Mechanics of Solids)*, 14(6):33–42, 1979.

[74] W.K. Miller. Creep of die cast AZ91 magnesium at room temperature and low stress. *Metallurgical Transactions A*, 22A(4):873–877, 1991.

[75] I. Mochida, S. H. Yoon, N. Takano, F. Fortin, Y. Korai, and K. Yokogawa. Microstructure of mesophase pitch-based carbon fiber and its control. *Carbon*, 34(8):941–956, 1996.

[76] T. Mori and K. Tanaka. Average stress in the matrix and average elastic energy of materials with misfitting inclusions. *Acta Metall.*, 21:571–574, 1973.

[77] D. Munz and Y. Y. Yang. Stress singularities at the interface in bonded dissimilar materials under mechanical and thermal loading. *J. Appl. Mech.*, 59:857–861, 1992.

[78] D. Munz and Y. Y. Yang. Stresses near the free edge of the interface in ceramic-to-metal joints. *J. Europ. Ceramic Soc.*, 13:453–460, 1994.

[79] T. Nakamura and S. Suresh. Effects of thermal residual stresses and fiber packing on deformation of metal-matrix composites. *Acta Metall.Mater.*, 41(6):1665–1681, 1993.

[80] J.F. Nye. *Physical Properties of Crystals, Their Representation by Tensors and Matrices.* Clarendon, Oxford, UK, 1957.

[81] R. Oaklay, R. F. Cochrane, and R. Stevens. Recend developments in magnesium matrix composites. *Key Engineering Materials*, 104-107:387–416, 1995.

[82] O. Öttinger, C. Grau, R. Winter, R. F. Singer, A. Feldhoff, E. Pippel, and J. Woltersdorf. The effect of aluminium additions on the interfacial microstructure of C/Mg composites. *In Proc. the tenth int. conf. on composite materials*, 6 microstructure, degradation, and design, 1995.

[83] O. Öttinger and R. F. Singer. An advanced melt infiltration process for the net shape production of metal matrix composites. *Z.Metallk.*, 84(12):827–831, 1993.

[84] S. S. Pageau and S. B. Biggers. Finite element evaluation of free-edge singular stress fields in anisotropic materials. *Int. J. for Num. Methodes in Eng.*, 38:2225–2239, 1995.

[85] H. Pettermann. Derivation and Finite Element Implementation of Constitutive Material Laws for Multiphase Composites Based on Mori–Tanaka Approaches. *VDI-Berichte*, Reihe 18(217), 1997. VDI–Verlag, Düsseldorf, Germany.

[86] K. Purazrang, P. Abachi, and K. U. Kainer. Mechanical behavior of magnesium alloy MMCs produced by squeeze casting and powder metallurgical techniques. *Compos.Engng.*, 3(6):489–505, 1993.

[87] I. S. Raju and J. H. Jr. Crews. Interlaminar stress singularities at straight free edge in composite laminates. *Computers & Structures*, 14(1-2):21–28, 1981.

[88] F. G. Rammerstorfer. *Repetitorium Leichtbau.* R. Oldenburg Verlag, Wien, 1992.

[89] F. G. Rammerstorfer and F. D. Fischer. A method for the experimental determination of residual stresses in axisymmetric composite cylinders. *J. Eng. Mat. Tech.*, 114:90–96, 1992.

[90] E. D. Reedy. Intensity of the stress singularity at the interface corner between a bonded elastic and rigid layer. *Eng. Fract. Mech.*, 36(4):575–583, 1990.

[91] N. Ricketts. The magnesium homepage.
URL: http://www.cat.csiro.au/~njr/mg_ home.htm, 1997.

[92] L. Rubin, D. J. Chang, E. Y. Robinson, and C. Tseng. Advanced composites for a dimensionally stable space structure. In *International SAMPE Technical Conference*, pages 345–358. Society for the Advancement of Material and Process Engineering, 1989.

[93] W. Sangani, A. Lu. Elastic coefficients of composites containing spherical inclusions in a periodic array. *J.Mech.Phys.Sol.*, 35(1):1–21, 1987.

[94] R. J. Schmidt, D. Q. Wang, and A. C. Hansen. Plastisity model for tranversely isotropic materials. *J. Eng. Mech.*, 119(4):748–766, 1993.

[95] N. J. Sørensen. Planar type analysis for the elastic–plastic behavior of continous fiber–reinforced metal matric composites under longitudional shearing and combined loading. DCAMM Report 418, Technical University of Denmark, Lyngby, 1991.

[96] T. Steinkopff and M. Sautter. Simulating the elastic-plastic behavior of multiphase materials by advanced Finite Element techniques, part I: A rezoning technique and the multiphase Finite Element method. *Comput.Mater.Sci.*, 4(1):10–14, 1995.

[97] Sumitomo. Altex data sheet. Technical report, Sumitomo Chemical Corp. Ltd., Osaka, 1994.

[98] P. M. Suquet. Effective properties of nonlinear composites. In *Continuum Micromechanics*, Springer–Verlag, Vienna, 1997

[99] S. Suresh, A. Mortensen, and A. Needleman. *Fundamentals of metal-matrix composites.* Butterworth-Heinemann, Boston 1993.

[100] A. J. Svobodnik, H. J. Böhm, and F. G. Rammerstorfer. A 3/D Finite Element approach for metal matrix composites based on micromechanical models. *Int.J.Plast.*, 7(8):781–802, 1991.

[101] C. J. Tranter. The use of the Mellin transform in finding the stress distribution in an infinite wedge. *Quart. J. of Mech. and Appl. Math.*, 1:125–130, 1948.

[102] G. Z. Voyiadjis and W. Huang. A modelling of single crystal plasticity with backstress evolution. *Eur. J. Mech. A/Solids*, 553–573, 15(4) 1996.

[103] K. Wakashima, H. Tsukamoto, and B. H. Choi. Elastic and thermoelastic properties of metal matrix composites with discontinuous fibers

or particles: Theoretical guidelines toward materials tailoring. In *The Korea–Japan Metals Symposium on Composite Materials*, pages 102–115. The Korean Institute of Metals, Seoul, Korea, 1988.

[104] J. W. Weeton, D. M. Peters, and K. L. Thomas. *Engineer's guide to composite materials.* American Society for Metals, Metals Park, OH, 1987.

[105] E. Weissenbeck, H. E. Pettermann, and S. Suresh. Numerical simulation of plastic deformation in compositionally graded metal-ceramic structures. *Acta Mater.*, 45:3401–3417, 1997.

[106] E. Werner, H. J. Böhm, W. Prantl, and F. G. Rammerstorfer. Plasticity and damage of a fiber reinforced aluminium alloy: Experiments and micromechanical modeling. *submitted to Zamm*, 1997.

[107] M. L. Williams. Stress singularities resulting from various boundary conditions in angular corners. *J. Appl. Mech.*, 74:526, 1952.

[108] J. D. Withcomb, I. S. Raju, and J. G. Goree. Reliability of the Finite Element Method for calculating free edge stresses in composite laminates. *Computers & Structures*, 15(1):23–37, 1982.

[109] F. Wu and J. Zhu. Morphology of second-phase precipitates in carbon-fiber- and graphite-fiber-reinforced magnesium-based metal-matrix composites. *Composites Sci. Tech.*, 57:661–667, 1997.

[110] Y. Y. Yang. *Spannungssingularitäten in Zweistoffverbunden bei mechanischer und thermischer Belastung.* PhD thesis, Universität Karlsruhe, 1992.

[111] L. Ye. Some characteristics of distributions of free-edge interlaminar stresses in composite laminates. *Int. J. Sol. Struct.*, 26(3):331–351, 1995.

Curriculum Vitae

Name:	Christian Maximilian Chimani
Date of birth:	[redacted]
Place of birth:	
Citizenship:	Austrian

Education

1983–1988	Technical High School, Dept. of Mechanical Engineering, Wels, Austria.
1988–1989	Military service
1989–1995	Studies of Material Science at the University of Mining and Metallurgy, Leoben, Austria
June 1995	Graduate with the degree of Diplom–Ingenieur
since 1995	Doctoral Student at the Institute of Light Weight Structures and Aerospace Engineering, Vienna University of Technology, Austria
July 1996	Participant at the Institute for Mechanics and Materials Summer School 1996, "The Mechanics–Materials Linkage", University of California, San Diego, CA

Scientific Experience

1994–1995	Diploma Thesis on Dynamic Simulation of Ceramic Test Specimens
since 1995	Research assistant at the *Institute of Lightweight Structures and Aerospace Engineering*, Vienna University of Technology, Vienna, Austria